JAERI-Research
2004-027

ENERGY CONFINEMENT AND TRANSPORT OF H-MODE PLASMAS IN TOKAMAK

February 2005

Hajime URANO

日本原子力研究所
Japan Atomic Energy Research Institute

本レポートは，日本原子力研究所が不定期に公刊している研究報告書です。
入手の問合わせは，日本原子力研究所研究情報部研究情報課（〒319-1195　茨城県那珂郡東海村）あて，お申し越しください。なお，このほかに財団法人原子力弘済会資料センター（〒319-1195　茨城県那珂郡東海村日本原子力研究所内）で複写による実費頒布をおこなっております。

This report is issued irregularly.
Inquiries about availability of the reports should be addressed to Research Information Division, Department of Intellectual Resources, Japan Atomic Energy Research Institute, Tokai-mura, Naka-gun, Ibaraki-ken, 319-1195, Japan.

編集兼発行　　日本原子力研究所

Energy Confinement and Transport of H-mode Plasmas in Tokamak

Hajime URANO

Department of Fusion Plasma Research
Naka Fusion Research Establishment
Japan Atomic Energy Research Institute
Naka-machi, Naka-gun, Ibaraki-ken

(Received December 7, 2004)

A characteristic feature of the high-confinement (H-mode) regime is the formation of a transport barrier near the plasma edge, where steepening of the density and temperature gradients is observed. The H-mode is expected to be a standard operation mode in a next-step fusion experimental reactor, called ITER – the International Thermonuclear Experimental Reactor. However, energy confinement in the H-mode has been observed to degrade with increasing density. This is a critical constraint for the operation domain in the ITER. Investigation of the main cause of confinement degradation is an urgent issue in the ITER Physics Research and Development Activity. A key element for solving this problem is investigation of the energy confinement and transport properties of H-mode plasmas. However, the influence of the plasma boundary characterized by the transport barrier in H-modes on the energy transport of the plasma core has not been examined sufficiently in tokamak research. The aim of this study is therefore to investigate the energy confinement properties of H-modes in a variety of density, plasma shape, seed impurity concentration, and conductive heat flux in the plasma core using the experimental results obtained in the JT-60U tokamak of Japan Atomic Energy Research Institute. Comparison of the H-mode confinement properties with those of other tokamaks using an international multi-machine database for extrapolation to the next step device was also one of the main subjects in this study.

Density dependence of the energy confinement properties has been examined systematically by separating the thermal stored energy into the H-mode pedestal component determined by MHD stability called the Edge Localized Modes (ELMs) and the core component governed by gyro-Bohm-like transport. It has been found that the pedestal pressure imposed by the destabilization of ELM activities led to a reduction in the pedestal temperature with increasing density.

The core temperature for each species, in turn, decreased only by an approximately constant factor with a reduction in the pedestal temperature, resulting in deterioration of the energy confinement of the plasma core. It has been demonstrated that the edge pedestal structure imposed by ELM instabilities plays a significant role as a boundary condition in determining the heat transport of the plasma core.

Hence, a higher pedestal temperature is required to improve the energy confinement in H-mode plasmas. It has been observed pervasively that high triangularity and/or argon seeded ELMy H-mode plasmas are capable of producing improved energy confinement. The present study showed that the improved performance in such discharges could also be explained by the higher pedestal temperature through the same mechanism seen in the standard ELMy H-mode plasmas shown above.

The effects of conductive heat flux in the plasma core on energy confinement has been analyzed in low and high triangularity discharges with changes in the neutral bean injection (NBI) power and in argon seeded discharges where the enhancement of radiation loss power due to argon gas injection changes the conductive heat flux profile. As the heat flux in the plasma core was varied in these plasmas, heat diffusivity adjusted itself to sustain the edge-core proportionality in temperature profiles.

The role of the pedestal temperature as a boundary condition for core confinement in other tokamaks has been compared to its role in JT-60U by using an international multi-machine pedestal database. Increasing the triangularity has been shown to be a possible method for maintaining high pedestal temperature in high density discharges and thus attaining high energy confinement in a next-step experimental device.

In this study, the energy confinement and transport properties of H-mode plasmas have been investigated from the viewpoint of plasma edge structure in various operation conditions. The decisive factor determining the core heat transport, which is a main argument in H-mode physics research, has been identified. Optimized operation conditions and methods to sustain enhanced energy confinement performance have also been investigated quantitatively. This thesis makes an important contribution to one of the most critical issues in the ITER Physics Research and Development Activity and, more widely, in tokamak fusion research.

Keywords: H-mode, ELM, Edge Pedestal, Profile Stiffness, Energy Confinement, Transport, Heat Flux, Boundary Condition, High Density, Triangularity, Argon Gas Injection, High β_{pol} H-mode, Multi-machine Pedestal Database, ITER, JT-60U

トカマクにおけるHモードプラズマのエネルギー閉じ込めと輸送

日本原子力研究所 那珂研究所 炉心プラズマ研究部
浦野　創

(2004年12月7日受理)

次世代の核融合研究開発の世界的な中枢を担う国際熱核融合実験炉 ITER では、炉心プラズマの周辺部に形成される輸送障壁によって閉じ込めが改善される高閉じ込めモード（Hモード）を標準運転モードとしている。しかし、この放電モードではプラズマの密度が増加するのに伴って、エネルギー閉じ込め性能が低下する傾向があるため、ITER におけるプラズマ密度の運転領域を大きく制限している。現在この原因を究明することは、ITER 物理 R&D 活動における最重要課題にも挙げられている。この課題解決のためには、Hモードプラズマのエネルギー閉じ込め特性を解明することが重要であるが、Hモードにおいて輸送障壁が形成されるプラズマ境界部によるコアプラズマの輸送へ及ぼす影響については未だ十分な研究がされていない。そこで本研究では、日本原子力研究所の臨界プラズマ試験装置 JT-60U の実験結果を用いて、Hモードプラズマのエネルギー閉じ込め特性のプラズマ密度依存性、プラズマ形状効果、不純物ガス導入の効果及びコアプラズマの熱流束の影響をそれぞれ解明することを目的とした。また国際マルチマシンデータベースを用いて、JT-60U における Hモードの閉じ込め特性の他装置との比較も本研究の目的とした。

Hモードプラズマを乱流輸送が支配するコア部と MHD 不安定性が支配するペデスタル部（Hモード化による圧力分布の嵩上げ部）に分離することによって、エネルギー閉じ込め特性のプラズマ密度依存性を解析した。ペデスタル部のプラズマ圧力（密度×温度）は、境界プラズマに局在する不安定性(Edge Localized Mode; ELM)によって、プラズマ密度に依らずほぼ一定に保たれ、プラズマ密度を増加させると、ペデスタル部の温度が低下することが分かった。さらに、このペデスタル部の温度の低下に比例して、コアプラズマ部の温度が低下し、エネルギー閉じ込め性能は低下することを示した。これにより、ペデスタル構造が、コアプラズマ部の熱輸送を決定する境界条件として重要な役割を果たすことを明らかにした。

従って、エネルギー閉じ込め性能を改善するためには、ペデスタル部の温度を増加させる必要がある。高プラズマ密度領域における閉じ込め改善を狙った運転

那珂研究所：〒311-0193 茨城県那珂郡那珂町向山 801−1

方法として、プラズマの高三角度化及び周辺部の放射損失の増大を伴う不純物注入等が報告されている。本研究では、これらの放電の閉じ込め特性もペデスタル部の温度上昇がコア部のエネルギー閉じ込め性能を向上させるという上記のメカニズムによって説明できることを示した。

次に、エネルギー閉じ込めに対するコア部の熱流束の影響を解析すべく、中性粒子ビーム(NBI)加熱パワーを変えた低三角度及び高三角度の重水素プラズマ放電、及びアルゴン入射による放射損失強度の増大によって、コア部の熱流束を変化させる放電を行った。これらの放電においてもコアプラズマの熱流束が増加（減少）すると、ペデスタルーコア間の比例関係を持つ温度分布を一定に保つように熱拡散係数が増加（減少）することが分かった。

最後に、国際マルチマシンデータベースを用いて、他のトカマク装置についてもエネルギー閉じ込め性能に対するペデスタル温度の境界条件としての役割を解析した。三角形度を大きくとることは高密度領域で高いペデスタル温度及び高いエネルギー閉じ込め性能を維持できるので、将来の核融合炉において適した運転手法であることを示した。

本研究では、H モードプラズマのエネルギー閉じ込め特性を境界プラズマの観点から様々な放電条件下で解析した。本論文は、その中心的課題であるプラズマ中心部の熱輸送を決定する主要なファクターを抽出し、高性能のプラズマを維持するための最適化された運転条件・手法を定量的に明確にしたものであり、ITER 物理 R&D 活動及び広くトカマク炉開発の最重要課題の解決に貢献するという重要な意義をもつ。

Contents

1. Introduction **1**

2. JT-60U and ITER **10**

2.1. Tokamak Research 10

2.2. JT-60U 12

2.2.1. Program of JT-60U 12

2.2.2. Auxiliary Heating System 14

2.2.3. Diagnostics 16

2.3 ITER 17

3. Thermal Energy Confinement of ELMy H-mode Plasmas **23**

3.1. Introduction 23

3.2. Operating Regime of ELMy H-mode Discharge 25

3.3. Thermal Energy Confinement 27

3.3.1. Density Dependence of Thermal Energy Confinement Time 30

3.3.2. Pedestal Structure during ELMy H-mode 39

3.3.3. Correlation between the Core and Edge Pedestal Confinement 45

3.4. Discussions 48

3.5. Conclusions 50

4. Thermal Energy Confinement of High Triangularity ELMy H-mode Plasmas **51**

4.1. Introduction 51

4.2. Experiment of High Triangularity ELMy H-mode 52

4.3. Thermal Energy Confinement Properties 55

4.4. Pedestal Characteristics 59

4.5. Boundary Condition for Thermal Energy Confinement 63

4.6. High β_{pol} H-mode Plasmas 66

4.7. Conclusions 73

5. Thermal Energy Confinement of Argon Seeded ELMy H-mode Plasmas 74

5.1. Introduction 74

5.2. Experiments of ELMy H-mode Discharges with and without Argon Gas Injection 77

5.3. Thermal Energy Confinement Properties 80

5.4. Pedestal Characteristics 88

5.5. Boundary Condition for Core Confinement 89

5.6. Conclusions 93

6. Effects of Heat Flux on Temperature Profiles 95

6.1. Introduction 95

6.2. Experiments 96

6.3. Effects of Triangularity on Plasma Boundary and Core Transport 97

6.4. Effects of Argon Gas Injection on Plasma Boundary and Core Transport 102

6.5. Discussions 105

6.6. Conclusions 106

7. Multi-machine Database Analysis of H-mode Plasmas 107

7.1. Introduction 107

7.2. Multi-machine Pedestal Database 108

7.3. Plasma Magnetic Geometry 109

7.4. Boundary Condition for Core Confinement 110

7.5. Conclusions 117

8. Conclusions 118

Acknowledgements 124

References 125

目　次

1. 序論 1

2. JT-60U と ITER 10

2.1. トカマク研究 10

2.2. JT-60U 12

2.2.1. JT-60U 計画 12

2.2.2. 外部加熱装置 14

2.2.3. 計測器 16

2.3. ITER 17

3. ELMy H モードプラズマの熱エネルギー閉じ込め特性 23

3.1. 序論 23

3.2. ELMy H モード運転領域 25

3.3. 熱エネルギー閉じ込め特性 27

3.3.1. 熱エネルギー閉じ込め時間の密度依存性 30

3.3.2. ELMy H モードのペデスタル構造 39

3.3.3. 周辺ペデスタルと炉心プラズマの閉じ込めの関係 45

3.4. 議論 48

3.5. 結論 50

4. 高三角度 ELMy H モードプラズマの熱エネルギー閉じ込め特性 51

4.1. 序論 51

4.2. 高三角度 ELMy H モード実験 52

4.3. 熱エネルギー閉じ込め特性 55

4.4. ペデスタル特性 59

4.5. 熱エネルギー閉じ込めに対する境界条件 63

4.6. 高 β_{pol} H モードプラズマ 66

4.7. 結論 73

5. アルゴン入射 ELMy H モードプラズマの熱エネルギー閉じ込め特性 74

5.1. 序論 74

5.2. ELMy H モード実験（アルゴン入射の有無） 77

5.3 熱エネルギー閉じ込め特性 80

5.4. ペデスタル特性 88

5.5. 炉心プラズマの閉じ込めに対する境界条件 89

5.6. 結論 93

6. 温度分布に対する熱流束の影響 95

6.1. 序論 95

6.2. 実験 96

6.3. プラズマ境界および炉心の熱輸送に対する三角度の影響 97

6.4. プラズマ境界および炉心の熱輸送に対するアルゴン入射の影響.....102

6.5. 議論 105

6.6. 結論 106

7. H モードプラズマのマルチマシンデータベースを用いた検討 107

7.1. 序論 107

7.2. マルチマシンペデスタルデータベース 108

7.3. 磁場構造 109

7.4. 炉心プラズマの閉じ込めに対する境界条件 110

7.5. 結論 117

8. 結論 118

謝辞 124

参考文献 125

1. Introduction

Nuclear fusion is expected to be a possible large contributor to the energy source in the next generation, from the viewpoint of a virtually inexhaustible fuel supply, safety characteristics and an acceptable environmental impact. The continuing population growth and the growing economic aspirations of all mankind combined with the increasing international concern over the potential climatic threat from dependence on fossil fuels have led to the demand for a range of practical energy options for a sustainable energy supply. Establishing the fusion energy option would make a critical contribution to the welfare of future society.

The major research on controlled nuclear fusion has been mostly focused on the use of magnetically confined plasma to produce a sufficiently high fusion reaction rate. Ignition, where, as with fossil fuels, the burning process becomes self-sustaining without further applied heating, is an essential requirement for the operation of thermonuclear fusion reactors. The progress toward ignition can be measured by means of the product of energy confinement time, temperature and density, which corresponds to the ratio of the fusion power ($\propto n_i^2(0)\, T_i^2(0)$) to the loss power ($\propto n_i(0)\, T_i(0) / \tau_E$). Here, $n_i(0)$ and $T_i(0)$ are the central ion density and temperature of the plasma, respectively, and τ_E is the energy confinement time. The form of the dependence of the fusion cross-section on energy fortuitously allows the requirement for ignition to be expressed by

$$n_i(0)\tau_E T_i(0) \geq 5\times10^{21}\,\mathrm{m^{-3}\cdot sec\cdot keV} \qquad (1.1)$$

The reactor plasma must therefore achieve high energy confinement with sufficiently high pressure. Although the required density, temperature and energy confinement time have all been obtained in tokamaks, they have not been achieved

simultaneously. To satisfy thermonuclear conditions in a tokamak, τ_E should be large enough at a sufficiently high density.

Several schemes of magnetic confinement systems, such as a tokamak, stellarator, reversed field pinch, Z-pinch and mirror, have been developed towards a thermonuclear fusion reactor. In particular, research on magnetic confinement based on a tokamak has progressed significantly. The tokamak is the magnetic confinement system currently best developed to allow confident extrapolation into ignition regimes.

Impressive progress throughout the magnetic controlled fusion research programs has reached a stage where a tokamak burning plasma facility can be seriously contemplated as an appropriate next step. In this facility, the thermonuclear heating balances (or is comparable to) transport and radiation losses for periods of 1000 sec or longer. Achieving this goal would be a major step forward, both in science and in technology, towards the ultimate goal of magnetic fusion generation of electrical power with significant environmental advantages [1,2]. The leading large tokamak experiments have achieved the break-even of reactor conditions, under deuterium-tritium (D-T) operation in JET of the Culham Laboratories in the United Kingdom [3,4] and under deuterium-deuterium (D-D) operation in JT-60U of Japan Atomic Energy Research Institute in Japan (based on calculations of the predicted fusion reactivity in a 50:50 mixture of deuterium and tritium under the same plasma conditions) [5-9].

Many of the problems of fusion research have been overcome in tokamaks. It is now necessary to look to the future and the next stage of tokamak development. In terms of plasma performance, this must include a tokamak which is capable of achieving extended burn in inductively driven plasmas at $Q > 10$ (where Q denotes the fusion power gain) and of demonstrating steady-state operation through current drive at $Q > 5$, while not precluding the possibility of controlled ignition [10,11]. Such an enterprise will concentrate effort on the

critical problems and, if successful, demonstrate the feasibility of a tokamak reactor. There is already worldwide co-operation in an international team, whose task is to design a tokamak which will satisfy the above conditions and produce power in the gigawatt range, and the engineering design of such a tokamak was completed in July 2001. This large-scale tokamak, the purpose of which is to demonstrate the scientific and technological feasibility of fusion energy, is called ITER – the International Thermonuclear Experimental Reactor [12].

However, there were serious problems in early era of tokamak research. In confinement studies based on the limiter configuration, the energy confinement time was unfortunately found to be a decreasing function of both density and temperature. As power was applied to the plasma the energy confinement time fell [13]. These results were disappointing and seemed to be an obstacle which could not be overcome. Using the empirical scaling derived from a range of experiments, it was predicted that the energy confinement time would improve with size of tokamaks and the associated higher plasma currents. On the basis of these confinement qualities called the L-mode, a tokamak reactor would require a large value of $A \times I_p$ of more than 100 MA, where A is the aspect ratio and I_p is the plasma current. This value is too large from the economic and engineering viewpoints. Therefore, improved confinement must be achieved in the fusion plasmas.

A fortunate discovery made in auxiliary heated discharges on the ASDEX tokamak [14,15] was on the existence of a mode of plasma operation in which the energy confinement time is typically twice longer than that of the previous 'normal' operation. This is called the H-mode in contrast with a normal regime called the L-mode. The transition to this state of higher confinement was found in a plasma with a divertor and at a sufficiently high level of plasma heating. The transition occurs abruptly and appears to be associated with improved energy confinement at the plasma edge (see figure 1.1).

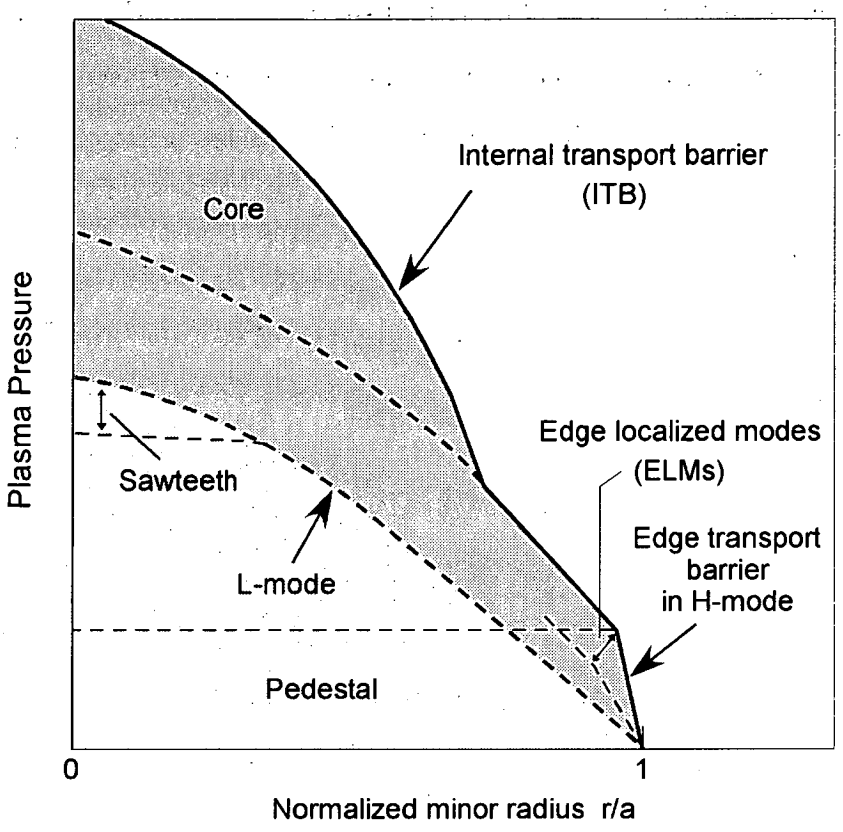

Figure 1.1 Schematic representations of the pressure profiles in L-mode and H-mode (ELMy H-mode). A profile of ELMy H-mode plasma with an internal transport barrier (ITB) is also shown.

H-mode plasmas produce steep gradients of density and temperature in the edge region, and because of the steep edge pressure gradient, MHD instabilities so-called Edge Localized Modes (ELMs) [16-19] are driven. These instabilities are accompanied by rapid bursts of MHD activity with poor plasma confinement and producing large heat and particle fluxes to plasma-facing surfaces. However, from the viewpoint of steady-state operation, the H-mode accompanied with ELMs (ELMy H-mode) is considered to be desirable for particle control as they expel impurities, including helium ash [20], and stabilize the core plasma density, although the energy confinement performance is slightly degraded by them. The ELMy H-mode has been chosen over other modes as the

primary principal operating mode for ITER. It has now been seen on a wide variety of magnetic confinement devices under a wide range of conditions. The feature of improved core confinement is sometimes combined with that of H-mode, and higher performance of the energy confinement has been attained through this combination.

There has been considerable development of databases and accumulation of knowledge of the behavior of tokamak plasmas around the world, making it possible to design an experimental fusion reactor such as ITER. However, a significant uncertainty still exists in predicting the energy confinement properties and plasma performance in such a device.

A precise theory of classical collisional transport losses is established. Since this theory does not completely explain the transport process across magnetic surfaces, an additional transport process driven by plasma turbulence must be taken into account. Significant theoretical efforts are being devoted to understanding the cross-field transport in tokamaks due to turbulence, and a few models are broadly consistent with present experiments. On the other hand, since tokamaks of various sizes and with various operating parameters and heating powers have been constructed, empirical scaling laws derived from these tokamaks are useful for predicting plasma performance of a new device.

The main strength of the empirical energy confinement scaling method is its simplicity and the fact that all of the physical processes are contained within the data. Its main weakness is that modeling of the energy confinement time, τ_E, by a simple log-linear form, or even by more sophisticated forms, can only, at best, be a very approximate description of the physical processes taking place, since no knowledge of the heating, temperature or density profiles, or atomic physics for that matter, is built into the analysis. The log-linear form itself is equivalent to assuming that a single turbulence mechanism is responsible for the transport. This seems unlikely to be the case for the ELMy H-mode, the operational mode

foreseen for ITER, where the core region may be dominated by short wavelength turbulence of the gyro-Bohm type, and the behavior in the edge region is possibly determined by MHD events such as the edge localized modes (ELMs).

In the ITER Physics Basis (IPB) report [21], several empirical log-linear (power law) scaling expressions for thermal energy confinement time, τ_{th}, are presented. According to these scaling laws, τ_{th} is expected to increase with density. As a result, high thermal energy confinement could be achieved in the high density regime. However, high density operations conducted in many tokamaks have indicated that, when the density exceeds a certain value, the positive density dependence for the thermal energy confinement time expected by the scaling laws does not describe correctly the variations of τ_{th} of ELMy H-mode plasmas. Those scaling laws predict higher energy confinement than that observed experimentally, indicating that improved energy confinement leads to high density.

In recent tokamak research, extension of the maximum density at which high energy confinement can be sustained is a critical issue. Since the energy losses associated with the ELM activities are of a serious concern for the lifetime of the divertor target [22-24], high density operation is also indispensable for reducing the peak power load onto the divertor plate by high radiation power loss in the scrape-off layer (SOL) and divertor region. However, it has been difficult to maintain H-mode confinement at densities close to the Greenwald value, n^{GW} [10^{20} m^{-3}] ($\equiv I_p$ [MA] / πa_p^2 [m]) with gas puff fueling [25]. Although degradation of the energy confinement at high density is a common feature of the ELMy H-mode plasmas in many tokamaks, the critical density above which the energy confinement starts to degrade differs in different devices or equilibrium configurations.

The physics mechanism of core energy confinement above the critical density is presently not known. There are several issues which should be solved one by one to achieve high density and high energy confinement simultaneously.

In this study, through experiments using the JT-60U tokamak, the confinement and transport properties in H-mode plasmas are examined in the following order:

(1) Systematic analysis of the confinement and pedestal characteristics in ELMy H-mode plasmas by separating thermal stored energy into the H-mode pedestal and core components

(2) Investigation of the physics underlying the confinement degradation with increasing plasma density and identification of the dominant boundary factor determining the core energy confinement

(3) Examination of the edge-core relationship in alternative advanced operation modes (high triangularity and/or argon seeded ELMy H-modes) which are capable of producing high energy confinement at high density

This thesis is organized as follows. In chapter 2, an outline of the JT-60U tokamak and the required operating regime in the ITER are presented. The relevant engineering instruments used in the JT-60U tokamak, such as additional heating systems and diagnostics, are also described.

In chapter 3, the thermal energy confinement properties in ELMy H-mode plasmas are described for the case of the JT-60U tokamak. Based on the results of low triangularity experiments (δ_x = 0.16-0.19, where δ_x denotes triangularity at the separatrix), the density dependence of the thermal energy confinement is discussed in terms of the H-mode pedestal and core components. It is therefore made clear whether the confinement degradation on the basis of the H-mode confinement scaling law is attributed to the core or pedestal deterioration. The H-mode pedestal characteristics are also described for a wide range of densities. The relationship between pedestal structure and core transport based on the experimental observations is of a significant concern. The role of the pedestal structure as a boundary condition for the core confinement is discussed from the viewpoint of temperature profile effects.

In chapter 4, the thermal energy confinement properties and pedestal characteristics of high triangularity ELMy H-mode plasmas, which are being considered as a means for improving the energy confinement, are described. High triangularity discharges, in which the critical edge pressure gradient (edge α-parameter) can be raised, have been found to result in high energy confinement of the plasma core [26-31]. In this chapter, the density dependence of the energy confinement improved by high triangularity configuration is shown quantitatively. The H-mode pedestal characteristics of low and high triangularity discharges are compared. In JT-60U, high energy confinement plasmas, so-called high poloidal-beta (β_{pol}) H-mode [32,33], have been obtained with improved core confinement at high triangularity. In these plasmas an internal transport barrier (ITB) is formed. The ion heat diffusivity, χ_i, substantially decreases in the plasma core region down to the neoclassical level [34]. Across the ITB, the ion temperature increases by several keV. The pedestal and core confinement properties of high β_{pol} H-mode discharges with the ITB are also described in this chapter.

As an alternative operation method aimed at improved confinement in the high density regime, it has been reported that externally puffed seed impurity is of great use to the energy confinement improvement with high radiation loss power [35-38]. In chapter 5, the energy confinement and H-mode pedestal properties in argon gas injected discharges are described. The influence of pedestal structure on energy confinement improvement due to argon gas injection is shown by comparing with H-mode discharges only with deuterium gas puffing.

In chapter 6, the effects of conductive heat flow on energy transport concerning the temperature profile similarity are described for H-mode plasmas heated by neutral beam (NB) injection. In standard H-mode plasmas at low and high triangularity, the responses of the edge-core relationship on temperature profiles and its corresponding heat diffusivity in a variety of heat flux in the plasma core using NB injection are discussed. The heat transport mechanisms of

the plasma core are analyzed in argon gas puffed plasmas where the enhancement of the radiation loss power due to argon gas injection varies the conductive heat flux at a fixed NB injection power.

It has been observed in many tokamaks that the characteristics of the H-mode edge pedestal are crucial for characterizing the confinement and stability properties of the core plasma and for quantifying the effect of ELM energy load on divertors. To investigate the universal characteristics of the edge pedestal, an international multi-machine pedestal database has been developed [39]. In chapter 7, the relation of core confinement and pedestal parameters is described using the multi-machine pedestal database. The H-mode pedestal and core confinement properties in several tokamaks are compared, and the underlying physics of confinement degradation in high density ELMy H-mode plasmas are described.

Finally, in chapter 8, the main results of this study are summarized, and related issues for future study are presented.

2. JT-60U and ITER

2.1. Tokamak research

The tokamak was invented at the Kurchatov Institute in the Soviet Union, where the early development took place in the late 1950s. The successful development of the tokamak was principally the result of the careful attention paid to the reduction of impurities and the separation of the plasma from the vacuum vessel by means of a 'limiter'. This led during the 1960s to comparatively pure plasmas with electron temperatures of around 1 keV [40]. By 1970 these results were generally accepted and their significance appreciated and many tokamaks were constructed in the world [41]. Tokamak research concentration has led to a large scale world wide program.

As larger tokamaks were built the expected improvement in confinement was achieved and confinement times approaching 100 ms had been obtained by 1980. Since the simplest model consistent with experimental results gave $\tau_E \propto n a_p^2$, where n and a_p denote the density and the minor radius of the plasma, respectively, the design of large tokamak experiments was undertaken in several countries.

During the 1970s, although ohmic heating upon which the early experiments relied entirely becomes unfortunately less effective at higher temperature because the electrical resistively of the plasma falls as the electron temperature increases, varying as $T_e^{-2/3}$, neutral particle injection and RF heating had been developed as the additional heating methods to achieve success. Both methods had achieved temperatures of several keV in the early 1980s.

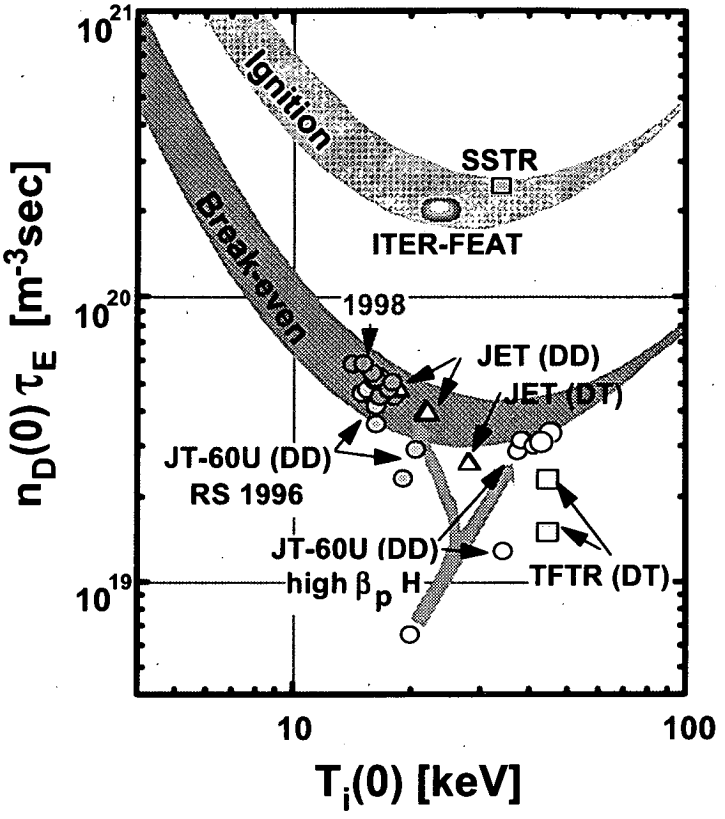

Figure 2.1 Development of confinement experiments in $n_D(0)\ \tau_E - T_i(0)$, where $n_D(0)$ denotes the central deuterium density, τ_E is the energy confinement time, and $T_i(0)$ is the central ion temperature.

In 1982, it was discovered in ASDEX [14,15] that under certain conditions there is a discontinuous improvement in confinement as the heating power is increased. Typically there is a factor of two increase in the energy confinement time. This regime is called the H-mode. The H-mode was also identified in other tokamaks. In addition to the H-mode characterized by an edge transport barrier (ETB), a number of other improved confinement regimes with an internal transport barrier (ITB) have also been identified.

By the early 1980s, three large tokamaks: TFTR in Princeton Plasma Physics Laboratory, United States of America (programs finished in 1997); JET in Culham Laboratories, United Kingdom; JT-60 of the Naka Fusion Research Establishment in Japan Atomic Energy Research Institute, Japan, were constructed

Table 2.1 The main parameters and dimensions of the JT-60U plasma

Plasma current (I_p)	5.0 MA
Toroidal magnetic field (B_t)	4.2 T
Discharge duration time	15 sec
Plasma major radius (R_p)	3.0-3.4 m
Plasma minor radius (a_p)	0.6-1.1 m
Vertical elongation at the separatrix	1.4-1.7
Plasma volume (V_p)	40-100 m^3
Main auxiliary heating (NBI, ICRF, LHRF, ECRF)	55 MW

to satisfy the Lawson criterion. Up to the present, the JET and JT-60 achieved the break-even plasma condition and TFTR and JET have successfully gained the fusion power up to 16 MW in actual deuterium-tritium mixture discharges as is shown in figure 2.1 [3-9,42,43].

2.2. JT-60U

2.2.1. Program of JT-60U

JT-60 (JAERI Tokamak-60), in which the first plasma was obtained in April 1985, was constructed as one of the large tokamak fusion experimental devices to contribute to the physics research and development of fusion plasma and the achievement of the break-even plasma condition [44]. The original JT-60 had an enclosed divertor chamber situated on the large major radius side of the plasma. It was however found that this configuration did not allow H-mode operation, and the poloidal circuit was modified in early 1988 to permit the formation of an X-point in the bottom of the vacuum vessel. This constituted an interim step in a much more extensive modification of the tokamak, which began in late 1989. The vacuum vessel was replaced, eliminating the original divertor,

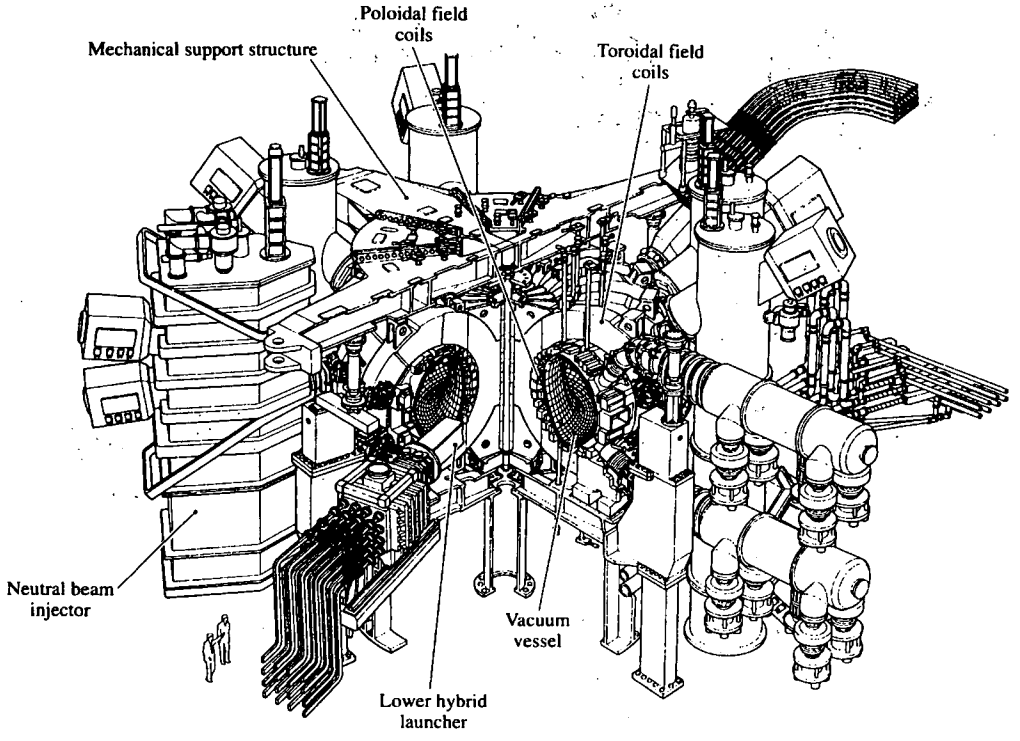

Figure 2.2 Bird's eye view of JT-60U tokamak device

and the poloidal circuit was extensively upgraded within the existing toroidal field coil set. In order to distinguish the remodeled machine from the previous JT-60, it is called JT-60U (JT-60 Upgrade). The divertor of JT-60U was also modified from an open divertor to a W-shaped divertor with pumps in 1997 [45].

The operational parameters of JT-60U are summarized in table 2.1. An overall schematic of the JT-60U device is shown in figure 2.2. The electric power of ~1.3 GW required to operate JT-60U experiment for exciting magnetic field coils, producing plasma and heating plasma is supplied by three motor generators. Most of required power is accumulated before the discharge pulse in these electrically powered generators with the form of rotation energy and at the plasma discharge all the power are released together with directly received commercial electric power. The JT-60U device is capable of operating at hydrogen, deuterium

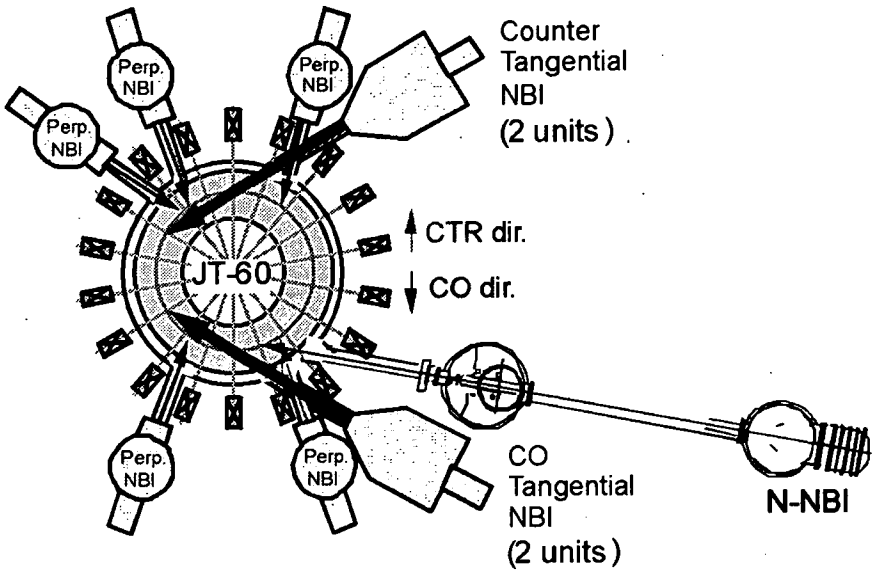

Figure 2.3 NBI heating system of JT-60U tokamak device

and helium gases. The first wall is completely lined with graphite, especially with carbon fiber composite (CFC) tiles in the divertor target.

2.2.2. Auxiliary heating system

The ohmic heating, acceleration by the toroidal electric field induced by transformer action heats the plasma up to temperature of a few keV. The ohmic heating power degrades as the temperature increase with a $T_e^{-3/2}$ dependence of the plasma resistivity. To achieve temperature larger than 10 keV, additional heating such as neutral beam injection (NBI) and radio-frequency (RF) heating are used. In the former, to penetrate through the magnetic field in a tokamak, high energy neutral atoms are injected into the plasma. In radio-frequency heating, high power microwaves are injected into the plasma and heat plasma by resonant interactions.

The neutral beam injection (NBI) into JT-60U is composed of two systems (see figure 2.3). One is a positive-ion based NBI (14 units) and the other

is a negative-ion based NBI (1 units). The NB heating system for the JT-60U started the beam injection operation in 1986 with hydrogen beam. All the original neutral beam lines were perpendicular injection. In 1990-1991, four beam lines out of 14 units were modified from perpendicular to tangential injection. At the same time, a modification was made to enable deuterium operation.

The positive-ion based NBI system is capable of injecting up to 40 MW at 85-90 keV for ~10 s with deuterium. On the other hand, the negative-ion based NBI system, which is aiming at 10 MW at 500 keV, is composed of one beam line with two ion sources and a set of high voltage power supply.

In radio-frequency (RF) heating, high power microwaves are injected into the plasma and impart energy by resonant interactions. Three main schemes are currently exploited in JT-60U, which are composed of ion cyclotron resonance heating (ICH), lower hybrid resonance heating (LHH) and electron cyclotron resonance heating (ECH). In the ICH system the frequency is chosen to resonate at the cyclotron frequency or its harmonics, 110-130 MHz, $2\Omega_{CH}$ = 116 MHz at B_t = 3.8 T. In the LHH system at 1.74-2.23 GHz, the waves undergo Landau damping by either electrons or ions depending on density. The ECH system at 110 GHz consists of three gyrotrons and designed to couple the fundamental O-mode from the lower field side, which is the proposed scheme for EC current drive in ITER. The design pulse length of the ICH and LHH systems is ~10 s, the heating capability is 6 MW of ICH and 7 MW of LHH. The ECH system is capable of achieving a torus input of 1.5 MW for 3 s [46]. Radio-frequency heating has an advantage of flexible control of the heating profile since the cyclotron absorption occurs around one value of the magnetic field. Radio-frequency waves can also be used for driving current.

Table 2.2 Summary of the main diagnostic systems in JT-60U

Plasma parameter	Diagnostics
Ion temperature	Charge exchange recombination spectroscopy (CXRS)
Electron temperature	Thomson scattering with Ruby laser system
	Thomson scattering with YAG laser system
	Electron cyclotron emission (ECE) Diagnostics
Electron density	Thomson scattering for Ruby laser system
	Thomson scattering for YAG laser system
	Far infrared (FIR) interferometer
	CO_2 laser interferometer
Plasma current profile	Motional stark effect (MSE)
Radiation	Bolometer
Effective charge number	Visible Bremsstrahlung
Magnetic fluctuation	Saddle coils
	Tangential magnetic probes

2.2.3. Diagnostics

In order to understand the physical processes occurring inside the plasma, the JT-60U tokamak is equipped with a comprehensive range of diagnostic systems. These measurements can be used to determine the general plasma parameters, to assess the fusion performance and for studies of specific plasma phenomena. The parameters most commonly monitored are the plasma stored energy, power input and output, temperature and density profiles of electrons and ions, magnetic field configuration and current profile, impurity emission intensity, divertor and edge plasma parameters. Diagnostic tools equipped in JT-60U are summarized in table 2.2.

2.3. ITER

The ITER project has its origin in the common recognition, among the leading fusion programs worldwide, of the need for a next-step experiment aimed at demonstrating the scientific and technological feasibility of fusion energy for peaceful purposes. Built on the performance advances of leading machines and the wider database including data from smaller machines, ITER prefigures the core of a working fusion reactor and is thus designed to embody the next-step machine that serves the imperatives for progress in future research.

The ITER collaboration was set up to provide its parties with the option to make the next, integrated step within the frame of a global collaboration in which participants could pool their accumulated scientific and technological expertise, share the burden of costs and secure a degree of political commitment consistent with the scope and time scale of the task. After a brief 'Conceptual Design Phase' (CDA), four parties – the European Union, Japan, the Russian Federation and the United States – embarked, in 1992, on the phase of 'Engineering Design Activities' (EDA) [12].

The focus of effort in the ITER-EDA since 1998 has been the development of a new design to meet revised technical objectives and a cost reduction target of about 50 % of the previously accepted cost estimate. Drawing on the design solutions already developed and qualified during the EDA and using the latest physics results and outputs from technology researched development projects, a new design of ITER has been developed which meets, in general, the revised objectives and provides acceptable margins against the unavoidable uncertainties in performance projections. As such the new ITER design [47], whilst having reduced technical objectives from its predecessor, will nonetheless meet the programmatic objective of providing an integrated demonstration of the

Table 2.3 The main parameters and dimensions of the ITER plasma

Total fusion power	500 MW (700 MW)
Q (fusion power/auxiliary heating power)	≥ 10
Average 14 MeV neutron wall loading	0.57 MW m^{-2} (0.8 MW m^{-2})
Plasma inductive burn time	≥ 300 sec
Plasma major radius (R_p)	6.2 m
Plasma minor radius (a_p)	2.0 m
Plasma current (I_p)	15 MA (17.4 MA)
Vertical elongation at 95% of the flux surface/separatrix	1.70/1.85
Triangularity at 95% of the flux surface/separatrix	0.33/0.49
Safety factor† at 95% flux surface (q_{95})	3.0
Toroidal field at 6.2 m radius (B_t)	5.3 T
Plasma volume (V_p)	837 m^3
Plasma surface	678 m^2
Installed auxiliary heating/current drive power	73 MW (100 MW)

† Measure of the pitch of the helical field lines

scientific and technological feasibility of fusion energy. The main parameters and overall dimensions of the ITER plasma are summarized in table 2.3 [11,48,49]. The table shows the parameters and dimensions for nominal operation; the figures in brackets represent the maximum values obtaining under specific limiting conditions, including, in some cases, additional capital expenditures. A cutaway view of the tokamak and sub-systems in the cryostat are shown in figure 2.4 [11,49].

The reference operating scenario for inductive operation in the ITER is the ELMy H-mode (i.e. operational mode with high energy confinement time and regular edge localized modes); and the rules and methodologies for the projections of plasma performance to the ITER scale are those established in the ITER Physics Basis (IPB) [21], which was developed from broadly-based experimental and modeling activities within the magnetic fusion programmes of the ITER parties.

From the statistical analysis of confinement results obtained in many tokamak devices, an expression of the energy confinement time for ELMy H-

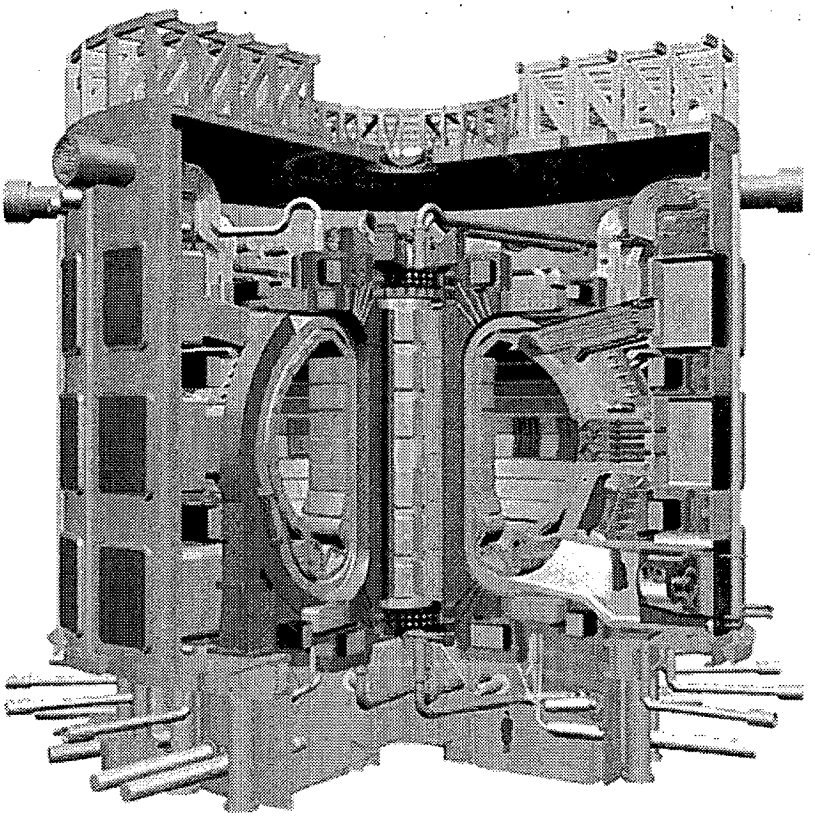

Figure 2.4 Cutaway view of ITER.

mode plasmas has been established as a function of plasma parameters, verified in time through three orders of magnitude, and expressed by the IPB98(y,2) scaling as [21]:

$$\tau_{th}^{IPB98(y,2)} = 0.0562 A_i^{0.19} I_p^{0.93} B_t^{0.15} R_p^{1.39} a_p^{0.58} \kappa_a^{0.78} n_e^{0.41} P_{loss}^{-0.69} \qquad (2.1)$$

where the units are s, amu, MA, T, m, 10^{19} m^{-3} and MW, respectively. In the above formula, A_i and P_{loss} denote the atomic mass of the ions and the total loss power crossing the separatrix corrected for the time derivative of the stored energy. The quantity κ_a is the plasma elongation defined as $\kappa_a = S_0 / \pi a_p^2$ with S_0 being the plasma cross-sectional area. In the IPB report [21], five empirical log-linear (power law) scaling expressions for thermal energy confinement time, τ_{th}, are presented which are derived from different subsets of the H-mode global

confinement database containing data from 13 tokamak devices. The IPB98(y,2) scaling has been selected as a conservative option. To represent either how close the actual value observed in one experiment is from the scaling, or a level of uncertainty, a scalar named the H_H-factor can be used. The H_H-factor describes the enhancement factor of thermal energy confinement time obtained experimentally, τ_{th}, based on the predicted standard ELMy H-mode confinement level. The $H_H^{IPB98(y,2)}$ is therefore given as follows:

$$H_H^{IPB98(y,2)} = \frac{\tau_{th}}{\tau_{th}^{IPB98(y,2)}} \tag{2.2}$$

Key limiting factors for inductive operation are normalized β (β_N), the density in relation to the Greenwald value (n_e/n^{GW}) [25], and the L-H mode power threshold (transition from the lower confinement mode of operation to the higher confinement mode). A range of possible plasma parameters at which Q = 10 by analyzing the possible operational domains in relation to the above limiting factors, for given values of Q, the plasma current and the H_H-factor ($H_H^{IPB98(y,2)}$) is illustrated in figure 2.5(a) and (b). The fusion power amplification, Q = 10 is maintained within the shaded region by adjusting auxiliary power and density. At a plasma current, I_p, of 15 MA, Q = 10 will be achieved at a fusion power, P_{fus}, of 400 MW with n_e/n^{GW} = 0.85, $H_H^{IPB98(y,2)}$ = 1 and β_N = 1.8. These parameters are still in conservative ranges. If necessary, a high field side pellet injector, stabilization of neoclassical tearing modes by the electron cyclotron (EC) current drive and/or mitigation of heat load due to ELMs will be applied for high fusion power operation up to ~ 700 MW with higher β_N, higher density and higher stored energy. The device also has a capability for Q = 10 operation at n_e/n^{GW} ~ 0.6 and β_N ~ 1.5 when $H_H^{IPB98(y,2)}$ = 1. Provided that energy confinement times consistent with the confinement scaling are maintained, the results show the flexibility of the design, its capacity to accommodate uncertainties in projection, and its ability to maintain the goal of extended burn Q = 10 operation, and also imply its ability to

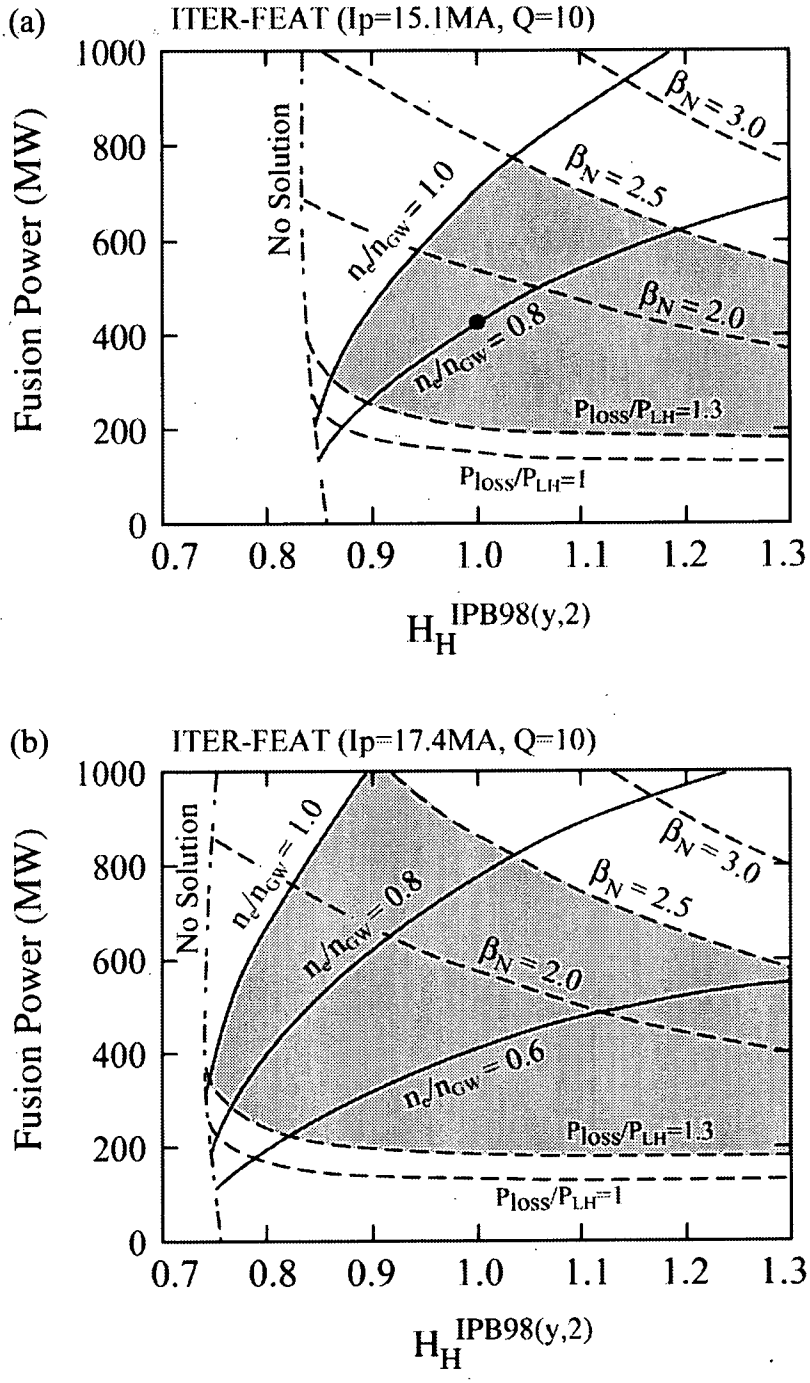

Figure 2.5 Q = 10 domain (shaded) for (a) I_p = 15.1 MA (q_{95} = 3.0) and (a) I_p = 17.4 MA (q_{95} = 2.6).

explore higher Q operation.

For the performance projection of ITER, there still remain uncertainties on the H-mode characteristics, such as energy confinement time scaling, H-mode power threshold scaling, non-dimensional transport, ELM model and so on. It has traditionally been difficult to maintain H-mode confinement at densities close to the Greenwald value. The extension of the maximum density at which high energy confinement can be sustained is also a critical issue. These issues are required to be studied on the present tokamaks as ITER physics research needs.

3. Thermal Energy Confinement of ELMy H-mode Plasmas

3.1. Introduction

High density operation with improved energy confinement is essential for a tokamak reactor to produce sufficiently high fusion power and to reduce heat load onto the divertor plates [22]. ITER [50,51] is envisaged to operate in the ELMy H-mode regime at a high density close to the Greenwald density limit, n^{GW} [25]. However, the H-factor, which describes the enhancement factor of the energy confinement from the L-mode level, has been observed to decrease with increasing plasma density in many experiments (e.g. in JET [52,53], ASDEX-Upgrade [54,55] and JT-60U [56,57]). Therefore the investigation of the dominant causes of this degradation is an urgent task in tokamak research for the extension of the improved energy confinement regime in the H-mode.

ELMs [16-19] are considered to affect the energy confinement mainly through two basic mechanisms. One is the direct energy loss from the region near the plasma boundary due to each burst. Type-I ELMs, which appear when higher levels of additional power than the H-mode threshold are applied, have the beneficial effect of regulating impurity content and density rise in a manner that has essentially allowed steady state operation, while the frequency of ELM bursts increases with heating power, and the energy loss produced by type-I ELMs reaches 1-10 % of total stored energy [18]. The other mechanism is the influence of the edge pedestal structure imposed by the destabilization of ELMs on the thermal energy confinement of the core plasmas. The stiff temperature profiles in

H-mode plasmas, which are evidence of an edge-core relationship, have been found in many devices [54,58-60]. The density dependence of thermal energy confinement should therefore be analyzed in terms of the core and pedestal properties.

In this chapter, the thermal energy confinement properties divided into core and pedestal components are examined in ELMy H-mode plasmas at low triangularity (δ = 0.16-0.19) for the case of JT-60U over the density range of 30-53 % of n^{GW}. The H-factor starts to decrease with density when the density is increased above a certain value. This reduction in the H-factor at high density is a common feature of ELMy H-mode plasmas in tokamaks although the critical density above which the H-factor starts to decrease depends on devices or equilibrium configurations, such as triangularity.

In order to understand the underlying physics of the reduction in the H-factor in the high density regime, the density dependence of the thermal energy confinement is analyzed for each component, and then the correlation between the pedestal characteristic parameter and the thermal transport of the core plasma is examined. The following research points will therefore be made clear. First, the dependence of thermal stored energy on plasma density is investigated. The reduction in the enhancement factor of the thermal energy confinement is due to the overestimated density dependence of the thermal stored energy in the scaling laws. The second point is whether the confinement degradation based on the H-mode confinement scaling law is attributable to core or pedestal deterioration. Density and temperature profiles are examined over the density range covered in the experiments. The third point is the pedestal characteristics during the H-mode regime. The variation in the shoulder of the pedestal temperature due to an increase in the pedestal density is analyzed in type-I and type-III ELMy H-mode plasmas. The dependence of the repetition frequency of ELMs on the absorbed power and plasma density is also of a significant concern. The fourth point is the

relationship between the pedestal structure and the core transport on the basis of the experimental observations in this study. The role of the pedestal structure as a boundary condition for the core confinement is analyzed from the viewpoint of the profile effects. This analysis sheds light on why the thermal stored energy does not increase with density as predicted by the scaling laws. The results could provide methods to raise the saturated value of the thermal stored energy (e.g. high triangularity configuration), resulting in a higher energy confinement at a given density.

The contents of this chapter are as follows. The operating regime of an ELMy H-mode discharge is presented in section 3.2. The thermal energy confinement properties divided into core and pedestal components are analyzed in section 3.3. The H-mode pedestal characteristics are also studied. The relationship between the edge pedestal and core plasmas during the type-I ELMy H-mode regime is discussed in section 3.4. The conclusions obtained from this study are given in section 3.5.

3.2. Operating regime of ELMy H-mode discharge

ELMy H-mode database analyzed in this chapter consists of a series of 36 discharges (shot 33635-33670) performed in JT-60U. The experiments were carried out at a plasma current, I_p = 1.8 MA, where n^{GW} corresponds to (8.1-8.7)$\times 10^{19}$ m^{-3}. The toroidal magnetic field, B_t = 3.0 T and the safety factor at the 95 % of flux surface, q_{95} = 2.9-3.1. The plasma configuration and viewing chords of the main diagnostics are shown in figure 3.1. The elongation, κ, of 1.48 to 1.55 and the triangularity, δ, of 0.16 to 0.19 were fixed. The plasma volume, V_p, was in the range of 60-63 m^3. The plasma major radius, R_p, and the minor radius, a_p, were in the ranges of 3.24-3.25 m and of 0.81-0.85 m, respectively. The spreads of n^{GW} and q_{95} are due to variations in the configuration parameters, such as a_p and R_p. A

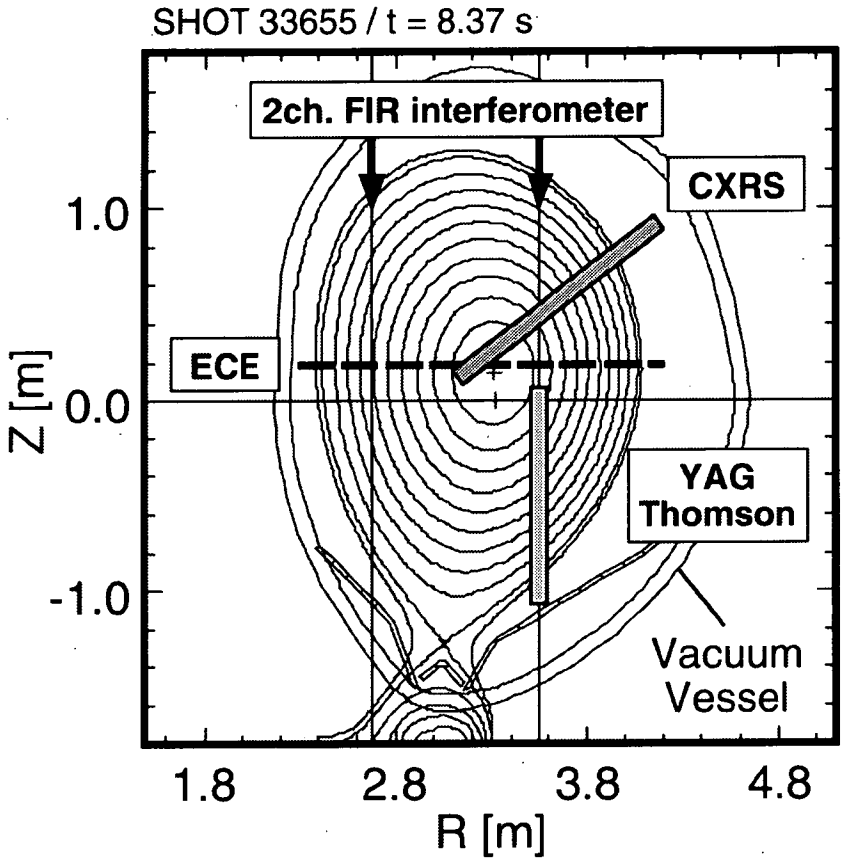

Figure 3.1 Sightlines and location of main diagnostics are illustrated on a cross-section of the plasma equilibrium.

neutral beam (NB) of deuterium was injected into a deuterium plasma, and the NB injection power, P_{NBI}, was varied in steps during a discharge from 4 to 13 MW. The line-averaged electron density measured with the far infrared (FIR) interferometer, $\bar{n}_e$ [61], was varied on a shot by shot basis from 2.4×10^{19} to 4.5×10^{19} m^{-3}. The maximum $\bar{n}_e$ reached was $(0.50\text{-}0.53)\times n^{GW}$. The experiments were operated so that the density could be kept almost constant at t = 6.0-8.5 s during a discharge. The density is increased by deuterium gas puffing at the beginning of a discharge, and then the particles were fuelled by the NB injection.

Radial profiles of the electron density, n_e, and electron temperature, T_e, were obtained by Thomson scattering measurements with a YAG laser system [62]. The core region T_e profiles were also measured using electron cyclotron emission

(ECE) data [63]. Ion temperature profiles, T_i, were measured with charge-exchange recombination spectroscopy (CXRS) [64]. The effective charge, Z_{eff}, was estimated using visible Bremsstrahlung and its profile was assumed spatially uniform so that these values were capable of reproducing the measured neutron emission rate, S_n [65].

Figure 3.2 shows the time evolution of plasma parameters in a pair of typical ELMy H-mode discharges with different densities. Type-III ELMs occurred at a heating power just above the threshold for L-H transition, and then type-I ELMs appeared with a further rise in the heating power, as seen in the D_α emission signals in the divertor region measured with the photomultiplier (PMT) array. In the higher density discharge (shot 33655; $\bar{n}_e = (3.0\text{-}3.8)\times 10^{19}$ m^{-3}), the global stored energy measured with the diamagnetic loop, W_{dia}, gradually increased to 2.9 MJ with increasing P_{NBI}, while in the lower density discharge (shot 33638; $\bar{n}_e = (2.3\text{-}2.8)\times 10^{19}$ m^{-3}), W_{dia} increased to 3.3 MJ. The energy confinement properties in the type-I ELMy H-mode phase, which appears when sufficiently high levels of additional power are applied, are analyzed at the time when the density and temperature profiles reached a quasi-steady state as shown in figures 3.3(a) and (b). Note that the plasmas analyzed in this paper are standard ELMy H-modes without an internal transport barrier (ITB) in the core.

3.3. Thermal energy confinement

It seems to be helpful to analyze the energy confinement properties in terms of (1) the thermal stored energy and (2) the thermal energy stored in the core and pedestal plasmas. In this paper, the orbit following Monte Carlo (OFMC) code [66] and the tokamak predictive and interpretation code system (TOPICS) [67] were used for the transport analysis of the fast ions and thermal plasma. The

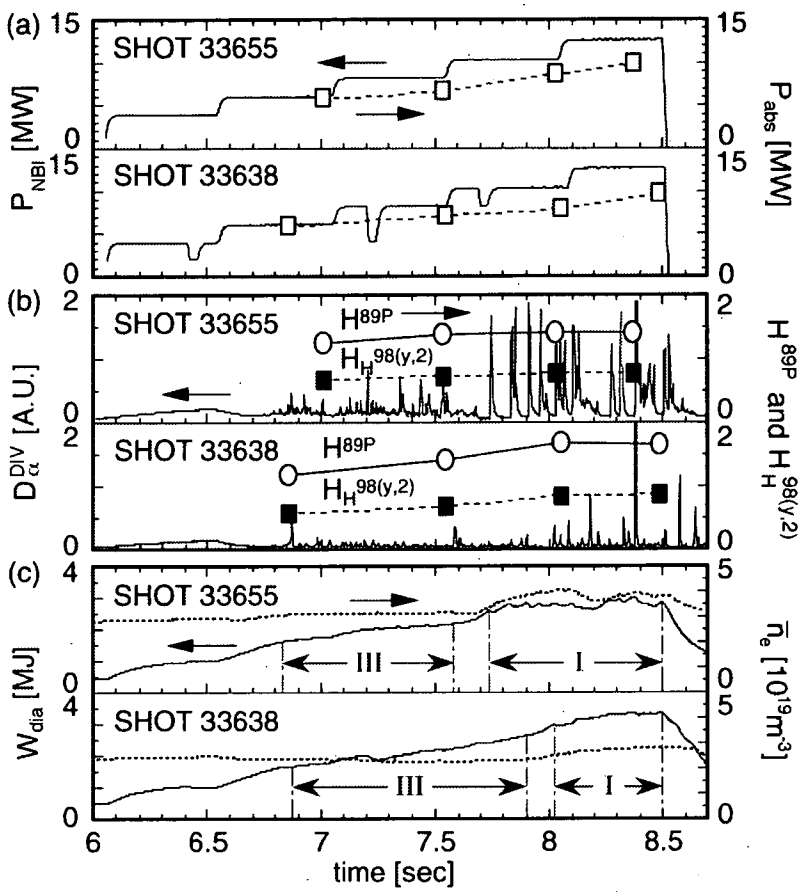

Figure 3.2 Time evolution of plasma parameters in the high and low density ELMy H-mode discharges (shots 33655 and 33638). (a) Neutral beam injection power, P_{NBI}, and absorbed power, P_{abs}; (b) D_α emission signals, the H-factor based on the ITER89P L-mode scaling, H^{89P}, and the H_H-factor against the IPB98(y,2) H-mode scaling; (c) the global stored energy, W_{dia}, and line-averaged electron density, $\bar{n}_e$.

confinement scaling laws used in this study as references for evaluation of these energy confinement properties are shown below.

The global stored energy is composed of the energy stored in the fast ions due to the NB injection, W_{fast}, and the thermal stored energy, W_{th}. In JT-60U, W_{fast}, is defined as the total energy of the fast ions, ranging from the injected energy in the range of 85-90 keV down to thermal ion energy of $1.25T_i$. The contribution of the fast ions varies with neutral beam energy, plasma electron temperature and density. To evaluate the performance of enhanced energy confinement discharges,

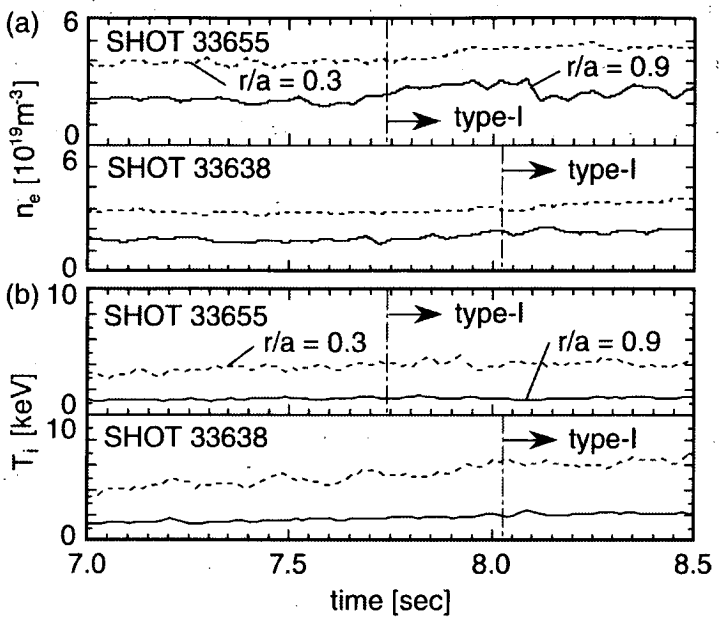

Figure 3.3 Time evolution of plasma parameters in the high and low density ELMy H-mode discharges at t = 7.0-8.5 s (shots 33655 and 33638). (a) Core and edge electron density (r/a = 0.3 and 0.9) obtained by Thomson scattering measurements with a YAG laser system; (b) core and edge ion temperature (r/a = 0.3 and 0.9) measured with charge exchange recombination spectroscopy (CXRS).

the energy confinement of fast ions and thermal plasma should be distinguished. As for the thermal energy confinement time, the IPB98(y,2) H-mode scaling was obtained from the ITER H-mode confinement database as follows [21]:

$$\tau_{th}^{IPB98(y,2)} = 0.0562 A_i^{0.19} I_p^{0.93} B_t^{0.15} R_p^{1.39} a_p^{0.58} \kappa_a^{0.78} n_e^{0.41} P_{loss}^{-0.69} \qquad (3.1)$$

where A_i is the effective mass number, P_{loss} is the total loss power to the plasma corrected for the time derivative of the stored energy given as $P_{abs} - dW/dt$ with P_{abs} being the absorbed power. The units are s, amu, MA, T, m, 10^{19} m^{-3} and MW, respectively.

For the empirical prediction of thermal energy confinement, a multi-machine confinement database has been developed and several scaling laws that can be used to calculate the expected performance of the standard operation

regime (ELMy H-mode) for ITER have been deduced [21,68-70]. In ELMy H-mode plasmas, the thermal stored energy can be divided further into the energy stored in the H-mode pedestal and core plasmas. In an offset non-linear (ONL) scaling for ELMy H-mode confinement [70], the pedestal component determined by the MHD stability of ELMs and the core component governed by the gyro-Bohm-like transport are separated as follows:

$$\tau_{th}^{ONL} = 0.082\kappa R_p a_p I_p B_t b^{-0.1} P_{loss}^{-1.0} + 0.043 R_p^{1.3} a_p I_p^{0.6} n_e^{0.6} b^{-0.15} P_{loss}^{-0.4} \qquad (3.2)$$

with $b \equiv B_t R_p^{1.25}$. The first and second terms represent the pedestal and core components, respectively.

3.3.1. Density dependence of thermal energy confinement time

The global energy confinement time, τ_E, is given by the following energy balance equation, in which W_{dia} includes the stored energy of the fast ions, W_{fast}, and of the thermal plasma, W_{th}:

$$\frac{dW_{dia}}{dt} = P_{abs} - \frac{W_{dia}}{\tau_E} \qquad (3.3)$$

$$P_{abs} = P_{NBI} + P_{ohmic} - P_{sh} - P_{orbit} - P_{ripple} \qquad (3.4)$$

where P_{ohmic} denotes the ohmic heating power, and P_{sh}, P_{orbit} and P_{ripple} are the shine-through loss of injected beam, banana orbit loss and ripple loss of fast ions, respectively. The ohmic heating power, P_{ohmic}, gradually increases from 0.4 to 0.9 MW at P_{NBI} = 13.0 MW. With an increase in $\bar{n}_e$ from 2.4×10^{19} to 4.5×10^{19} m^{-3}, P_{sh} decreases from 4 to 1 % of P_{NBI}. The fractions of P_{orbit} and P_{ripple} are in the ranges of 0.5-1.4 % and 15-20 % with some scatter. Accordingly, P_{abs} ranges between 9.3 and 10.6 MW at P_{NBI} = 13.0 MW. To evaluate the confinement properties in a quasi-steady state where dW_{th}/dt is negligible, the transport analysis was done by smoothing the data in time over several ELM cycles (~ 100 ms). The relevant times of analysis (t_a) were chosen for the beam-slowing down time (τ_{sd})

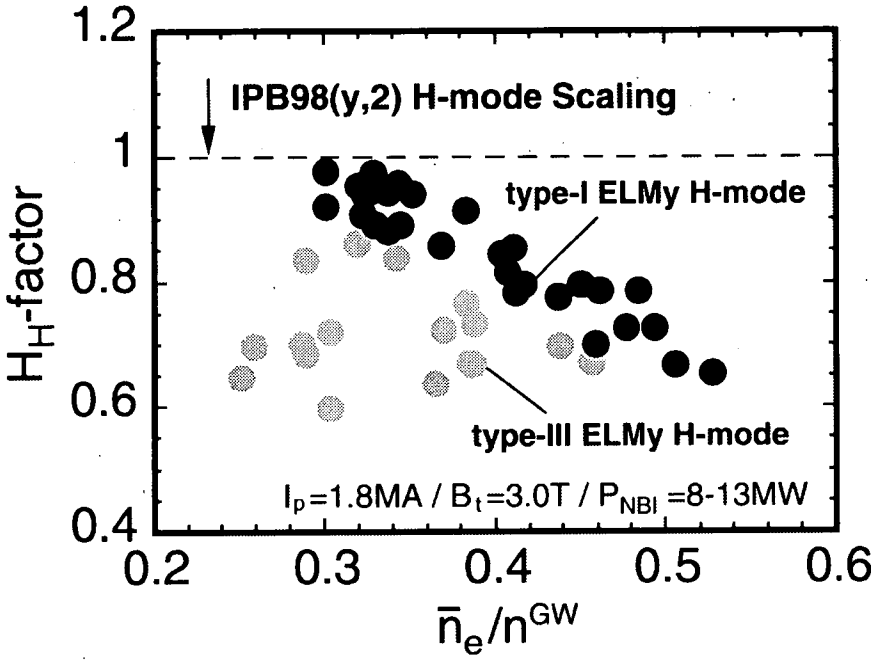

Figure 3.4 The H_H-factor during the type-I ELMy H-mode based on the IPB98(y,2) scaling, $H_H^{98(y,2)}$ (closed circles), is shown as a function of $\bar{n}_e/n^{GW}$. For the type-III ELMy H-mode, $H_H^{98(y,2)}$ is plotted as shaded circles.

after the beginning of each step of NB power (t_0), i.e. $t_a > t_0 + \tau_{sd}$. The energy confinement time of fast ions, τ_{fast}, is sufficiently larger than the slowing down time of NB injection [71,72]. The thermal energy confinement time, τ_{th}, was derived from the energy balance equation for a thermal plasma given as:

$$\frac{dW_{th}}{dt} = P_{abs} - \frac{W_{th}}{\tau_{th}} \tag{3.5}$$

$$W_{th} = \frac{3}{2} k_B \int_{V_p} \sum_j n_j(r) T_j(r) dV_p \tag{3.6}$$

where j denotes species of particles, i.e. electron, deuterium and carbon, and k_B is Boltzmann's constant.

Figure 3.4 shows the H_H-factor of ELMy H-mode plasmas with P_{NBI} = 8-13 MW as a function of $\bar{n}_e/n^{GW}$. The H_H-factor, $H_H^{98(y,2)}$, defined as the thermal

energy confinement time, τ_{th}, normalized to $\tau_{th}^{IPB98(y,2)}$, decreases continuously from 1.0 to 0.6 with increasing $\bar{n}_e / n^{GW}$ from 0.30 to 0.53.

Figure 3.5(a) indicates the density dependence of W_{fast}, W_{th} and W_{dia} with P_{NBI} = 13.0 MW. As $\bar{n}_e$ increases from 2.7×10^{19} to 4.5×10^{19} m^{-3}, W_{dia} and W_{fast} decrease from 3.5 to 2.5 MJ and from 0.9 to 0.3 MJ, respectively. Since W_{fast} is proportional to the energy slowing down time of the fast ions ($\propto T_e^{1.5}/n_e$), it decreases with $\bar{n}_e$. On the other hand, W_{th} remains almost constant in the range of 2.0-2.4 MJ. The stored energy of thermal ions is 41-49 % of W_{th} at all the densities. The above results refer to ELMy H-modes with type-I ELMs for the entire range of densities obtained in the experiments.

Figure 3.5(c) shows the density dependence of τ_{th} and τ_E at P_{NBI} = 13.0 MW, where P_{abs} is in the range of 9.3-10.6 MW (see figure 3.5(b)). As the density is raised, τ_E decreases continuously from 0.38 to 0.24 s, while τ_{th} undergoes a slight reduction or is almost constant in the range of 0.19-0.25 s. It should be emphasized that the reduction in $H_H^{98(y,2)}$ with density shown in figure 3 is caused by the positive density dependence of the predicted thermal energy confinement time, $\tau_{th}^{IPB98(y,2)}(\propto n_e^{0.41})$ because τ_{th} given by the experiments remains almost constant or decreases slightly with density as shown in figure 3.5(c). Attention must be drawn to the saturation of τ_{th} with density at high density.

The profiles of n_e, T_e and T_i for the low and high density ELMy H-mode discharges with P_{NBI} = 13.0 MW are shown in figures 3.6(a) and (b). It can be seen that the central value of T_i goes down to that of T_e with increasing $\bar{n}_e$. There are mainly two reasons for this result. One is that the energy deposition of the fast ions becomes broader and its spatial peak shifts towards the edge. The other is due to the equipartition power from ions to electrons in the density range where the ion heating fraction is predominant. A noteworthy feature, seen in our data, is that the total thermal stored energy, derived from the volume-integration of the total thermal pressure profile, remains constant over a wide range of densities as shown

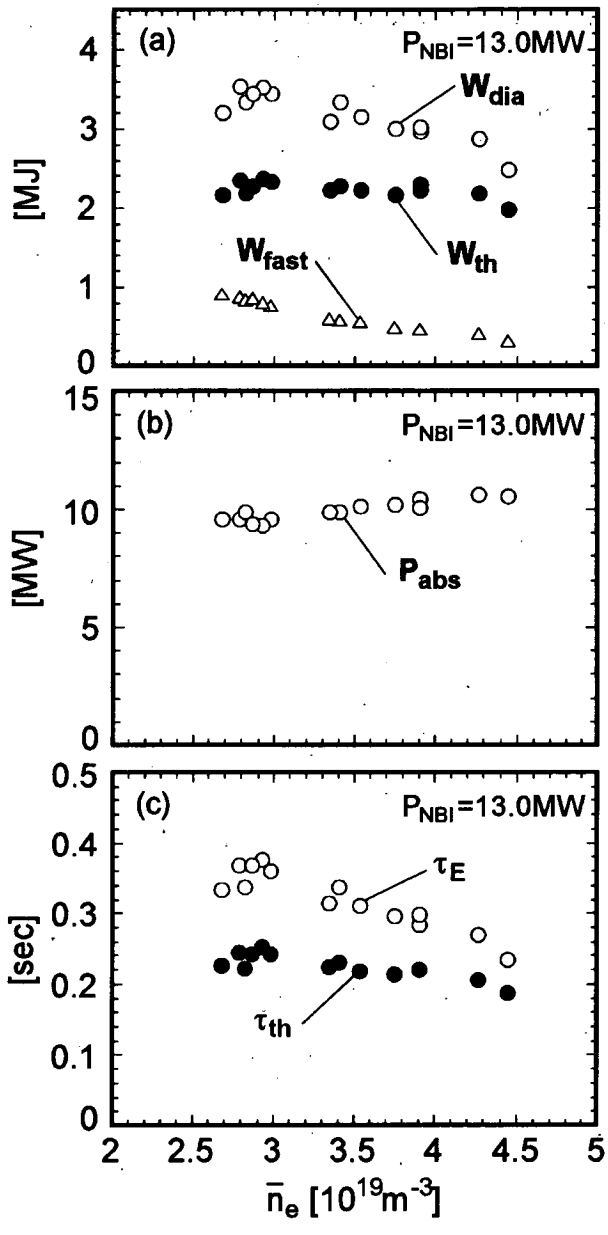

Figure 3.5 (a) The density dependence of the stored energy is shown for the type-I ELMy regime at P_{abs} = 13.0 MW. Open circles, closed circles and open triangles indicate the global stored energy (W_{dia}), the energy stored in the thermal plasma (W_{th}) and in the fast ions (W_{fast}), respectively. (b) The absorbed power, P_{abs} (open circles), is plotted as a function of $\bar{n}_e$. (c) The density dependence of the energy confinement time is shown for the type-I ELMy regime. Open and closed circles indicate τ_E and τ_{th}, respectively.

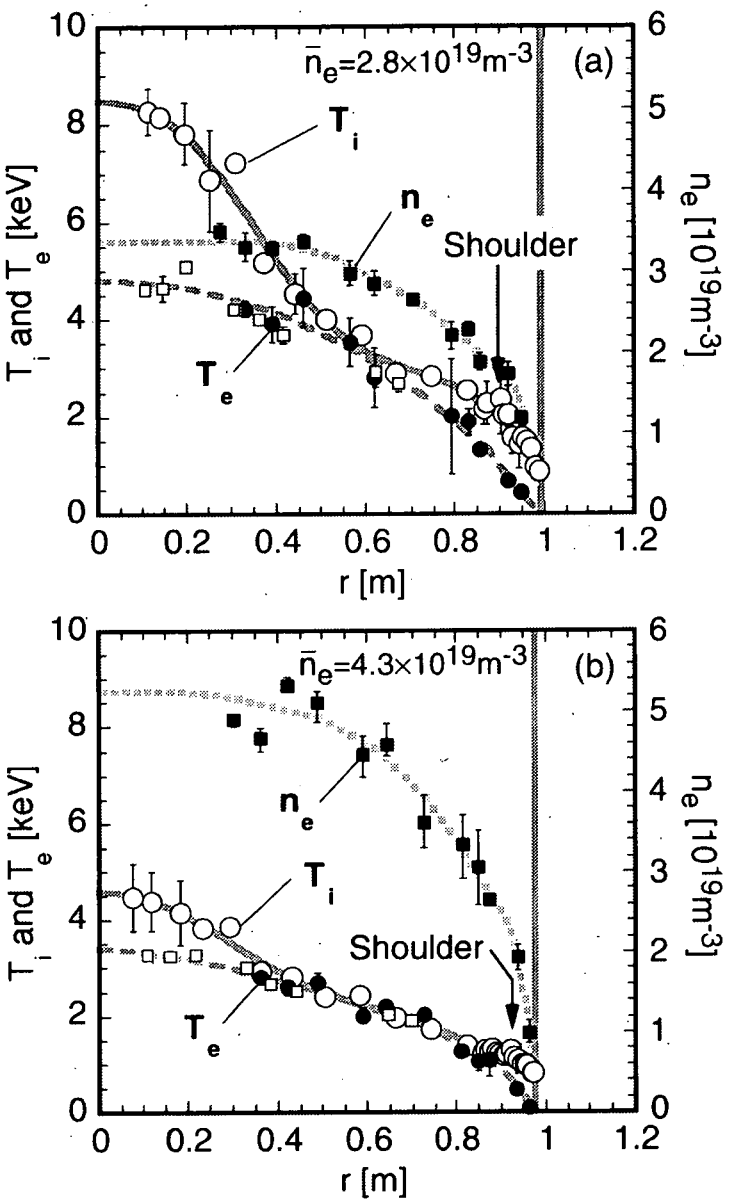

Figure 3.6 Radial profiles of T_c, T_i and n_c in ELMy H-mode plasmas (a) at low density (shot 33638; t = 8.48 s, $\bar{n}_e = 2.8\times10^{19}$ m^{-3}), and (b) at high density (shot 33642; t = 8.39 s, $\bar{n}_e = 4.3\times10^{19}$ m^{-3}). The NB injection power, P_{NBI}, is fixed at 13.0 MW. The electron density, n_c (closed squares), and the electron temperature, T_c (closed circles), are obtained by Thomson scattering measurement of YAG laser. The core region T_c profiles are obtained by ECE measurement (open squares). The ion temperature, T_i, is measured with CXRS (open circles). The separatrix position is shown by a dark column.

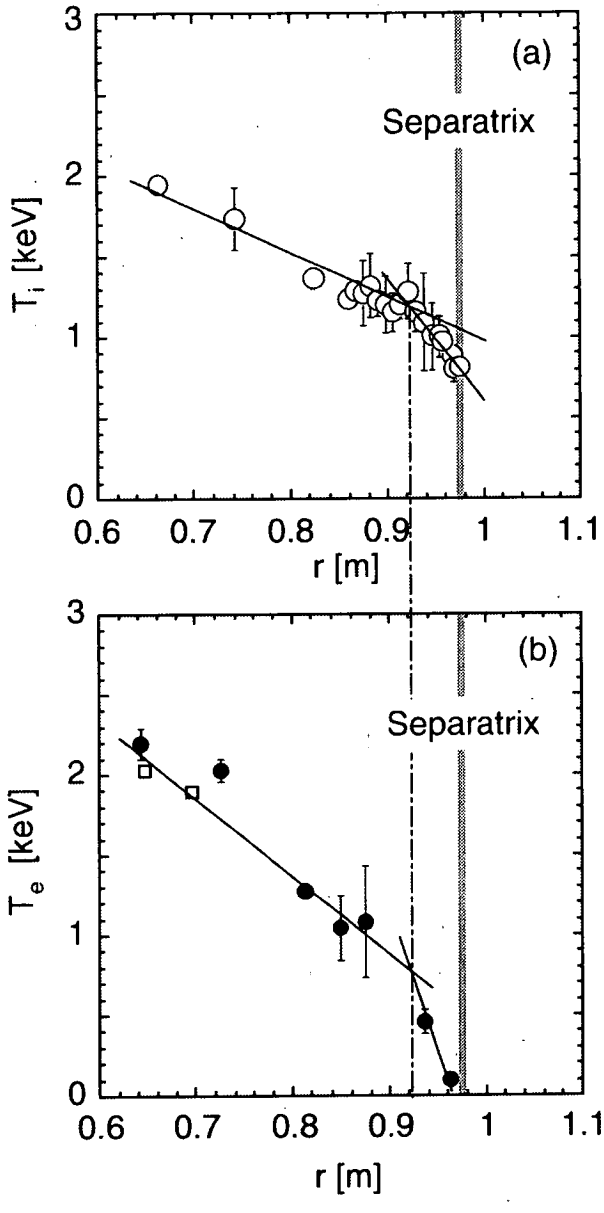

Figure 3.7 Details of the edge region are illustrated for (a) T_i and (b) T_e in a high density plasma. The shoulder of the H-mode pedestal is defined with the T_i profile.

in figure 3.5(a). The ion temperature is seen to be building up gradually at the center with a parabolic type of profile as the density is decreased. However, the thermal pressures at the center are almost constant (~ 6×10^4 Pa) in both cases. In this study, the shoulder radius of the H-mode pedestal, r_{ped}, is defined with the T_i profile as shown in figure 3.7(a). The electron temperature at the shoulder, T_e^{ped}, is determined at r_{ped} by a linear fitting from the core region as shown in figure 3.7(b), since the YAG Thomson scattering measurement has a large error especially at low density owing to the small signal to noise (S/N) ratio and its spatial resolution is not adequate to determine r_{ped} from the T_e profile itself. Figures 3.8(a) and (b) plot the electron density at the shoulder of the H-mode pedestal, n_e^{ped}, and at the center, $n_e(0)$, as a function of $\bar{n}_e$. In the type-I ELMy regime, n_e^{ped} and $n_e(0)$ increase in proportion to $\bar{n}_e$. The electron and ion temperatures at the shoulder of the H-mode pedestal, T_e^{ped} and T_i^{ped}, decrease from 1.6 to 0.8 keV and from 2.8 to 1.0 keV, respectively (see figure 3.8(c)). These reductions are attributed to the limit of the pedestal pressure due to the type-I ELM activity, which is discussed in section 3.3.2. With increasing $\bar{n}_e$, the central temperature of ions, $T_i(0)$, decreases about by 5 keV, while that of electrons, $T_e(0)$, decreases about by 3 keV as shown in figure 3.8(d).

The density dependence of the thermal stored energy in the pedestal, W_{th}^{ped}, and in the core, W_{th}^{core}, is shown in figure 3.9(a), where W_{th}^{ped} and W_{th}^{core} are calculated as:

$$W_{th}^{ped} = \frac{3}{2}k_B \int_{V_p} \sum_j n_j^{ped} T_j^{ped} dV_p \approx \frac{3}{2}\sum_j n_j^{ped} k_B T_j^{ped} \cdot 2\pi R_p \cdot \pi a_p^2 \kappa \quad (3.7)$$

$$W_{th}^{core} = W_{th} - W_{th}^{ped} \quad (3.8)$$

With an increase in $\bar{n}_e$ from 2.9×10^{19} to 4.5×10^{19} m^{-3} at P_{NBI} = 13.0 MW, W_{th}^{ped} and W_{th}^{core} remain in the ranges of 0.8-0.9 MJ and of 1.2-1.5 MJ, respectively.

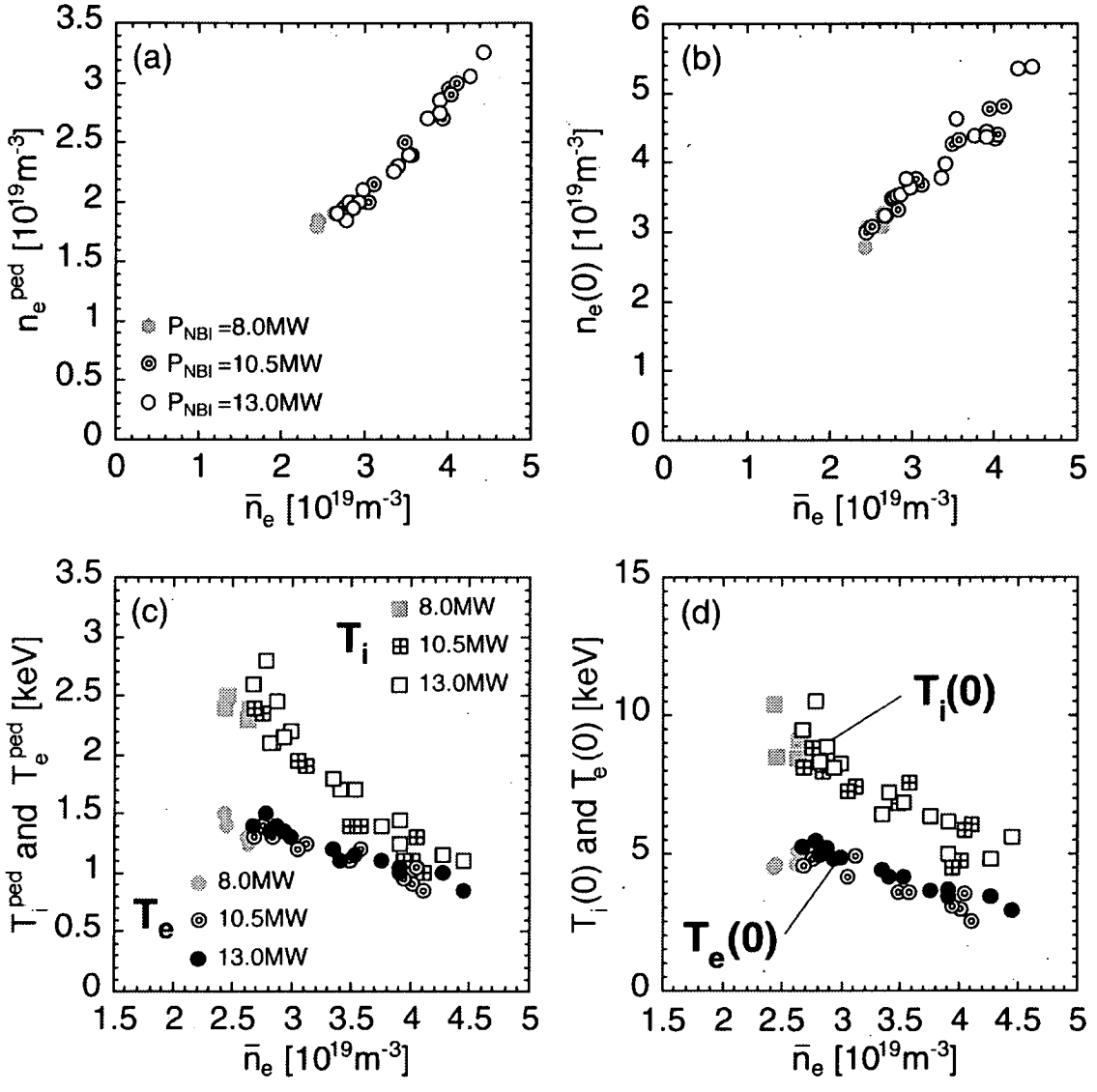

Figure 3.8 The density dependences of (a) n_e^{ped} and (b) $n_e(0)$ are plotted for type-I ELMy H-mode plasmas. Symbols are distinguished for the NB injection power. (c) Pedestal and (d) central values of T_i and T_e are plotted as a function of $\bar{n}_e$. Squares and circles indicate T_i and T_e, respectively.

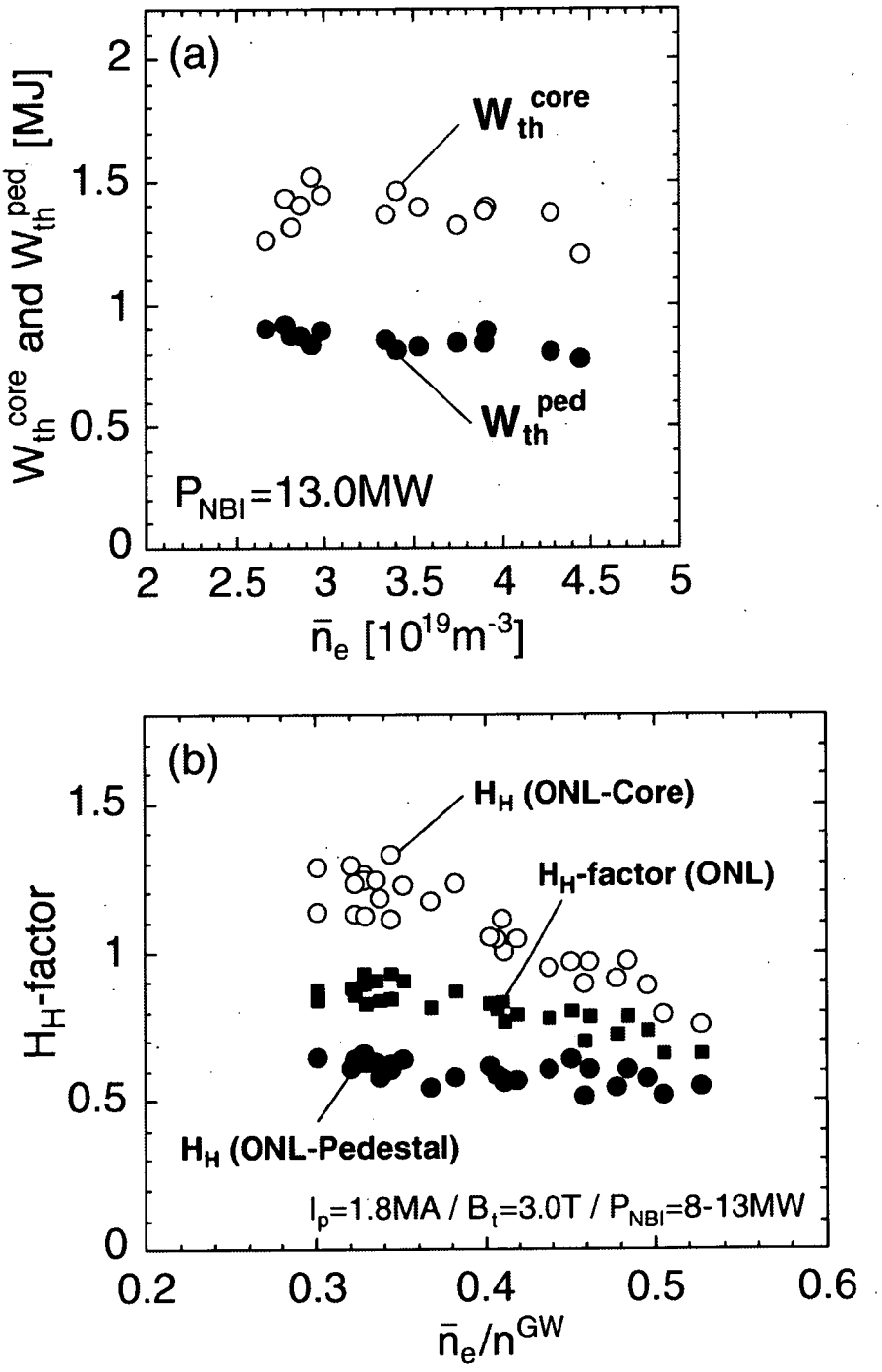

Figure 3.9 (a) Density dependences of W_{th}^{core} (open circles) and W_{th}^{ped} (closed circles) at P_{NBI} = 13.0 MW. (b) The enhancement factor during the type-I ELMy H-mode based on the offset non-linear scaling, H_H (ONL), is plotted as closed squares. Open and closed circles indicate the enhancement factors of the core, H_H (ONL-Core), and of the pedestal confinement, H_H (ONL-Pedestal), respectively.

Figure 3.9(b) shows the enhancement factors of the core and pedestal confinement, H_H (ONL-Core) and H_H (ONL-Pedestal), based on the offset non-linear scaling. It is observed that H_H (ONL-Pedestal) remains almost constant in the range of 0.5-0.7 over the density range of 30-53 % of n^{GW}, while H_H (ONL-Core) decreases significantly from 1.3 to 0.8 with density. Here it is noted that H_H (ONL-Pedestal) is rather small in these discharges. This result is observed in low triangularity discharges (δ = 0.16-0.19), where the edge pressure gradient becomes small. This is discussed further in section 3.3.4. Besides, it may be worth pointing out, in passing, that the ITER H-mode confinement database predicts H_H (ONL-Pedestal) ~ 0.75 for JT-60U ELMy H-mode plasmas. In this estimation, the pedestal component of the offset non-linear scaling is statistically determined as the offset part of W_{th}, independent of the heating power, P_{abs} [70].

3.3.2. Pedestal structure during ELMy H-mode

In the high density discharge shown in figure 3.2, it was observed that the L-H transition occurred at t = 6.6 s and the energy confinement was improved afterwards. After a quiescent phase for 0.2 s, type-III ELMs appeared at t = 6.8 s. In the type-III ELMy H-mode phase, W_{dia} gradually increased with the heating power. In this discharge, a temporarily improved performance was observed with the appearance of the ELM-free phase at t = 7.6 s and then W_{dia} was saturated after the appearance of type-I ELMs at t = 7.75 s. The saturated value of W_{dia} due to type-I ELMs in the low density discharge is higher than in the high density discharge. This is because the lower density plasma retains a higher W_{fast} as described in section 3.3.1., e.g. W_{fast} ~ 0.5 MJ at high density and ~ 0.9 MJ at low density, where W_{th} ~ 2.4 MJ at P_{NBI} = 13.0 MW.

The ELM-free period becomes longer at even lower densities. Figure 3.10(a) indicates the waveform of a low density discharge with $\bar{n}_e$ = (1.3-2.7)×

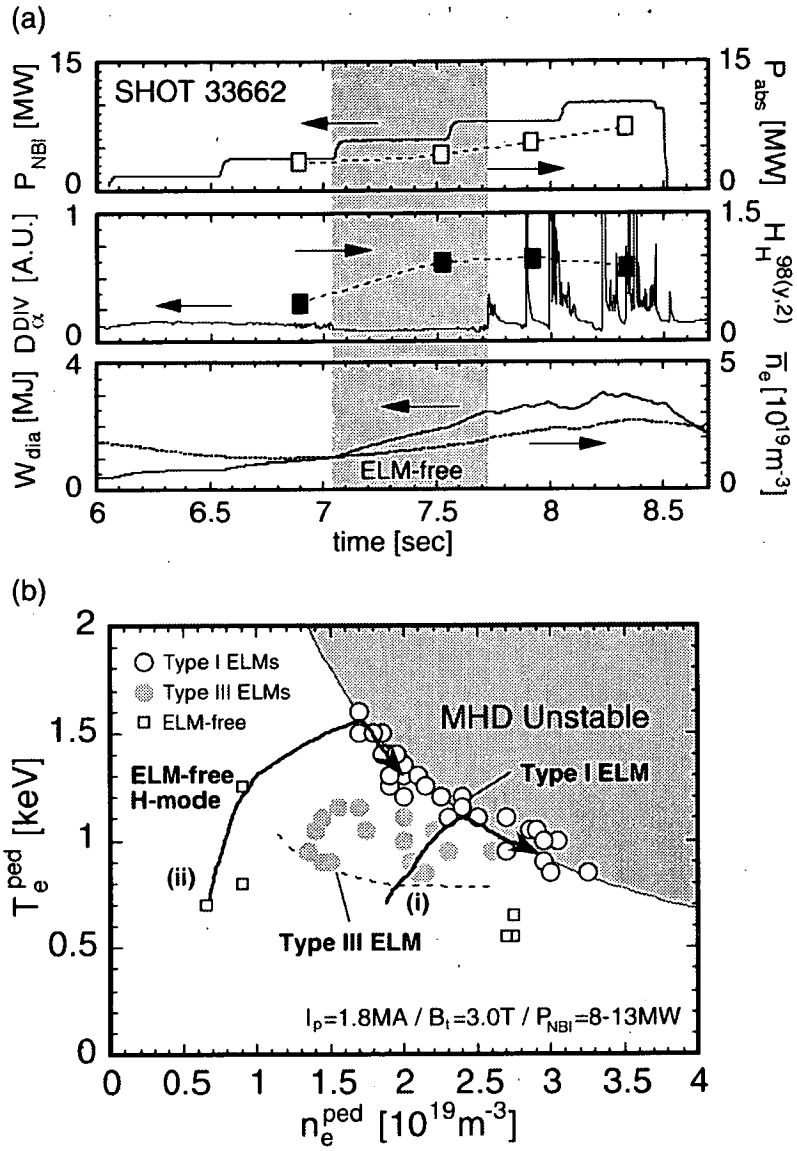

Figure 3.10 (a) Time evolution of plasma parameters in the low density ELMy H-mode discharge without the type-III ELMy phase. The ELM-free phase is indicated by the shaded area. (b) Diagram of $n_e^{ped} - T_e^{ped}$ for classifying ELM behavior in JT-60U. Open and shaded circles indicate the type-I and type-III ELMy H-mode plasmas at P_{NBI} = 8-13 MW, respectively. Open squares indicate the ELM-free H-mode plasmas. The arrows (i) and (ii) indicate the time evolutions of the pedestal shoulder in high and low density plasmas (shots 33662 and 33655), respectively.

10^{19} m^{-3}, where the ELM-free phase continues from the L-H transition until the first ELM burst occurs at t = 7.7 s. In this discharge, τ_E reaches 0.62 s at t = 7.52 s. The classification of ELM behavior in $n_e^{ped}-T_e^{ped}$ space is shown in figure 3.10(b). The arrow (i) indicates the high density discharge shown in figure 3.2. Both n_e^{ped} and T_e^{ped} increase through the type-III ELM region with additional heating power after the L-H transition, and then type-I ELMs appear when T_e^{ped} increases further with high power heating. In the type-I ELMy H-mode phase, increases in n_e^{ped} accompany decreases in T_e^{ped} so that the thermal energy stored in the pedestal is kept constant. The arrow (ii) indicates the low density discharge without the type-III ELMy H-mode phase shown in figure 3.10(a). Since the L-H transition occurs at quite a low density, the ELM-free phase is sustained and the type-III ELM region is completely avoided.

The next point is the saturation of the edge pedestal pressure caused by the type-I ELM activities. The ELM events involve very rapid expulsion of energy and particles from the region of the H-mode transport barrier out into the scrape-off layer (SOL), and thereby transiently reduce the temperature and density at the pedestal shoulder. The energy loss produced by type-I ELM bursts, which can enhance erosion of the divertor targets to the point where component lifetime becomes unacceptably short, is also a significant concern. Type-I ELMs exhibit a repetition frequency, f_{ELM}, that increases with the absorbed power, P_{abs} [73], and the density, while type-III ELMs have a repetition frequency that decreases with the absorbed power as shown in figure 3.11(a). It is generally observed that an increase in the edge electron temperature due to high power heating stabilizes type-III ELM activities [74]. During the type-I ELMy H-mode phase f_{ELM} tends to increase gradually when the plasma density is raised at P_{NBI} = 13.0 MW (see figure 3.11(b)). Each burst of ELM events expels the energy from the region near the plasma boundary. The energy stored outside the pedestal shoulder, W_{edge}, is evaluated according to the definition shown in figure 3.12. It has to be noted here

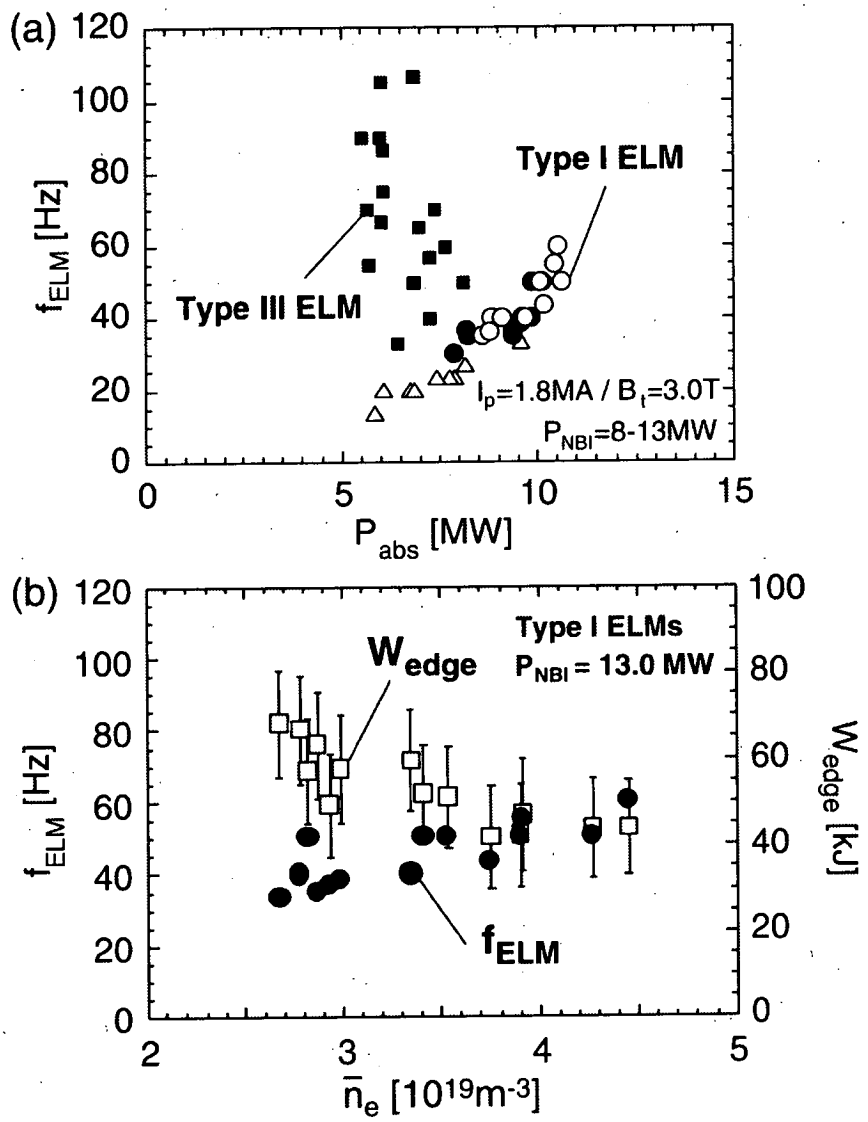

Figure 3.11 (a) Dependence of ELM frequency, f_{ELM}, on P_{abs} in the ELMy H-mode discharges. The data groups with f_{ELM} increasing linearly with P_{abs} correspond to type-I ELMs. Open triangles, closed circles and open circles indicate the density regions of $\bar{n}_e = (2.4\text{-}2.7)\times 10^{19}$ m^{-3}, $(2.8\text{-}3.5)\times 10^{19}$ m^{-3} and $(3.6\text{-}4.5)\times 10^{19}$ m^{-3}, respectively. The other group with high f_{ELM} at low power corresponds to type-III ELMs (closed squares). (b) The average ELM frequency, f_{ELM} (closed circles), and the energy stored outside the pedestal shoulder, W_{edge} (open squares), are plotted as a function of $\bar{n}_e$ at P_{NBI} = 13.0 MW in the type-I ELMy regime.

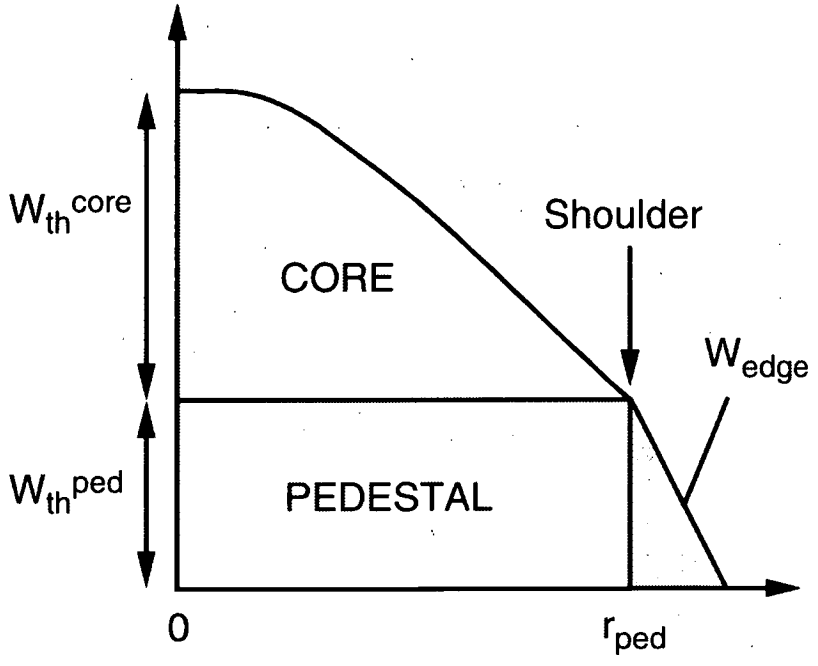

Figure 3.12 Schematic representation of the thermal energy stored in the pedestal plasma, W_{th}^{ped}, and outside the pedestal shoulder, W_{edge}. The core component of thermal stored energy, W_{th}^{core}, is also shown.

that W_{edge} itself could not be the energy loss produced by each burst of ELMs, ΔW_{ELM}. The energy stored outside the pedestal shoulder, W_{edge}, is given as:

$$W_{edge} = \frac{3}{2} k_B \int_{V_{ped}} \sum_j n_j(r) T_j(r) \mathrm{d}V_p \approx 3\pi^2 R_p r_{ped} \cdot p_{ped} \Delta r \qquad (3.9)$$

where V_{ped}, p_{ped} and Δr denote the plasma volume outside the shoulder of the H-mode pedestal, the pedestal pressure and the spatial width of the edge pedestal, respectively. The pedestal width, Δr, is defined as the radial distance between the separatrix radius, r_{sep}, and the shoulder radius of the H-mode pedestal, r_{ped}, measured with the T_i profile. The density dependence of W_{edge} during the type-I ELMy H-mode regime at P_{NBI} = 13.0 MW is shown in figure 3.11(b). It can be seen that W_{edge} becomes smaller when the density is increased whereas f_{ELM} becomes larger. The product of f_{ELM} and W_{edge} ranges between 15 and 30 % of P_{abs} with some scatter. Additional comments on the relationship between ΔW_{ELM} and

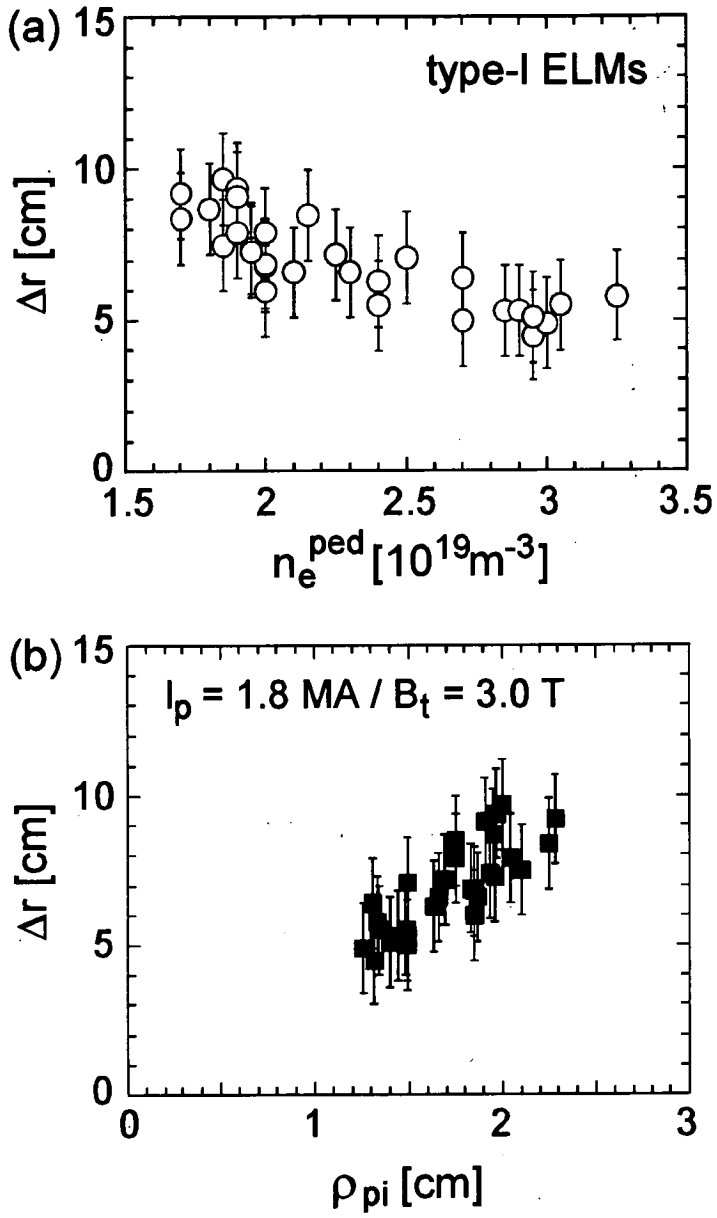

Figure 3.13 (a) Dependence of the pedestal width, Δr, on n_e^{ped} during the type-I ELMy H-mode. (b) Relationship between the pedestal width, Δr, and the poloidal gyro-radius of thermal ions, ρ_{pi}, at fixed poloidal magnetic field.

W_{edge} are given in section 3.4. The reduction in W_{edge} with increasing density is mainly attributed to the change in Δr. The dependence of Δr upon n_e^{ped} in the type-I ELMy H-mode is shown in figure 3.13(a). The pedestal width, Δr, is seen to become narrower with increasing n_e^{ped}. In JT-60U, it has been reported that Δr is approximately proportional to the poloidal gyro-radius of thermal ions, ρ_{pi} ($\propto T_i^{1/2}/B_p$) [75]. A similar relationship between Δr and ρ_{pi} was obtained at a fixed poloidal magnetic field, B_p, of 0.36 T at the plasma boundary in this series of experiments (see figure 3.13(b)).

3.3.3. Correlation between the core and edge pedestal confinement

It is observed that the edge pedestal structure imposed by the destabilization of ELMs has a large influence on the thermal energy confinement of the core plasma. In particular, since the pedestal density and temperature vary inversely in the type-I ELMy H-mode regime as shown in figure 3.10(b), the saturation of thermal energy confinement, or the reduction in the H_H-factor, can be linked to the relatively low pedestal temperatures.

A strong correlation between T_i^{ped} and H_H (ONL-Core) is found for type-I ELMy H-mode plasmas as shown in figure 3.14. Since the thermal energy confinement of the pedestal plasma is almost independent of the density as expected from the offset non-linear scaling (see figure 3.9(b)), the variation of H_H (ONL-Pedestal) with T_i^{ped} is also small. With an increase in T_i^{ped} from 1.0 to 2.2 keV, H_H (ONL-Core) continuously increases from 0.8 to 1.3. However, it can be seen that once a certain pedestal temperature is exceeded ($T_i^{ped} \geq 2.2$ keV) the impact of the pedestal temperature on the core energy confinement weakens, i.e. H_H (ONL-Core) remains constant in the range of 1.1-1.3. The influence of the

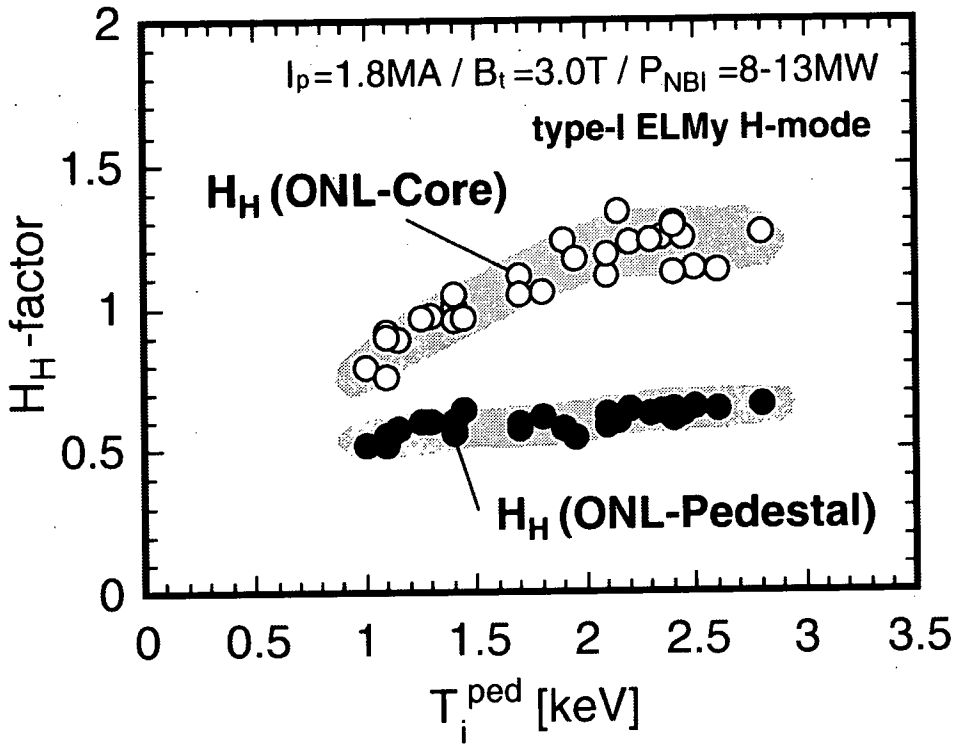

Figure 3.14 Influence of the pedestal temperature on the core and pedestal energy confinement in the type-I ELMy H-mode plasmas. Open and closed circles indicate H_H (ONL-Core) and H_H (ONL-Pedestal), respectively.

pedestal structure on the thermal energy transport of the core plasma is evaluated by using the effective heat diffusivity of the core component, χ_{eff}^{core}, given as:

$$\chi_{eff}^{core} \equiv \frac{\int_0^{r_{ped}} \chi_{eff}(r) \cdot 2\pi r dr}{\int_0^{r_{ped}} 2\pi r dr} \tag{3.10}$$

where $\chi_{eff}(r)$ is calculated with the transport analysis code for thermal plasmas (TOPICS) [67]. The heat diffusivity derived from Eq. (3.10) indicates a characteristic value which can determine the energy transport of the core plasma. The variation in χ_{eff}^{core} is small or roughly constant over the range of T_i^{ped} with some scatter as shown in figure 3.15(a). It can be also seen for each species that the temperature profiles are approximately self-similar and differ only by a

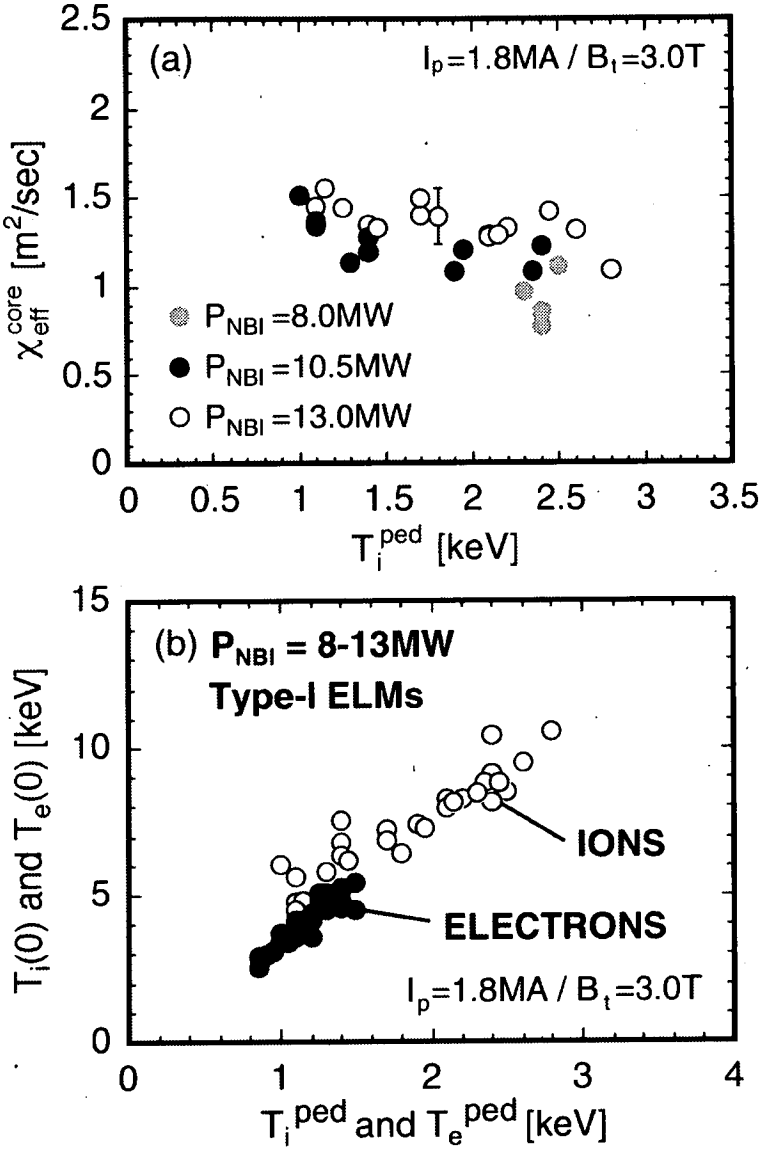

Figure 3.15 (a) Dependence of the effective heat diffusivity of the core plasma, χ_{eff}^{core}, on T_i^{ped} in the type-I ELMy H-mode plasmas. (b) Profile similarity during the type-I ELMy H-mode plasmas: the central temperatures for each species, $T_i(0)$ (open circles) and $T_e(0)$ (closed circles), are proportional to the temperatures at the shoulder of the H-mode pedestal.

constant factor throughout a wide range of heating powers (P_{NBI} = 8-13 MW) in the type-I ELMy H-mode plasmas (see figure 3.15(b)). The most significant result from this edge-core relationship for the temperature profiles is the fact that the trend of χ_{eff}^{core} at high density seen in figure 3.15(a) is incompatible with the positive temperature dependence of χ_{eff}^{core} expected from Bohm or gyro-Bohm diffusion, i.e. $\chi_{Bohm} \propto T$ or $\chi_{gyro\text{-}Bohm} \propto T^{1.5}$.

In the H-mode discharges, where the pedestal pressure is limited by the type-I ELMs, an increase in the pedestal density due to gas puffing reduces the temperature at the pedestal shoulder, and if the pedestal temperature becomes lower than a certain level, the energy confinement enhancement factor of the plasma core, H_H (ONL-Core), starts to decrease. Similar agreement is obtained from the estimate $\chi_{eff}^{core} \propto a_p^2/\tau_{th}$ since τ_{th} is kept almost constant over the range of densities analyzed. As the density is raised, saturation of the core energy confinement, or reduction in H_H (ONL-Core), is also observed. Thus, H_H (ONL-Core) is expected to decrease with a reduction in the pedestal temperature owing to an increase in the density. The edge temperature plays a significant role as the boundary condition in determining the thermal energy confinement of the core plasma.

3.4. Discussions

Consideration should be given to the question of whether the saturation of the thermal energy confinement of the core plasma is caused directly by ELM bursts or by an underlying mechanism of thermal energy transport connecting the edge pedestal with the core plasma. As shown in figures 3.11(a) and (b), the ELM frequency, f_{ELM}, is seen to increase with the absorbed power and also to increase with density at a fixed P_{NBI}. Moreover, the energy stored outside the shoulder of the H-mode pedestal, W_{edge}, tends to decrease gradually with density. When f_{ELM}

increases with density at a constant power flow crossing the separatrix, the energy loss expelled by each burst of ELMs, ΔW_{ELM}, would be expected to decrease with density. The trend in W_{edge} with density seems consistent with that expected for ΔW_{ELM} as can be seen in figure 3.11(b), although ΔW_{ELM} has not been estimated quantitatively. The region of the plasma affected by an ELM burst is reported to be larger than the pedestal width, and ΔW_{ELM} continually decreases with density in DIII-D [76]. In this case, the direct heat loss during a short turbulent phase due to ELM events cannot account directly for the thermal energy saturation of the core plasma.

It might then be argued that ELMs could be phenomena not located exclusively near the plasma boundary but rather that there is a large transport structure connected with the plasma core. As for the saturation of the core energy confinement, the effect of the edge pedestal structure imposed by the ELM activities in situations of stiff profiles in the plasma core could be more significant than the direct heat and particle loss due to each ELM event. The enhancement of the energy confinement (the H-factor) during H-mode in many cases depends strongly on the temperature at the shoulder of the H-mode pedestal [54,58-60]. In particular, it can be seen in figure 3.15(b) that the pedestal and central temperatures for each species are approximately proportional for the entire range of densities covered. Besides, similarity of the density profiles is also observed as shown in figures 3.8(a) and (b). When the pedestal density is increased, the saturation of W_{th}^{ped} during the type-I ELMy H-mode regime forces a reduction in the pedestal temperature (see figure 3.10(b)). The core temperature, in turn, decreases only by an approximately constant factor with a reduction in the temperature at the boundary. It follows from these results that the thermal stored energy, W_{th}, remains almost constant as shown in figure 3.5(a). These observations naturally suggest that, if a higher sustainable W_{th}^{ped} is produced in type-I ELMy H-mode discharges, the pedestal temperature is expected to be higher at a given

density and a higher energy confinement enhancement factor would be obtained. High triangularity discharges have been observed to lead to a higher edge pedestal pressure and to improvement of the energy confinement in many devices [26-28,30]. These results might be indicative of supportive evidence that the edge pedestal structure could determine the core confinement because triangularity strongly affects the peripheral shape of the toroidal magnetic flux surfaces. An analysis results of the energy confinement and pedestal structure for high triangularity plasmas are treated in chapter 4.

3.5. Conclusions

The dominant causes of the reduction in the enhancement factor of thermal energy confinement with increasing plasma density have been analyzed in ELMy H-mode plasmas on JT-60U. The thermal energy stored in the pedestal, W_{th}^{ped}, remains almost constant over a wide range of densities in the type-I ELMy H-mode regime. The core component, W_{th}^{core}, also tends to remain constant although the offset non-linear (ONL) scaling, which is developed in the ITER H-mode confinement database, predicts that W_{th}^{core} should increase with density. As the density is increased, the temperature at the pedestal shoulder drops so that the pedestal pressure remains almost constant during the type-I ELMy H-mode regime. The temperature profile for each species is approximately self-similar and thus the core temperature varies in proportion to the pedestal temperature. The reduction in the pedestal temperature at high density leads to saturation of the thermal energy stored in the core plasma.

4. Thermal Energy Confinement of High Triangularity ELMy H-mode Plasmas

4.1. Introduction

ELMy H-modes are currently considered as the most promising plasma operating regime of enhanced confinement, with a proven capability for steady state performance in a future reactor-size magnetic fusion experiment. As is presented in chapter 2, the existing ITER design also requires ELMy H-mode operation combined with a high energy confinement time [11,48,50,51,77]. The H-mode plasma conditions at the plasma edge strongly influence the conditions and limits for plasma operation, including the energy confinement regime, and provide boundary conditions for energy and particle transport in the core plasma [27,54,58,59,78,79]. Most of the confinement properties in these plasmas indicate that temperature profiles generally show stiffness, i.e., are limited by a critical temperature gradient scale length [60,80,81]. High triangularity discharges with higher critical edge pressure gradient are therefore expected to lead to further improved energy confinement of the plasma core [26-31]. The improved energy confinement has also been achieved in high β_{pol} H-mode discharges with internal transport barrier (ITB) at high triangularity [73,82]. Growth of the pedestal width and higher edge pedestal pressure is observed in these plasmas [75].

In this chapter, thermal energy confinement properties and pedestal characteristics of high triangularity ELMy H-mode plasmas are analyzed carefully for the case of JT-60U tokamak. A significant research issue is to confirm the correlation between edge and core temperatures consistently in H-mode plasmas at

different triangularity, which is seen in a variety of densities at fixed plasma shape. The influence of density and plasma shape on the temperature profile, the comparison of pedestal characteristics between low and high triangularity ELMy H-mode plasmas and the edge-core relationship of temperature profiles, are presented in this chapter. The experimental procedure for high triangularity discharges is presented in section 4.2. Thermal energy confinement properties and H-mode pedestal characteristics are analyzed in section 4.3 and section 4.4, respectively. The pedestal structure in high β_{pol} H-mode plasma with ITB is also treated in section 4.4. The boundary condition for thermal energy confinement is examined in section 4.5. The relationship between the edge pedestal and core temperatures in ELMy H-mode plasmas is discussed at low and high triangularity. Thermal energy confinement properties of high β_{pol} H-mode plasmas are presented in section 4.6. Finally, the conclusions are given in section 4.7.

4.2. Experiment of high triangularity ELMy H-mode

A typical waveform of high triangularity ELMy H-mode discharge in JT-60U is shown in figure 4.1. The experiments were performed at the plasma current, I_p = 1.0 MA, where the Greenwald density limit, n^{GW} [25], corresponds to (4.6-4.9)$\times 10^{19}$ m^{-3}. The toroidal magnetic field, B_t, is 2.1 T and the safety factor calculated at the magnetic surface corresponding to 95 % of the flux, q_{95}, is 3.4-3.6. The neutral beam (NB) injection power, P_{NBI}, for deuterium plasma was ~ 9.0 MW at the relevant time of analysis. With deuterium gas puffing, the line-averaged electron density measured with the far infrared (FIR) interferometer, $\bar{n}_e$ [61], was varied on a shot by shot basis from 1.8×10^{19} to 3.2×10^{19} m^{-3}. The maximum $\bar{n}_e$ investigated in these experiments was ~ $0.7\times n^{GW}$, at which the H-mode edge was sustained with higher frequent ELMs. The plasma configuration and viewing chords of the main diagnostics are illustrated in figure 4.2(a). The

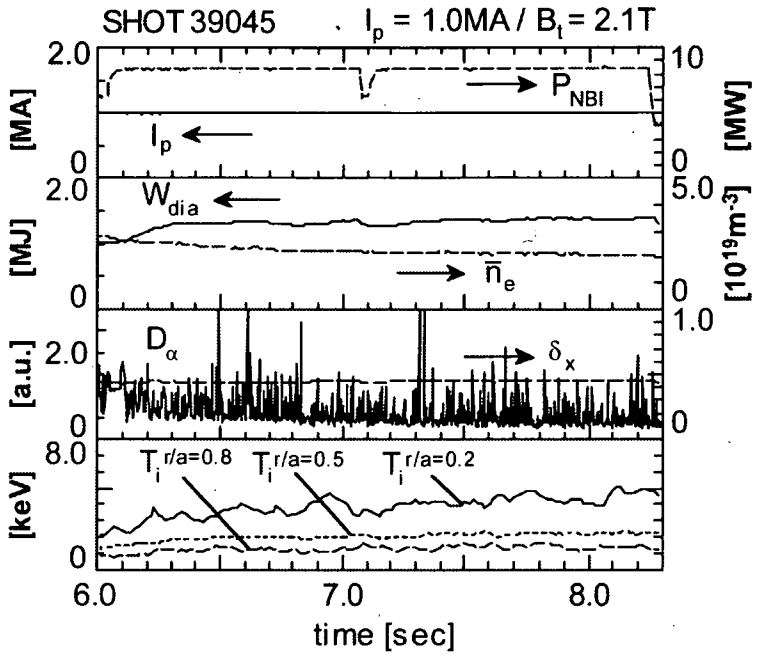

Figure 4.1 Time evolution of plasma parameters in an ELMy H-mode discharge. In the figure I_p denotes the plasma current; P_{NBI} the neutral beam injection power; $\bar{n}_e$ line-averaged electron density measured with the far-infrared (FIR) interferometer; W_{dia} the global stored energy measured with a diamagnetic loop. Intensity of D_α line emission signals from the divertor plasma and triangularity at the separatrix are given as D_α and δ_x, respectively. Time evolution of ion temperatures measured with charge-exchange recombination spectroscopy, T_i, at r/a = 0.2, 0.5 and 0.8 is also shown.

elongation, κ, of 1.4 and the triangularity, δ_x, of 0.45 were fixed. The plasma volume, V_p, was in the range of 55-56 m^3. The plasma major radius, R_p, and the minor radius, a_p, were in the ranges of 3.32-3.33 m and of 0.80-0.82 m, respectively. In order to assess the effects of triangularity on the energy confinement properties and edge pedestal parameters, low triangularity experiments were also carried out at $\delta_x \sim 0.20$ for reference (see figure 4.2(b)). The experiments aimed at achieving quasi-steady state conditions accompanied by ELM activity, so that each value of triangularity was investigated in different density scans. The operating parameters, such as I_p and B_t, were fixed with a series

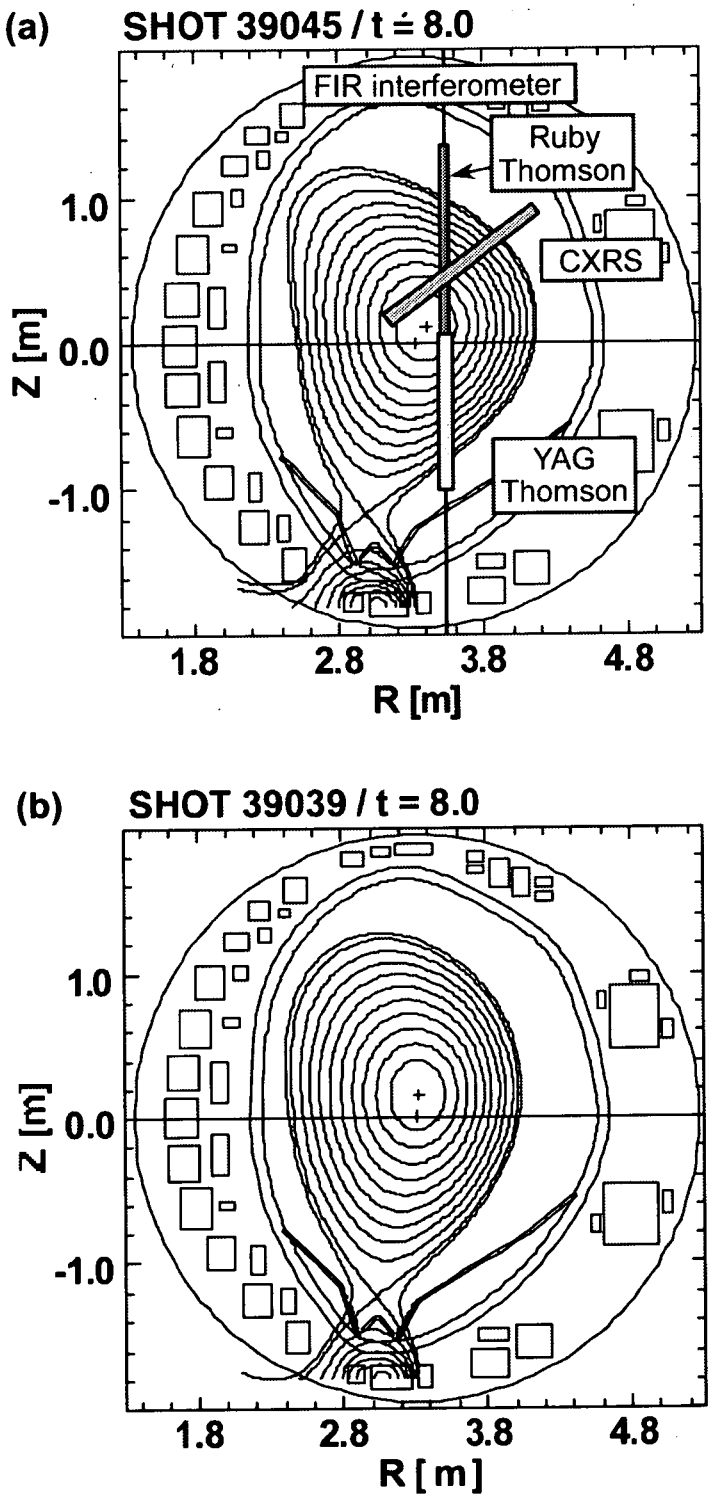

Figure 4.2 Cross sections of the plasma equilibrium in (a) high (δ_x = 0.45) and (b) low triangularity plasmas (δ_x = 0.20). Sightlines and location of main diagnostics are illustrated on a cross section of the high triangularity plasma equilibrium.

of high triangularity experiments. In this case, q_{95} and κ are in the range of 3.6-3.7 and of 1.5-1.6, respectively. Because of a slight reduction of a_p (= 0.78-0.80 m), n^{GW} becomes (4.9-5.2)×10^{19} m^{-3}.

Radial profiles of the electron density, n_e, and electron temperature, T_e, were obtained by the Thomson scattering measurement of Ruby [83] and YAG [62] laser systems. Ion temperature profiles, T_i, were measured by charge-exchange recombination spectroscopy (CXRS) of carbon [64]. The effective charge number, Z_{eff}, was estimated using visible Bremsstrahlung and its profile was assumed to be spatially uniform so that these values were capable of reproducing the measured neutron emission rate, S_n [65]. The orbit following Monte Carlo (OFMC) code [66] and the tokamak predictive and interpretation code system (TOPICS) [67] were used for the transport analysis of the fast ions and thermal plasma.

4.3. Thermal energy confinement properties

Figure 4.3 displays the H_H-factor based on the predictions of the IPB98(y,2) H-mode scaling [21] as a function of the line-averaged electron density, $\bar{n}_e$, normalized to n^{GW}. For reference, figure 4.3 also includes data from the density scan experiments of the low triangularity ELMy H-mode in JT-60U (I_p = 1.8 MA, B_t = 3.0 T, q_{95} = 3.0, δ_x = 0.16 and P_{NBI} = 8-13 MW) [79]. In any plasma configuration, the H_H-factor decreases continuously as the density is raised. It is however seen most clearly that the thermal energy confinement quality is improved by high triangularity discharges at low densities. The discharges in steady state at low densities are characterized by type-I ELMs. When the density is increased, the ELM frequency becomes larger. In the medium density regime ($\bar{n}_e / n^{GW} \sim 0.5$), the type-I and type-III ELMs are mixed and thus the ELM frequency increases rapidly. In the high triangularity discharges, the cases at

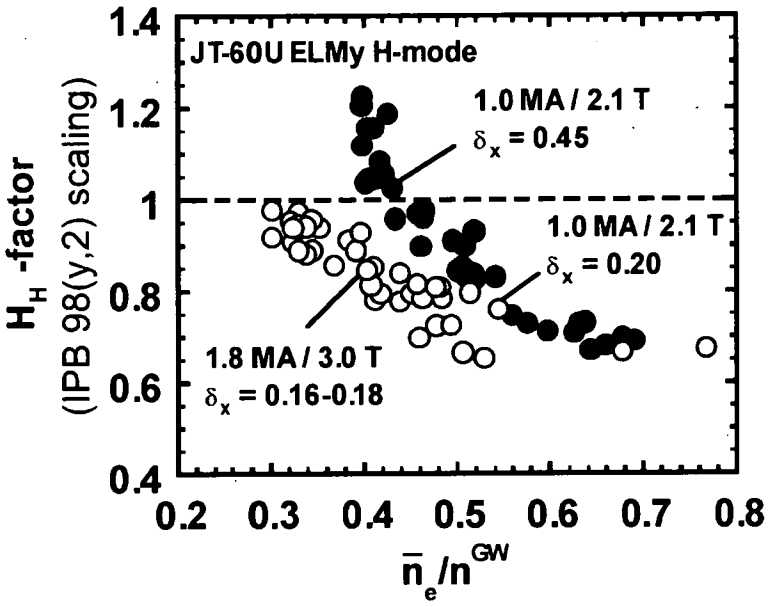

Figure 4.3 The H_H-factors in the low and high triangularity ELMy H-mode based on the IPB98(y,2) H-mode scaling, $H_H^{IPB98(y,2)}$, are shown as a function of $\bar{n}_e/n^{GW}$. Closed and shaded circles indicate the H_H-factor of δ_x = 0.45 and 0.20 at I_p/ B_t = 1.0 MA / 2.1 T, respectively. Open circles are of δ_x = 0.16-0.18 at I_p/ B_t = 1.8 MA / 3.0 T.

$\bar{n}_e/n^{GW} < 0.5$ and $\bar{n}_e/n^{GW} > 0.5$ are considered as mostly type-I and type-III ELMs, respectively. At high densities ($\bar{n}_e/n^{GW} \sim 0.7$), ELMs with much higher frequency are generated. The confinement improvement due to the high triangularity configuration becomes smaller at high densities ($\bar{n}_e/n^{GW} > 0.5$) as is seen in figure 4.3. This seems due to the low level of P_{NBI} of 9.0 MW, which would not be enough to produce the type-I ELMs at this experimental condition.

Profiles of n_e, T_e and T_i for low and high density plasmas at a fixed plasma shape of δ_x = 0.45 are shown in figure 4.4(a), (b) and (c). The enlarged pedestal T_i profiles are also shown in figure 4.4(d). A comparison of the profiles between low ($f_{GW} \sim 0.40$; where $f_{GW} \equiv \bar{n}_e/n^{GW}$) and high density plasmas ($f_{GW} \sim 0.52$) at high triangularity reveals that an increase in density leads to a reduction in the both pedestal and core temperature for each species. This observation is consistent with that obtained by low triangularity ELMy H-mode discharges in JT-

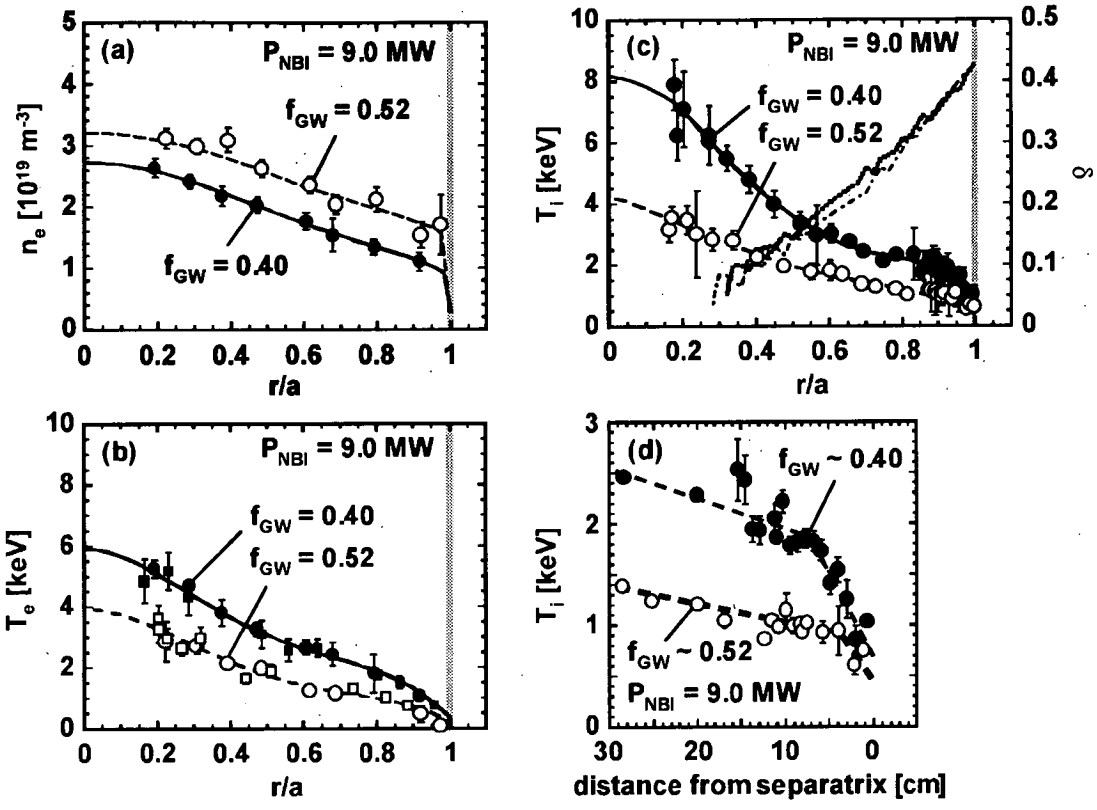

Figure 4.4 Radial profiles of (a) the electron density, (b) electron temperature and (c) ion temperature in ELMy H-mode plasmas with P_{NBI} = 9.0 MW at low (f_{GW} ~ 0.40) and high density (f_{GW} ~ 0.52). The electron density and temperature are obtained by the Thomson scattering measurement of YAG laser system. Profiles of the electron temperature obtained by the Ruby laser system are also shown as open and closed squares for f_{GW} ~ 0.52 and 0.40, respectively. The ion temperature is measured with the CXRS. Profiles of triangularity in low and high density plasmas are also shown as dotted and dotted-broken lines, respectively. The separatrix position is shown by a dark column. (d) The enlarged pedestal T_i profiles are also shown for the low and high density plasmas.

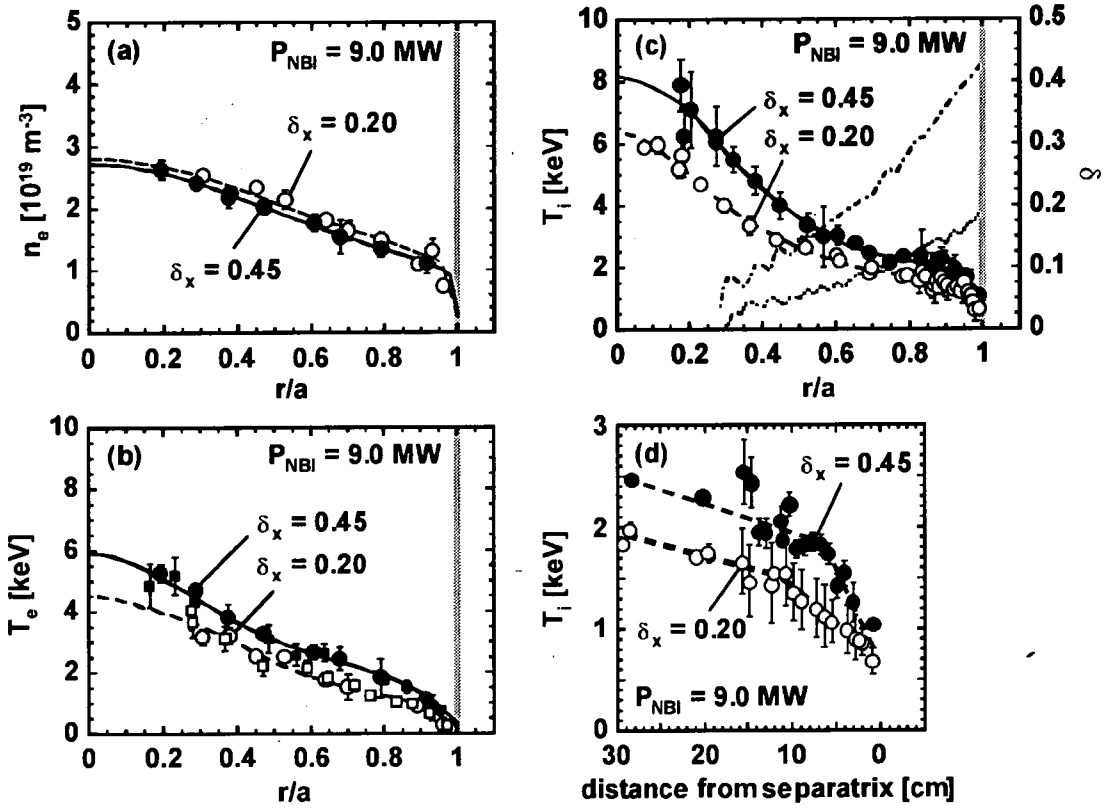

Figure 4.5 Radial profiles of (a) the electron density, (b) electron temperature and (c) ion temperature in low and high triangularity ELMy H-mode plasmas (δ_x = 0.20 and 0.45) with P_{NBI} = 9.0 MW at fixed density of f_{GW} ~ 0.40. Profiles of triangularity in low and high triangularity plasmas are also shown as dotted and dotted-broken lines, respectively. (d) Detail of the edge region in T_i profiles is also illustrated for the low and high triangularity plasmas.

60U, where the density increase is accompanied by a cooling of the central and edge pedestal temperature for each species [79]. The pedestal characteristics in high triangularity plasmas are discussed in section 4.4.

The variation of the plasma triangularity in ELMy H-mode plasmas is correlated to changes in the density and energy confinement. It is the effect of increasing triangularity in ELMy H-modes that the same H_H-factor is reached at higher densities, as shown in figure 4.3. Profiles of n_e, T_e and T_i for low and high

triangularity plasmas with P_{NBI} = 9.0 MW at a fixed density of f_{GW} ~ 0.40 are shown in figure 4.5(a), (b) and (c). It is seen in figure 6(a) that the density profiles are similar in both cases. The increase in triangularity, however, produces higher temperature for each species over the entire range of the minor radius. In fact the core temperature is also improved by a factor of ~ 1.3 as well as the peripheral temperature (see figure 4.5(d)) in the high triangularity discharge. This is of significance because the plasma shaping affects most strongly edge toroidal magnetic flux surfaces as seen in figure 4.5(c). The pressure gradient is highest in the H-mode barrier region, and strongly shape-sensitive modes, such as ballooning or interchange modes, are destabilized only in the edge. Thus, there seems to exist a large transport structure under which the core temperature is influenced strongly by a boundary value. Note that instabilities driven by ion temperature gradients (ITGs) [84-87] and trapped electron modes (TEMs) [88] show exactly the observed feature of a temperature gradient scale length limit. Since the temperature at the shoulder of the H-mode pedestal is raised owing to high triangularity, the core temperature may be increased due to the effect of profile stiffness. The edge-core relationship of temperature profiles is analyzed in detail in section 4.5.

4.4. Pedestal characteristics

As is seen in figure 4.5(c), triangularity affects directly the edge toroidal magnetic flux surfaces. In this section, the pedestal structure imposed by the ELM activities is examined for the cases of low and high triangularity. A comparison of the pedestal characteristics between low and high triangularity ELMy H-mode plasmas is shown as a diagram for the pedestal density (n_e^{ped}) and temperature (T_e^{ped}) in figure 4.6. The values of n_e^{ped} and T_e^{ped} are deduced by the time average over several ELM cycles (not only in time intervals just before ELMs but

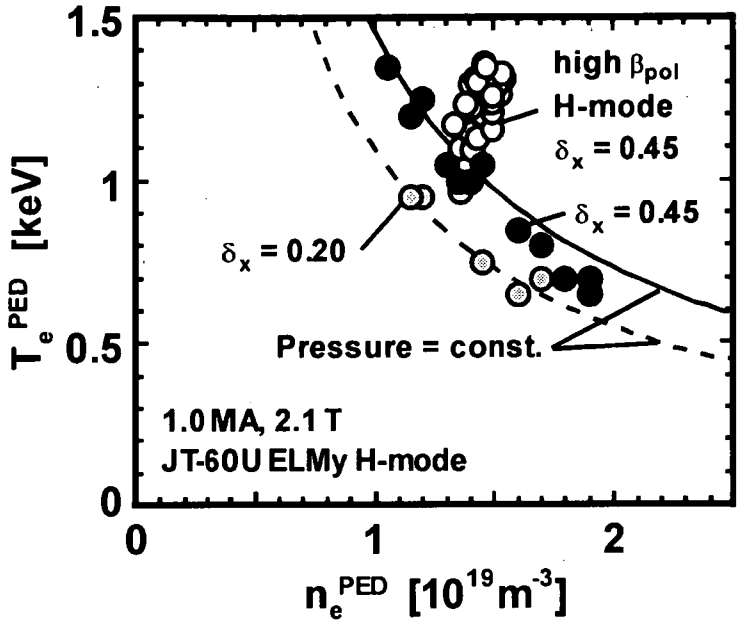

Figure 4.6 Diagram of $n_e^{ped} - T_e^{ped}$ for ELM H-mode plasmas in JT-60U. Closed and shaded circles indicate high and low triangularity ELMy H-mode plasmas (δ_x = 0.45 and 0.20) at I_p / B_t = 1.0 MA / 2.1 T, respectively. Open circles indicate high β_{pol} ELMy H-mode plasmas with ITB which were performed at I_p / B_t = 1.0 MA / 2.1 T.

including the phase immediately after ELMs) of each quantity calculated at the shoulder of the H-mode pedestal. The time window is ~ 100 ms during the steady state phase of a discharge. At a fixed I_p of 1.0 MA, high triangularity ELMy H-mode plasmas produce higher pedestal temperature than low triangularity plasmas at a given density. Besides, it is seen in high triangularity plasmas that the pedestal pressure, p^{ped}, tends to decrease gradually with density. Figure 4.6 also indicates a time trace of the pedestal for a high β_{pol} ELMy H-mode discharge with an ITB [32,33,75,89] due to high power additional heating, the density and temperature profiles of which are shown in figure 4.7(a) and (b). With high triangularity, it can be seen that the high β_{pol} H-mode plasma reaches higher critical pedestal pressure.

The dependence of the poloidal beta at the pedestal, β_{pol}^{ped}, upon triangularity is plotted in figure 4.8. Here β_{pol}^{ped} represents the pedestal pressure,

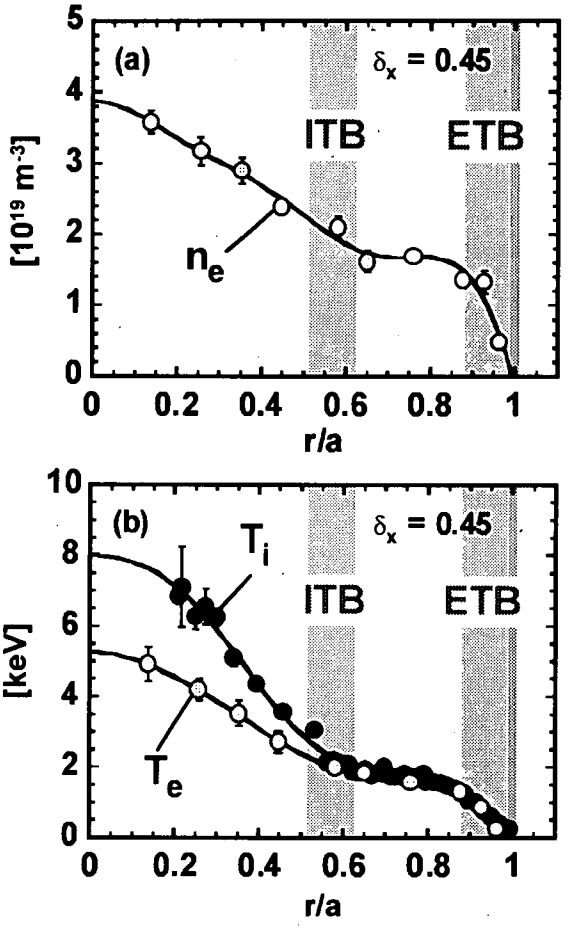

Figure 4.7 Radial profiles of (a) the electron density, (b) electron and ion temperatures in high β_{pol} ELMy H-mode plasmas at high triangularity ($\delta_x = 0.45$).

p^{ped}, normalized to the averaged poloidal magnetic field on the plasma surface, B_p, defined as:

$$\beta_{pol}{}^{ped} \equiv \frac{p^{ped}}{B_p^2 / 2\mu_0} \tag{4.1}$$

where μ_0 denotes the vacuum permeability. A comparison of standard ELMy H-modes without ITB between low and high triangularity discharges indicates that the achievable upper boundary of $\beta_{pol}{}^{ped}$ tends to increase gradually with increasing triangularity. In the high β_{pol} H-mode plasma, which corresponds to the discharge shown in figure 4.6 (open circles), the pedestal confinement is improved

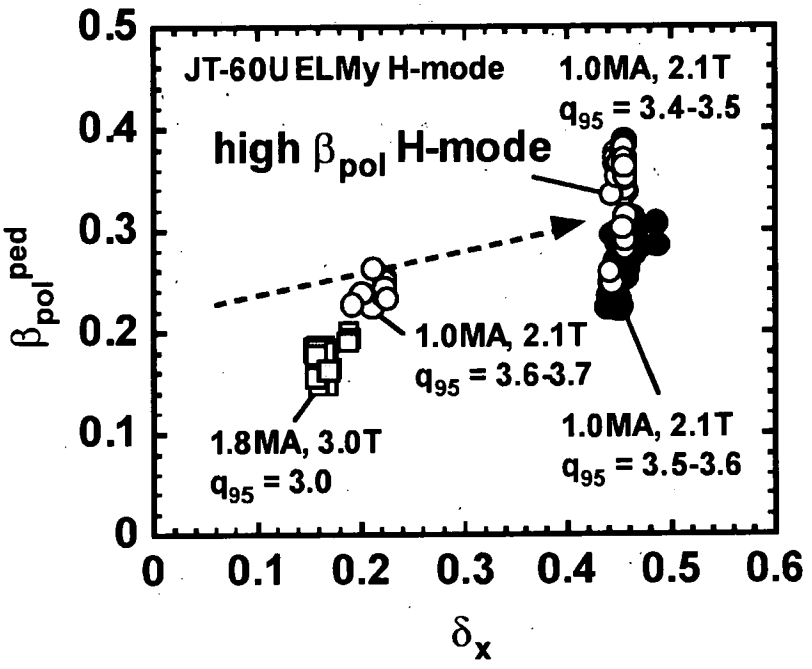

Figure 4.8 Dependence of the pedestal poloidal beta, β_{pol}^{ped}, upon triangularity at the separatrix, δ_x in ELMy H-mode plasmas. Closed and shaded circles indicate the standard ELMy H-mode plasmas without ITB at I_p / B_t = 1.0 MA / 2.1 T, respectively. Shaded squares are also the standard ELMy H-modes at I_p / B_t = 1.8 MA / 3.0 T. Open circles are high β_{pol} ELMy H-mode plasmas with ITB which were performed at I_p / B_t = 1.0 MA / 2.1 T at high triangularity.

further compared with the standard H-mode plasmas at high triangularity (δ_x ~ 0.45). This finding might be indicative of the stability improvement at the edge due to total β_{pol} increased by ITB formation. Thus, significantly high confinement is obtained by high pedestal pressure as well as the core improvement due to ITB formation. In JT-60U, the pedestal improvements have been observed in ELMy H-mode discharges with high triangularity and high β_{pol} [90]. A detailed stability analysis is required to investigate the feasible correlation among core and pedestal parameters in high β_{pol} discharges. The thermal energy confinement properties of high β_{pol} H-mode plasmas are presented in detail in section 4.6.

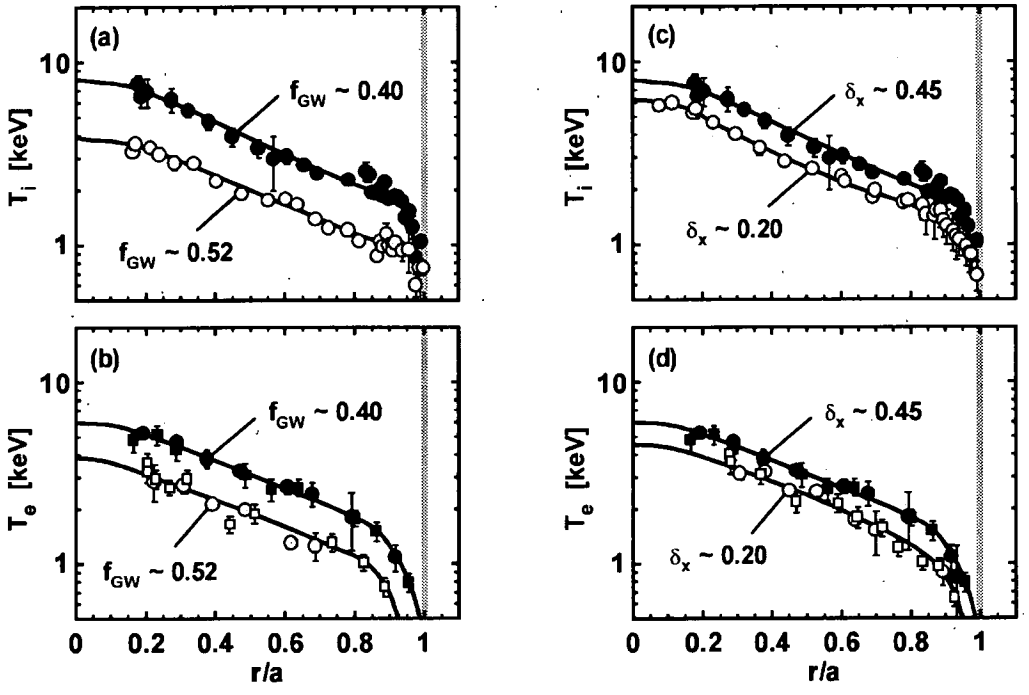

Figure 4.9 Similarity of ion and electron temperature profiles of ELMy H-mode plasmas for a variety of density and triangularity. Shown are cases with I_p = 1.0 MA, B_t = 2.1 T and P_{NBI} = 9.0 MW.

4.5. Boundary condition for thermal energy confinement

It has been identified in many tokamaks that the thermal energy confinement in H-mode plasmas depends strongly upon the temperature at the shoulder of the H-mode pedestal [27,54,58,59,78,79]. These results may be mainly linked to the profile similarity in the temperature. The profiles of temperature are seen to be self-similar in the sense that there is a minimum scale length of temperature gradient,

$$L_T = \left[\frac{1}{T}\frac{dT}{dr}\right]^{-1} = \left[\frac{d(\ln T)}{dr}\right]^{-1} \qquad (4.2)$$

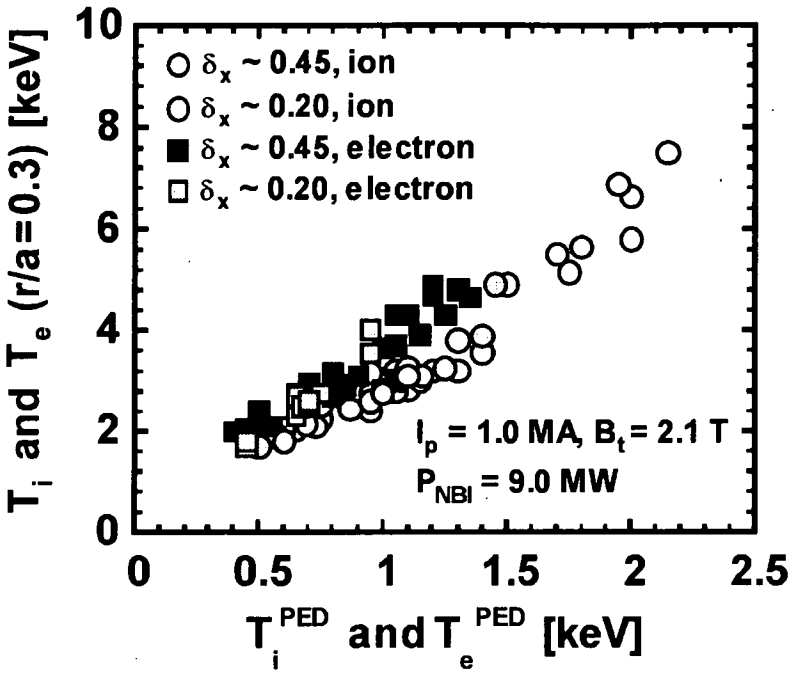

Figure 4.10 Profile similarity of ELMy H-mode plasmas in JT-60U: the core temperatures at r/a = 0.3 at high triangularity (δ_x = 0.45) for ions (open circles) and electrons (closed squares) are proportional to the temperatures at the shoulder of the H-mode pedestal, respectively. Shaded circles and squares indicate the core T_i and T_e at low triangularity (δ_x = 0.20), respectively.

which can be achieved and the energy transport adjusts to maintain this scale length [59]. In figure 4.9, the profile stiffness is shown both for ion and electron temperatures in a variety of discharges with a range of densities and plasma shapes. The core temperatures are varied according to a vertical offset of the profiles on a log scale where changing boundary temperatures at constant gradient scale length result in self-similar profiles.

Figure 4.10 shows the proportionality of the core temperatures to the pedestal temperatures for each species. It can be seen that this proportionality is the same for high and low triangularity plasmas. Therefore, the pedestal temperature is a key boundary factor for the core energy confinement through the

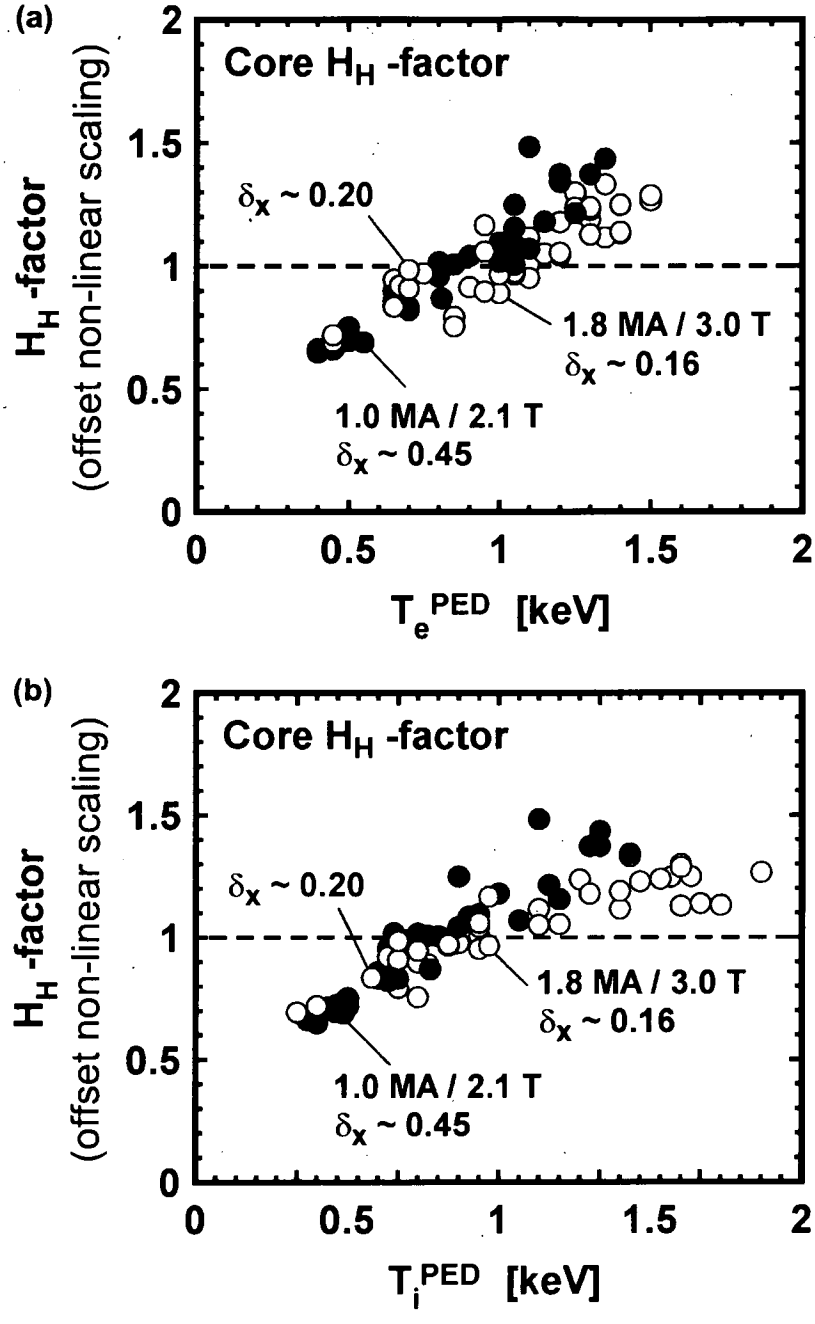

Figure 4.11 Influence of the pedestal temperatures for (a) electrons and (b) ions on the energy confinement enhancement factor of the plasma core evaluated by the offset non-linear (ONL) scaling. Closed and shaded circles indicate the H_H-factors of the core component of $\delta_x = 0.45$ and 0.20 at I_p / B_t = 1.0 MA / 2.1 T, respectively. Open circles are of δ_x = 0.16-0.18 at I_p / B_t = 1.8 MA / 3.0 T.

stiff profile of temperature. Higher triangularity plasmas have higher temperature at the pedestal shoulder at a given density, which in turn leads to an increase in the core temperature, resulting in the improvement of the energy confinement of H-mode plasmas. The effects of the pedestal temperature for each species on the energy confinement of the plasma core are shown in figure 4.11(a) and (b). At all triangularities, the H_H-factor of the plasma core based on the offset non-linear (ONL) scaling [70] increases as the pedestal temperature increases for each species. It can be expected consistently from figure 4.10 that, at a fixed I_p (= 1.0 MA) and B_t (= 2.1 T), the H_H-factors of higher triangularity discharges ($\delta_x \sim 0.45$) show approximately similar trends for the temperatures at the pedestal shoulder to those of lower triangularity discharges ($\delta_x \sim 0.20$).

4.6. High β_{pol} H-mode plasmas

In ITER, the investigation of improved confinement modes accompanied with ITB [91-93] is required from a viewpoint of development of an economically attractive fusion reactor. Besides, tokamak operation in the high β_{pol} regime is a promising concept for a steady-state tokamak reactor [94,95]. Of the several advanced confinement modes in tokamaks, the high β_{pol} mode was discovered during high β_{pol} experiments in JT-60 [32]. The safety factor profile of the mode is basically monotonically increasing with the minor radius. This mode needs a strong central heating into the plasma without sawtooth oscillations, with the safety factor at the center larger than unity. Because of its steep pressure gradient, it had been difficult to sustain high energy confinement at steady state. However, in JT-60U [96], quasi-steady high β_{pol} ELMy H-mode discharges with enhanced confinement and high β stability have been obtained at high triangularity without a harmful increase in impurity and particle recycling. Optimization of the pressure profiles characterized by the double transport barriers enabled sustainment of high

Table 4.1 Parameters of high β_{pol} H-mode discharges at high triangularity

Shot	I_p [MA]	B_t [T]	$\bar{n}_e$ [$\times 10^{19} m^{-3}$]	κ	δ	q_{95}
32226	1.0	2.1	2.1	125	0.43 – 0.45	3.5
32358	1.0	2.1	3.0 – 4.0	5	0.45	3.5
32511	1.0	3.6	2.1 – 3.1	1153	0.48 – 0.51	5.8 – 6.1
32519	1.0	3.6	1.7 – 1.9	16	0.44 – 0.47	5.6 – 5.9
32520	1.0	3.0	1.7 – 2.4	45	0.45 – 0.49	4.8 – 5.2

performance in long pulses. As shown in section 4.5, the energy confinement properties in the standard ELMy H-mode plasmas are determined by the close relationship between the pedestal and core temperature profiles. A formation of the ITB has been considered to break the edge-core relationship and enable an unrestrained development of thermal energy stored in the plasma core. In this section, thermal energy confinement properties in high β_{pol} H-mode plasmas are presented and the correlation between the pedestal and core confinement are discussed.

Data treated here are composed of high β_{pol} H-mode discharges with high triangularity (δ_x = 0.43-0.51) at I_p = 1.0 MA. Table 4.1 shows the main plasma parameters in each discharge. Toroidal magnetic field, B_t, and q_{95} are in a wide range of 2.1-3.6 T and 3.5-6.1, respectively. The time evolutions of main plasma parameters in two high triangularity ELMy H-mode discharges with an unclear ITB (case (a); shot 32519) and with a clear ITB (case (b); shot 32520) are given in figure 4.12(a) and (b), respectively. In these experiments, the NB injection power, P_{NBI}, was varied in steps during the discharge from 4 to 15 MW. In the case (a), $\bar{n}_e$ was raised from 1.5×10^{19} to 1.7×10^{19} m^{-3} by the L-H transition and then kept roughly constant. The global stored energy, W_{dia}, was increased from 0.6 to 2.0 MJ with an increase in P_{NBI}. On the other hand, in the case (b), $\bar{n}_e$ remained almost constant at (1.7-1.9)$\times10^{19}$ m^{-3} until an ITB was formed at t = 8.6 s, and the ITB formation increased $\bar{n}_e$ to 2.5×10^{19} m^{-3}. The ITB formation also increased W_{dia} to

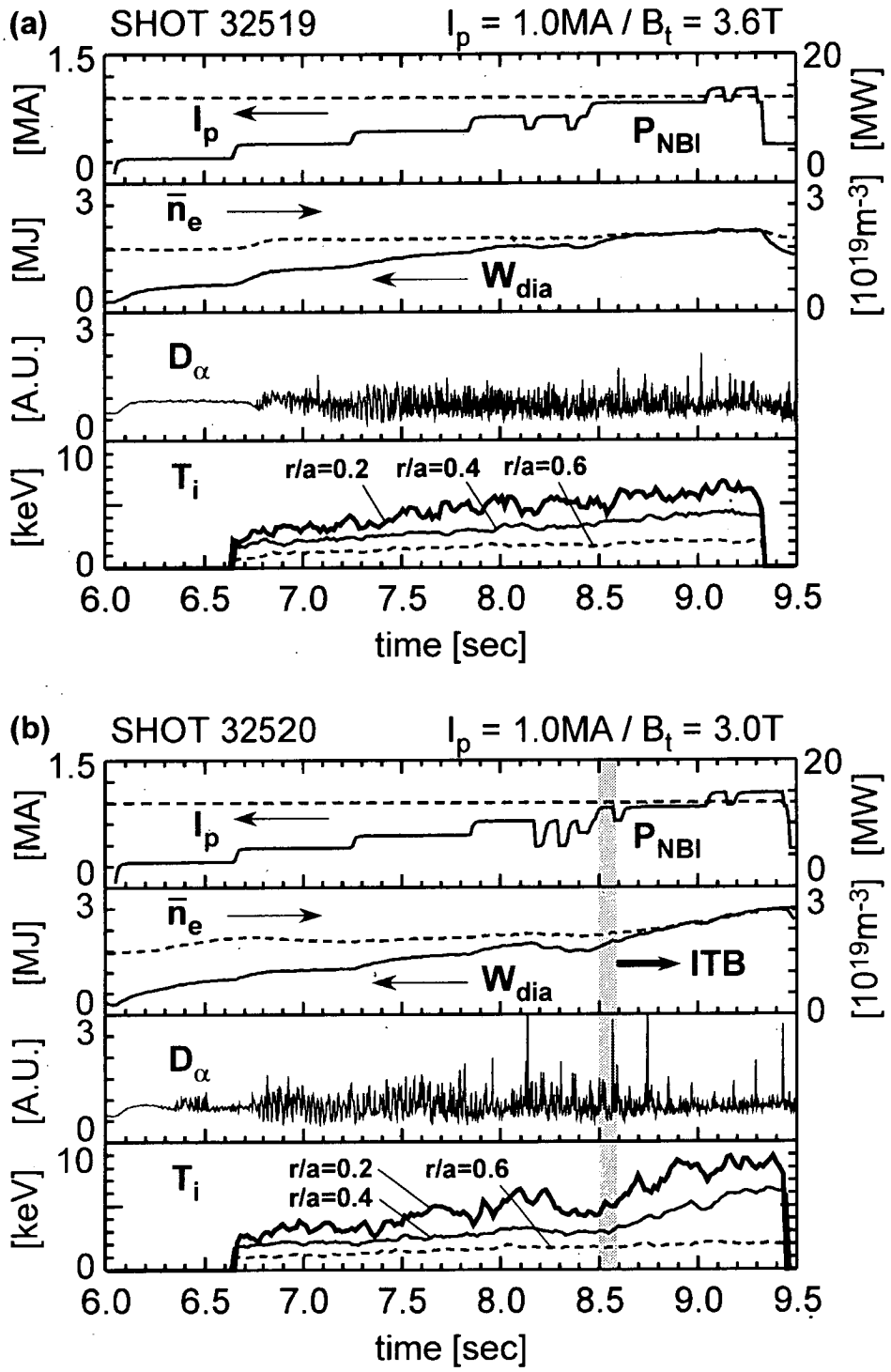

Figure 4.12 Time evolutions of plasma parameters in high triangularity ELMy H-mode discharges (a) with an unclear ITB (shot 32519) and (b) with a clear ITB (shot 32520). In the high β_{pol} H-mode discharge (shot 32520), the start of ITB formation is shown by a dark column.

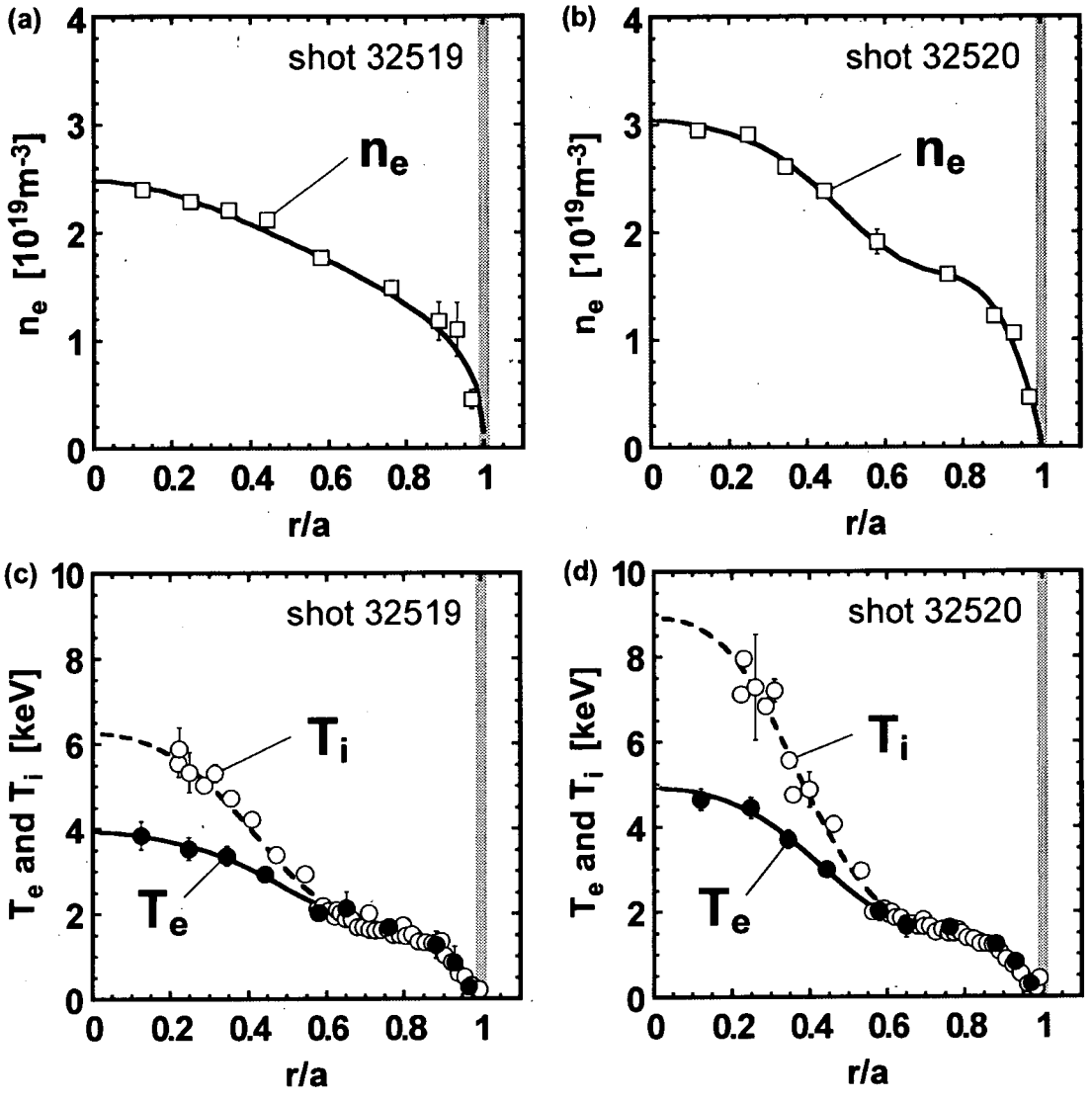

Figure 4.13 Radial profiles of n_e, T_e and T_i in high triangularity ELMy H-mode plasmas with an unclear ITB (shot 32519) and with a clear ITB (shot 32520). (a) The n_e profile of shot 32519. (b) The n_e profile of shot 32520. (c) The profiles of T_e and T_i of shot 32519. (d) The profiles of T_e and T_i of shot 32520. The separatrix position is shown by a dark column.

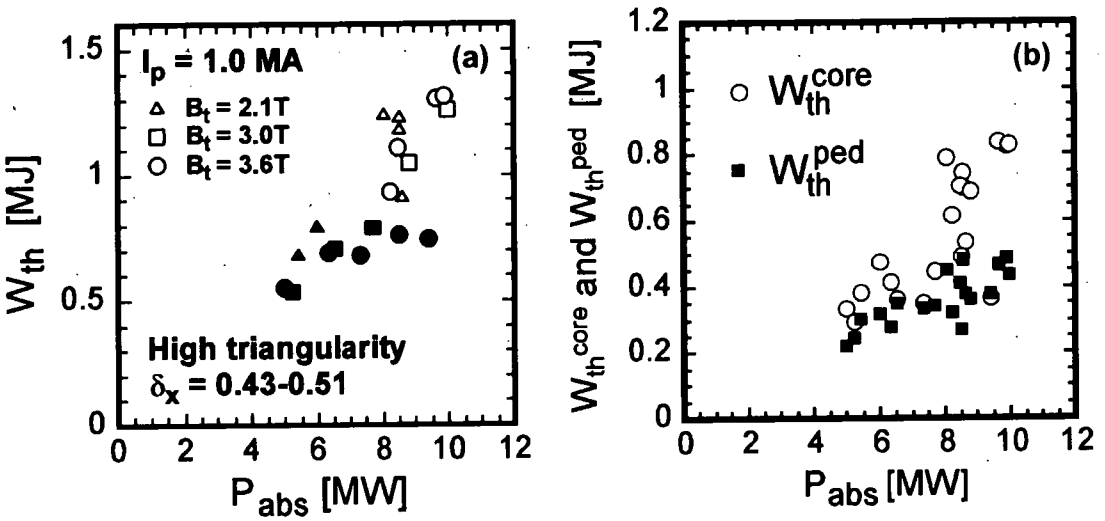

Figure 4.14 (a) Power dependence of the thermal stored energy (W_{th}) in high triangularity ELMy H-mode plasmas. Open and closed symbols indicate the plasmas with and without the ITB, respectively. (b) Power dependence of the core and pedestal stored energy (W_{th}^{core} and W_{th}^{ped}) in the plasmas shown above.

2.5 MJ at t = 9.4 s. After the L-H transition, the H-factor ($\equiv \tau_E / \tau_E^{ITER89P-L}$) and β_{pol} increased gradually from 1.5 to 1.9 and from 0.7 to 1.3 in the case (a), while it increased from 1.5 to 2.3 and from 0.8 to 1.8 in the case (b), respectively. It can be found in the case (b) that the ELM activities become weaker after the ITB formation at t = 8.6 s. In JT-60U, such small ELMs, which are referred to as Grassy ELMs, can be observed at $\delta \geq$ 0.3-0.4, $q_{95} \geq$ 5-6 and $\beta_{pol} \geq$ 1.6 [97]. According to the ideal stability analyses including finite surface current, in type-I ELMy H-mode discharges, the plasma edge is in the first stability regime and the pressure gradient hits the critical value for the ballooning mode. The access to the second stability regime for high-n ballooning mode is considered as one of the candidates for disappearance of type-I ELMs [98]. In the case (b), an increase in β_{pol} due to the ITB formation might improve the edge stability as discussed in section 4.4.

Radial profiles of n_e, T_e and T_i for these two high triangularity ELMy H-mode discharges with an unclear ITB (shot 32519) and with a clear ITB (shot 32520) at P_{NBI} = 11 MW (t = 9.0 s) are shown in figure 4.13. In the high β_{pol} H-mode, such double transport barriers are produced in the ion heat transport channel over a wide range of operation regions. In contrast, a drop in the electron heat transport at the ITB is not always observed. However, in the high triangularity discharges, the ITB for electrons tends to be observed. The dependence of the thermal stored energy, W_{th}, on the absorbed power, P_{abs}, in high β_{pol} H-mode plasmas is shown in figure 4.14(a). In case that a clear ITB is not formed, W_{th} is increased gradually with P_{abs} and is saturated at a further increase in the heating power. On the other hand, in the discharges accompanied with the ITB at I_p = 1.0 MA, it can be seen that W_{th} is increased rapidly from 0.8 to 1.3 MJ by the formation of the ITB at $P_{abs} \sim 8$ MW.

In the high β_{pol} mode, it is also observed that the ITB formation occurs at an approximately constant P_{abs} in spite of a wide range of B_t [99]. It has been seen in the standard ELMy H-mode plasmas that the energy confinement of the plasma core can be described by edge pedestal parameters as well as global parameters. To relate the observed variation in the thermal energy confinement to the changes in the edge parameters in high β_{pol} H-mode discharges, one can separate out the pedestal energy content from the total thermal energy content, and analyze how the two components vary with P_{abs}. A simple way to do this is to assume that the thermal stored energy, $W_{th} = W_{th}^{ped} + W_{th}^{core}$, in accordance with the definition presented as Eqs. (3.7) and (3.8) in chapter 3. Figure 4.14(b) indicates the dependence of the thermal energy stored in the core and pedestal components (W_{th}^{core} and W_{th}^{ped}) on P_{abs}. The presence of the ITB improves explicitly the core performance, while it is observed that W_{th}^{ped} also tends to increase in discharges with the ITB.

As can be expected by this result, it is found that W_{th}^{core} is correlated to

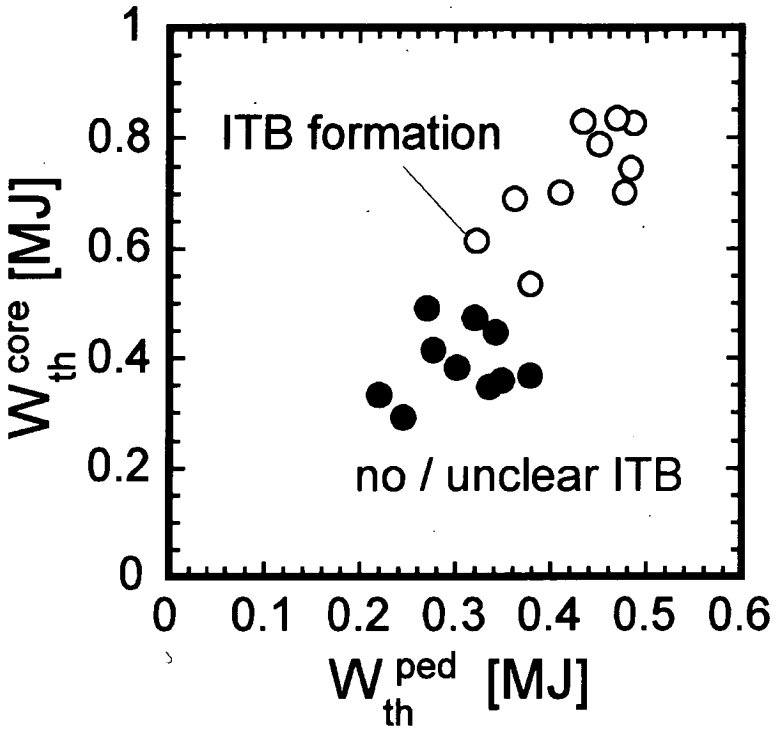

Figure 4.15 Correlation between the pedestal and core stored energy (W_{th}^{core} and W_{th}^{ped}) in high triangularity ELMy H-mode plasmas. Open and closed circles indicate the plasmas with and without the ITB, respectively.

W_{th}^{ped}, with the higher thermal energy stored in the plasma core corresponding to higher pedestal energy. This is shown for high triangularity and high β_{pol} experiments performed at I_p = 1.0 MA in figure 4.15. As shown in this figure, in the standard ELMy H-mode plasmas without the ITB, the variation in p^{ped} or W_{th}^{ped} is small, while higher W_{th}^{ped} tends to be obtained in high β_{pol} H-mode plasmas with the ITB. The improvement of the edge pedestal stability in the type-I ELMy H-mode regime has been observed with high δ and high β_{pol} in JT-60U [90]. Possible linkage among pedestal and core parameters has also been proposed based on variety of high β_{pol} H-mode experiments, where the β_{pol}-dependence may be attributed to increasing Shafranov shift or increasing field line curvature at the lower field side. It has not been concluded whether higher edge pedestal pressure

or temperature helps the ITB formation. However, at least for high β_{pol} mode discharges, higher triangularity plasmas seems to have relatively lower threshold heating power for the ITB formation accompanied with a clear transport barrier for T_e [96].

4.7. Conclusions

High triangularity ELMy H-mode experiments ($\delta_x \sim 0.45$) were carried out in JT-60U. In relatively low density regime ($\bar{n}_e/n^{GW} < 0.5$) where the type-I ELMs were observed, high triangularity discharges produced higher pedestal pressure; higher pedestal temperature was obtained at a given density. In the high density regime ($\bar{n}_e/n^{GW} > 0.5$) at fixed NB heating power type-III ELMs were generated and the pedestal pressure reduced gradually with density. A comparison between low and high density plasmas at high triangularity has shown that an increase in density led to a reduction in the both pedestal and core temperatures as observed in low triangularity ELMy H-mode plasmas. Compared to low triangularity plasmas at low densities, higher pedestal temperature was obtained at high triangularity and the core temperature was also improved by an almost same factor. The observed proportionality between the core and pedestal temperatures was independent of triangularity. In the standard ELMy H-mode plasmas, the profiles of temperature were stiff in the sense that there existed a minimum scale length of temperature gradient. The improvement of the edge stability by triangularity led to higher pedestal temperature, which in turn raised the core temperature, and thus the high thermal energy confinement was obtained. High β_{pol} H-mode plasmas characterized by ITB with the H-mode edge produced higher pedestal confinement. It was observed at high triangularity that the H-mode pedestal height, which was affected by the edge stability for ELMs, was raised, when the core energy confinement was improved, or when β_{pol} was increased.

5. Thermal Energy Confinement of Argon Seeded ELMy H-mode Plasmas

5.1. Introduction

It has been proved possible in present day experiments to demonstrate high density operation modes that lower the peak heat flux onto the divertor plates sufficiently with a high level of radiation for a tokamak reactor [22]. However, it has generally been seen that such regimes operated with the standard ELMy H-mode discharges also have diminished core plasma confinement quality [52-57]. The ITER design requires ELMy H-mode operation at $H_{\mathrm{H}}^{\mathrm{IPB98(y,2)}} = 1$ and $\bar{n}_{\mathrm{e}}/n^{\mathrm{GW}} = 0.85$. A high radiation loss power fraction, $P_{\mathrm{rad}}^{\mathrm{total}}/P_{\mathrm{abs}} \sim 0.8$, could be desirable, where $P_{\mathrm{rad}}^{\mathrm{total}}$ and P_{abs} denote the total radiation loss power and the total absorbed heating power, respectively [47]. As one of the promising techniques for avoiding the performance deterioration with increasing density, controlled injection of impurity gases in ELMy H-mode plasmas are envisioned to be beneficial for energy confinement improvement in a high density regime with enhanced radiation loss power either in the main chamber or in the divertor region [35,36]. Through impurity injection, energy confinement has been improved with high radiation loss power at a high density in TEXTOR (RI-mode) in a limiter configuration [35]. Confinement improvement due to impurity injection and formation of a radiating mantle have also been reported in DIII-D in a divertor configuration [36]. High radiation and high density ELMy H-mode plasmas have been investigated using neon gas injection into the divertor region in JT-60U [100,101]. Externally puffed seed neon improved the energy confinement by ~

15 % at $\overline{n}_e/n^{GW} \sim 0.65$. On the other hand, since the presence of impurities can dilute the fuel ions in a reacting plasma, enhance radiation losses, and impairs the performance of a tokamak reactor, the impurity concentration in the core plasma must be kept very low to guarantee a burning plasma. High radiation loss power fraction near the surface and in the divertor can be, in principle, accomplished by selecting low-Z impurities, which radiate mainly at temperatures in the 100 eV range and below, and/or by confining the radiating particles to the edge and divertor region. Many tokamaks have been successful in radiating a large fraction of injected power [35,36,58,100-112]. In present day experiments, argon radiates most intensely on closed flux surfaces among neon, nitrogen and argon. Controlled injection of argon gas is also being considered to enhance the radiation loss power in ITER [47]. This has motivated H-mode experiments using argon gas injection into the main chamber in JT-60U for confinement improvement and radiation loss enhancement due to a radiating mantle at a high density [37].

An intense gas puffing for achieving the high density operation regime can cause a state of plasma discharge so-called divertor detachment, which is characterized by a simultaneous decrease of electron temperature and density towards the target, i.e. parallel momentum is dissipated in the divertor region and plasma pressure is not constant along the magnetic field lines [113-122]. The detached plasma state favors a high plasma density and low power reaching the target [119,122]. However, plasma detachment from the divertor plate is often associated with an X-point MARFE [118,121], which is characterized by appearance of strongly enhanced radiation loss power around the X-point and causes a degradation of the energy confinement in the core plasma or even a major plasma disruption. In addition, as the gas fuelling is increased in the high density operation (without impurity gas injection), the temperature at the shoulder of the H-mode pedestal drops in the type-I ELMy H-mode plasmas. As is presented in chapter 3, the confinement degradation of the plasma core is accompanied by a

low pedestal temperature. A role of the pedestal structure determined by the ELM activities is seen to be significant for the thermal transport of the plasma core through the profile stiffness [54,59,60,123].

Numerous edge pedestal quantities, such as the density and temperature, which tend to vary monotonically together, prevent us from revealing the decisive factor being the boundary condition in determining the core confinement quality. In argon gas seeded discharges, since it has been observed in many experiments that peripheral temperatures produced are higher than those of the standard ELMy H-mode plasmas without argon gas injection [35-38], the comparison of the pedestal structure between the H-mode plasmas with and without argon gas injection may give explicit information on the influence of the boundary temperature on core energy confinement, which is separated from its corresponding variation in the boundary density.

In this chapter, focusing on ELMy H-mode discharges with argon gas puff, the density dependence of the energy confinement properties at the H-mode pedestal and core plasmas is analyzed in JT-60U. The boundary condition for core confinement is also examined in comparison with discharges without argon gas injection. The effects of radiation loss power due to argon gas puffing on the heat transport of the core plasma are presented more carefully in chapter 6. The details of the ELMy H-mode experiments with and without argon gas puffing are described in section 5.2. The general results of the experiments are summarized in section 5.3. A role of the pedestal temperature as a boundary condition for the core confinement is discussed in section 5.4. Finally, conclusions are summarized in section 5.5.

5.2. Experiments of ELMy H-mode discharges with and without argon gas injection

ELMy H-mode experiments were performed with and without argon gas injection in JT-60U at I_p = 1.2 MA, where the Greenwald density limit, n^{GW}, corresponds to (5.4-5.8)$\times 10^{19}$ m^{-3} [37]. The toroidal magnetic field, B_t = 2.5-2.6 T and the safety factor at the 95 % of flux surface, q_{95} = 3.3-3.6. Neutral beam (NB) of deuterium was injected into deuterium plasma at P_{NBI} of 16-18 MW. The plasma configuration is illustrated in figure 5.1. Elongation, κ, of 1.4 and triangularity, δ, of 0.35-0.36 were fixed. The plasma volume, V_p, was in the range of 57-58 m^3. The plasma major radius, R_p, and the minor radius, a_p, were in the ranges of 3.35-3.38 m and of 0.82-0.83 m, respectively.

The positions of gas puff and divertor pump are also shown in the figure. Deuterium gas was puffed into the main chamber from the top, and argon gas into the main chamber from the lower outside in order to form a radiating mantle in the edge region of the main plasma. Neutral particles in the divertor were pumped from the private flux region through exhaust slots near both the inner and the outer strike points. The time constant of exhaust for argon was ~ 0.5 s in the high density ELMy H-mode discharges. In some discharges, the radiation loss power from the edge region ($r/a > 0.55$) was controlled with a feedback technique using argon puffing. The area observed with bolometers to control the radiation loss power from the edge plasma is also depicted in figure 5.1.

With the feedback control, quasi-stationary ELMy H-mode plasmas were sustained in the region of $P_{rad}^{total} < 0.8 P_{loss}$, where P_{loss} denotes the total loss power given as $P_{loss} \equiv P_{abs} - dW/dt$. The error in the total radiation loss power was estimated to be less than 20 %, and it was mainly ascribed to uncertainty in estimation of the spatial distribution of the radiation loss power. In a series of

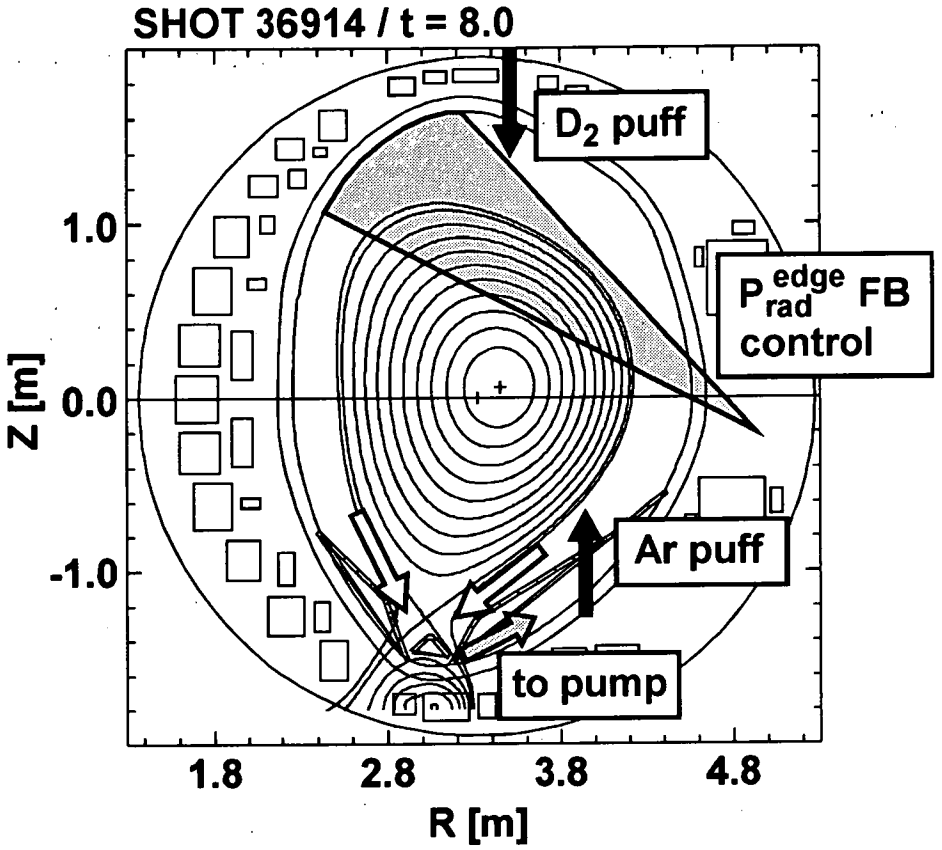

Figure 5.1 Positions of gas puff and divertor pump on the poloidal cross section of JT-60U. Also shown is the area observed with bolometers to control the radiation loss power from the edge plasma.

experiments without argon gas injection, the line-averaged electron density measured with the far infrared (FIR) interferometer, $\bar{n}_e$ [61], was varied from 2.5×10^{19} to 3.4×10^{19} m^{-3}. In argon gas injected discharges, $\bar{n}_e$ increased to 3.9×10^{19} m^{-3}. The maximum $\bar{n}_e$ reached was ~ $0.7\times n^{GW}$. In the case with argon gas puffing, the effective charge number, Z_{eff}, was in the range of 2.5-4.9, which depended upon the injected argon densities, n_{Ar}, of (0.2-0.8)%$\times\bar{n}_e$, while Z_{eff} ranged with a scatter between 2.1 and 2.5 without argon injection.

Time evolutions of ELMy H-mode discharges with and without argon gas injection are shown in figure 5.2(a) and (b), respectively. In the discharges without argon gas injection, an intense deuterium gas puff is necessary to increase the

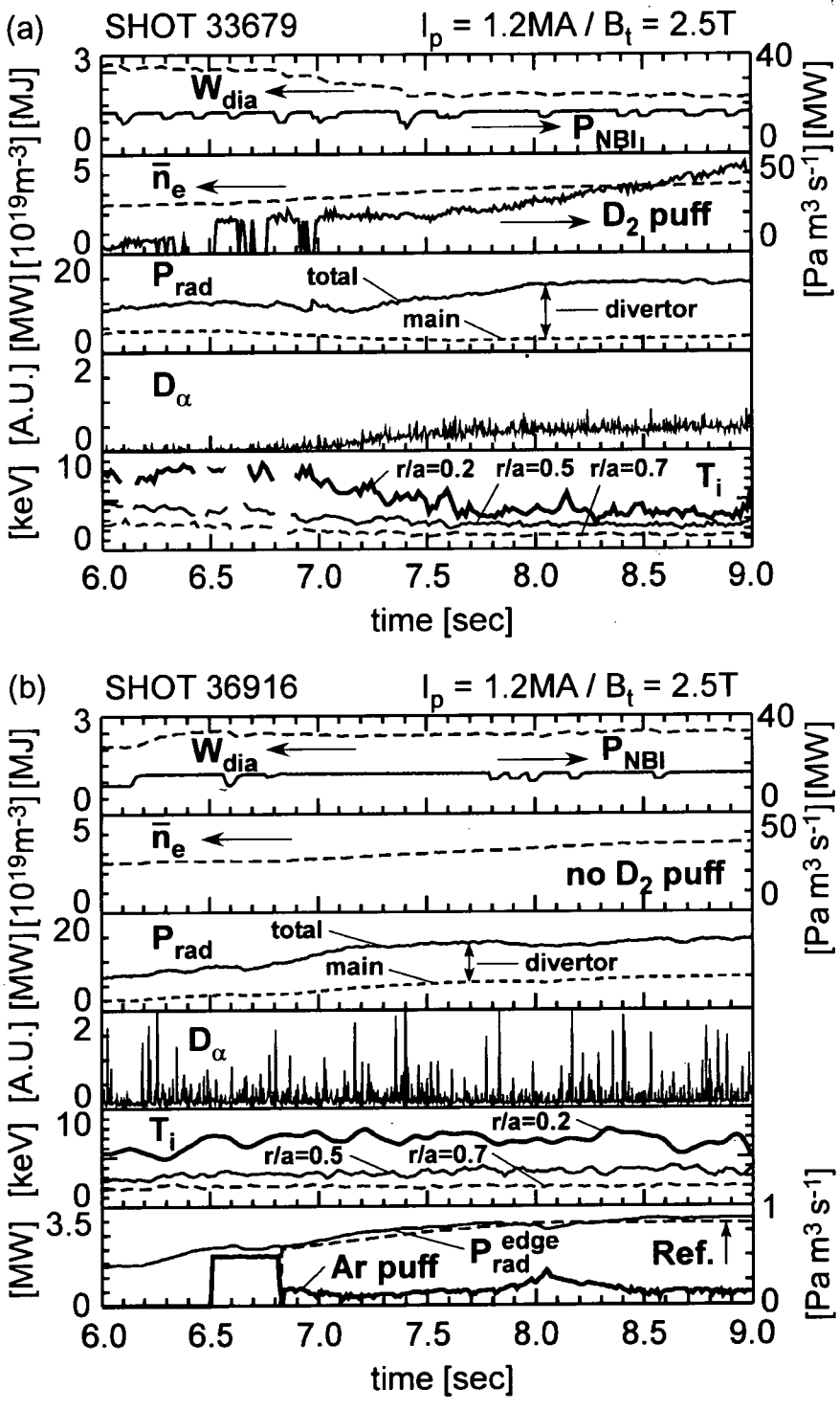

Figure 5.2 Time evolutions of plasma parameters in ELMy H-mode discharges (a) without and (b) with argon gas injection. Total radiation loss power, radiation loss power from the main plasma, and the puffing rate of deuterium and argon gases (D_2 puff and Ar puff) are also shown. Radiation loss power from the edge plasma, P_{rad}^{edge}, is controlled with a feedback technique (Ref.) using argon gas puffing.

electron density. As $\bar{n}_e$ increases with the deuterium gas puffing, the stored energy decreases. An X-point MARFE appears at t = 7.3 s, and the radiation loss power increases in the divertor plasma. The radiation loss power in the main plasma, however, remains constant and low. The D_α line intensity increases with the deuterium gas puffing. In the discharge with argon gas injection, the radiation loss power from the edge plasma, P_{rad}^{edge}, is controlled with a feedback technique using argon gas puffing. As is seen in figure 5.2(b), P_{rad}^{edge} is well controlled near the reference value by changing the argon gas puffing rate. In the argon seeded ELMy H-mode discharges, the deuterium gas puffing rate required to increase the electron density becomes lower. This might be attributable to the improvement of particle confinement. In the discharge shown in figure 5.2(b), the electron density is increased by beam fueling and recycling without deuterium gas puffing. In the high density regime, the stored energy is maintained at a high level. The basic intensity of D_α emission signals remains low, and type-I ELMs are maintained. The radiation loss power from the main plasma increases to the same level as that from the divertor plasma.

5.3. Thermal energy confinement properties

Externally puffed seed impurities as well as intrinsic impurities affect the energy balance of plasma through radiation loss. In JT-60U, the first wall is composed of graphite tiles and the divertor target is lined with carbon fiber composite (CFC) tiles. The fast particles which escape from the main plasma sputter these materials, which become impurities for the bulk plasma. In order to evaluate the impurity content, the charge neutrality condition and the estimation of Z_{eff} are used as follows:

$$\sum_j Z_j f_j = 1 \qquad (5.1)$$

$$Z_{\mathrm{eff}} = \sum_j Z_j^2 f_j \tag{5.2}$$

where Z_j and f_j ($\equiv n_j / n_e$) denote the charge number and the fraction of ion density for j-species. Due to the deuterium NB injection, the deuterium density, n_D, includes both thermalized component, n_D^{th}, and unthermalized or slowing down component, n_D^{fast}. The ionization energy of the light impurities such as carbon is sufficiently lower than the bulk electron temperature of JT-60U plasmas. Therefore except for the plasma edge region these materials are in the fully ionized state. In the following analysis in this chapter, only two species of impurity, which are carbon and argon, are taken into account. Then, an argon concentration, f_{Ar}, is given as:

$$f_{\mathrm{Ar}} = \frac{Z_{\mathrm{eff}} - Z_C(Z_C - 1)f_C - 1}{Z_{\mathrm{Ar}}(Z_{\mathrm{Ar}} - 1)} \tag{5.3}$$

For simplicity, the average charge state of argon, Z_{Ar}, is assumed to be 17 in the bulk plasma at T_e of several keV [124]. A carbon concentration, f_C, is measured with charge exchange recombination spectroscopy (CXRS) [125].

Figure 5.3(a) shows that the H_H-factor on the basis of the IPB98(y,2) scaling for different argon densities (f_{Ar} ~ 0.2, 0.5, and 0.8) as a function of $\bar{n}_e / n^{GW}$. In the plasmas without argon gas puffing at I_p = 1.2 MA, the H_H-factor decreases continuously from 0.9 to 0.7 with increasing $\bar{n}_e / n^{GW}$ from 0.44 to 0.61. In contrast, in argon injected discharges, the H_H-factor remains in the range of 0.9-1.0 until $\bar{n}_e / n^{GW}$ reaches 0.64, and then the H_H-factor declines gradually with a further increase in density. Figure 5.3(b) indicates the density dependence of thermal stored energy, W_{th}. As $\bar{n}_e$ is increased, W_{th} decreases gradually from 1.5 to 1.2 MJ in the case without argon gas puffing, while it increases to 1.9 MJ in argon injected plasmas.

The profiles of n_e, T_e and T_i in the ELMy H-mode discharges with and without argon gas injection are compared at $\bar{n}_e / n^{GW}$ = 0.58 (see figure 5.4(a) and

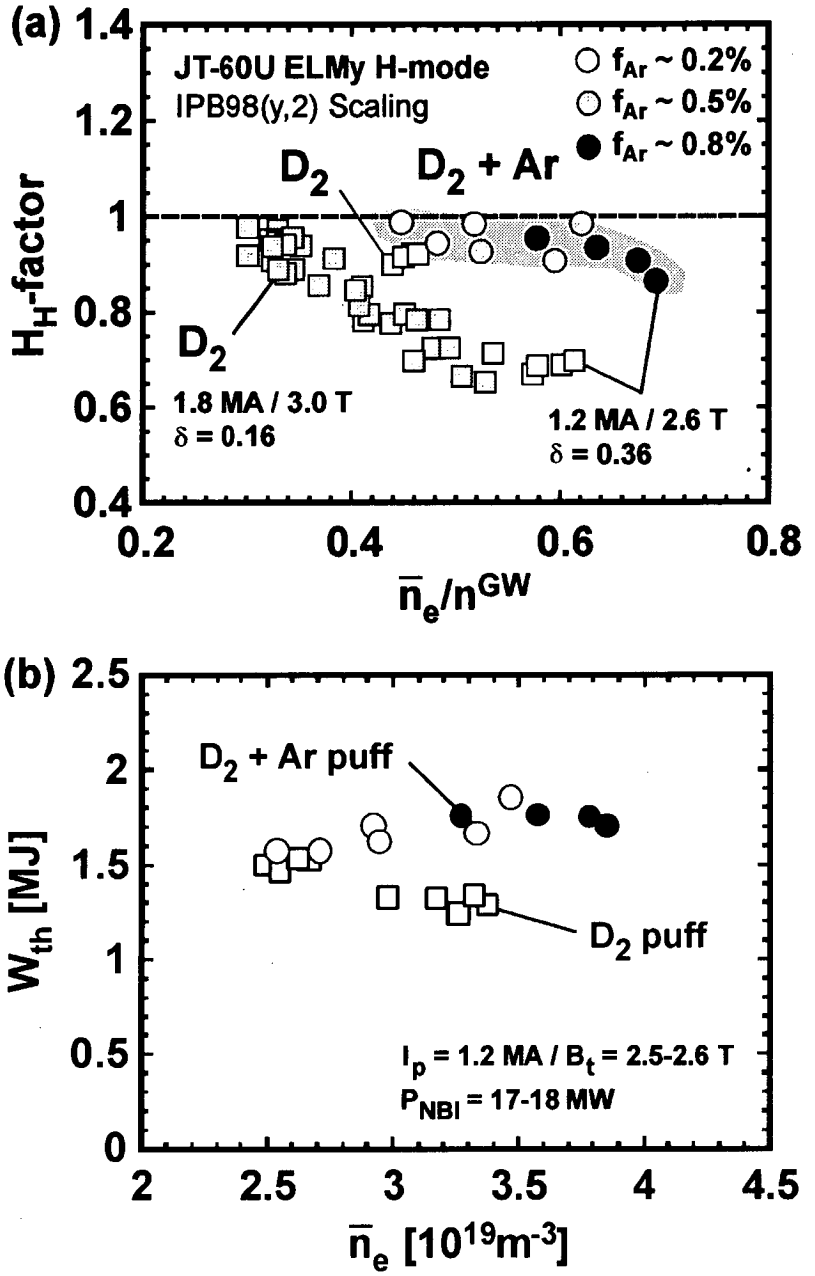

Figure 5.3 (a) The H_H-factors in ELMy H-mode discharges in JT-60U as a function of $\bar{n}_e/n^{GW}$. Open and shaded squares indicate the H_H-factors in the discharges at I_p = 1.2 MA, B_t = 2.5-2.6 T and δ ~ 0.36, and at I_p = 1.8 MA, B_t = 3.0 T and δ ~ 0.16 without argon gas puffing, respectively. The H_H-factors in the discharges with argon gas injection are shown for different argon densities. Open, shaded and closed circles are of the fraction of argon density, f_{Ar} ($\equiv n_{Ar}/n_e$) ~ 0.2, 0.5 and 0.8 %, respectively. (b) Density dependence of thermal stored energy, W_{th}, is shown for ELMy H-mode discharges with and without argon gas injection.

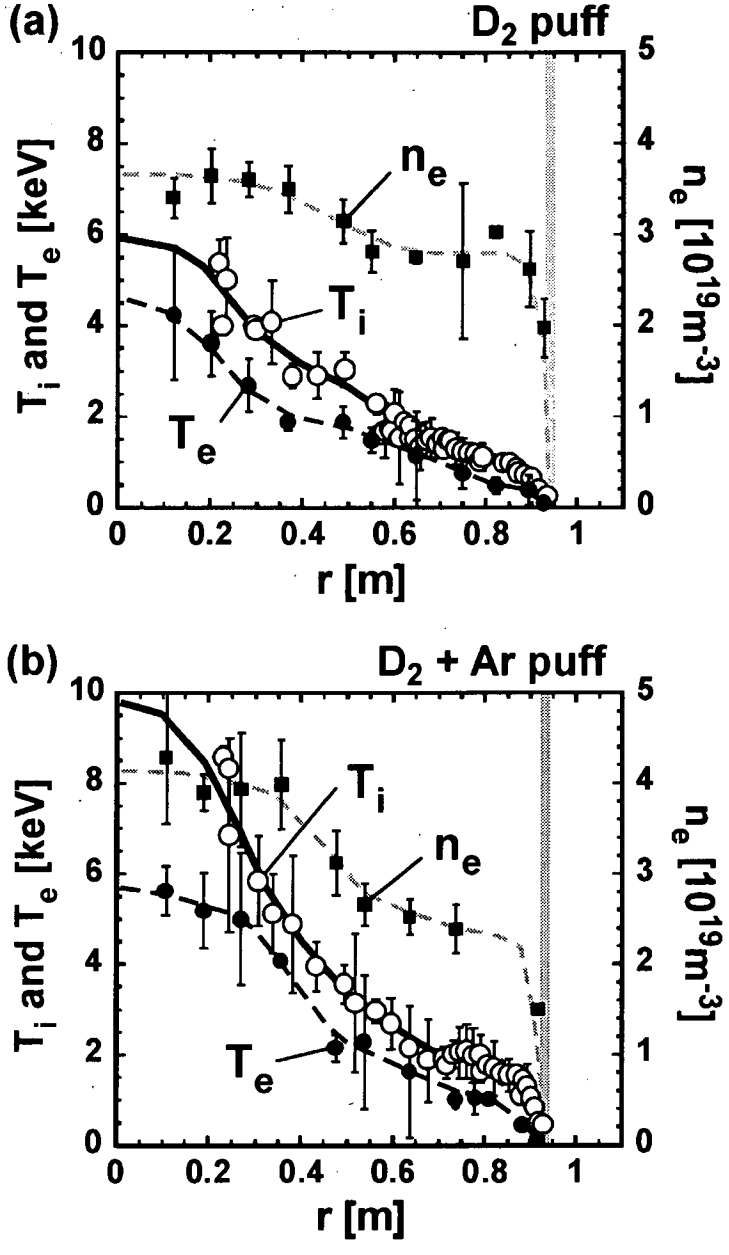

Figure 5.4 Radial profiles of T_e, T_i and n_e in the ELMy H-mode plasmas at $\bar{n}_e / n^{GW} = 0.58$ (a) without and (b) with argon gas injection. The electron density, n_e (closed squares), and the electron temperature, T_e (closed circles), are obtained by the Thomson scattering measurement with a YAG laser system. The ion temperature, T_i, is measured with the CXRS (open circles). The separatrix position is shown by a dark column.

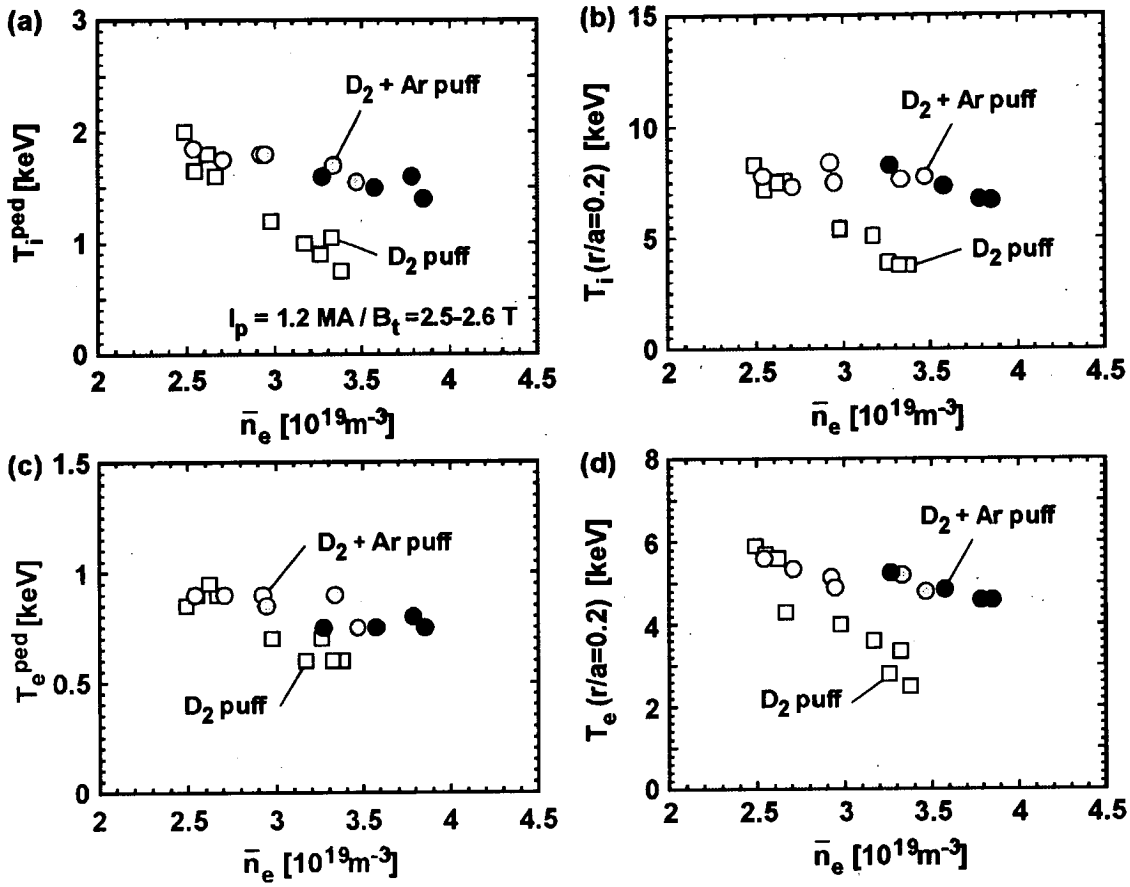

Figure 5.5 Density dependence of (a) T_i^{ped}, (b) T_i (r/a = 0.2), (c) T_e^{ped} and (d) T_e (r/a = 0.2) in ELMy H-mode discharges with and without argon injection. Closed squares indicate the discharges without argon gas injection. Open, shaded and closed circles are of the fraction of argon density, f_{Ar} ($\equiv n_{Ar}/n_e$) ~ 0.2, 0.5 and 0.8 %, respectively.

(b)). In the plasma with argon gas puffing, both T_e and T_i are higher at the H-mode pedestal and in the core region than those of the plasma without argon gas puffing. It is also seen in the figures that the density profile in the argon seeded plasma is peaked at the center. It is noted in the plasma with argon gas puffing that, while the radiation loss power is predominantly enhanced in the edge region, the power radiated from the region of r/a < 0.6, which is several times larger than that without argon injection, is ~10 % of the heating power injected into the region [38]. Figure 5.5(a) and (b) plot the ion temperatures at the shoulder of the H-mode

pedestal, T_i^{ped}; and near the center, $T_i(r/a = 0.2)$, as a function of $\bar{n}_e$, respectively. It is observed in the plasmas without argon gas injection that both T_i^{ped} and $T_i(r/a = 0.2)$ decrease continuously with increasing $\bar{n}_e$. However, it can be seen in the argon seeded case that the reduction in T_i^{ped} due to an increase in density weakens and T_i^{ped} remains rather high even in the high density regime in comparison with the case without argon gas injection. The core temperature, $T_i(r/a = 0.2)$, also tends to decrease slowly with an increase in density. A similar behavior is also seen in the electron temperatures as shown in figure 5.5(c) and (d). More scattered T_e^{ped}, evaluated using the Thomson scattering measurement with a YAG laser system, is attributed to its small S/N ratio at lower densities.

Another noteworthy feature in the argon seeded ELMy H-mode discharges is a peaked density profile seen in figure 5.4(b). Figure 5.6(a) and (b) plot the density dependence of the pedestal electron density, n_e^{ped}, and the peaking factor of electron density profile, $n_e(0)/\langle n_e \rangle$, where $n_e(0)$ and $\langle n_e \rangle$ denote the electron density at the center and the volume-averaged electron density, respectively. Density profiles become flatter with increasing density in the discharges without argon gas injection, while the peaking factor of electron density profile does not decrease as the density increases in the argon seeded discharges.

Impurity concentration enhances the dilution of the fuel ions. The effect of argon gas injection on the fraction of thermal deuterium ion density, f_D^{th} (= n_D^{th}/n_e), is shown in figure 5.7(a). As the argon concentration, f_{Ar} (= n_{Ar}/n_e), is raised from 0.2 to 0.8 % with increasing density, the dilution of thermal deuterium ions is enhanced gradually by 10 %, i.e. f_D^{th} decreases from 60 to 50 %. The fraction of carbon density, f_C (= n_C/n_e), remains constant in the range of 4-6 %. On the other hand, f_D^{th} and f_C are in the ranges of 70-79 % and 4-5 % in the discharges without argon gas injection, respectively. Under the condition of $f_{Ar} <$ 1 %, the dominant intrinsic impurity is carbon, whose density fraction is not changed by argon gas injection, i.e. $Z_C n_C$ (~ 30 % of n_e) is larger than $Z_{Ar} n_{Ar}$,

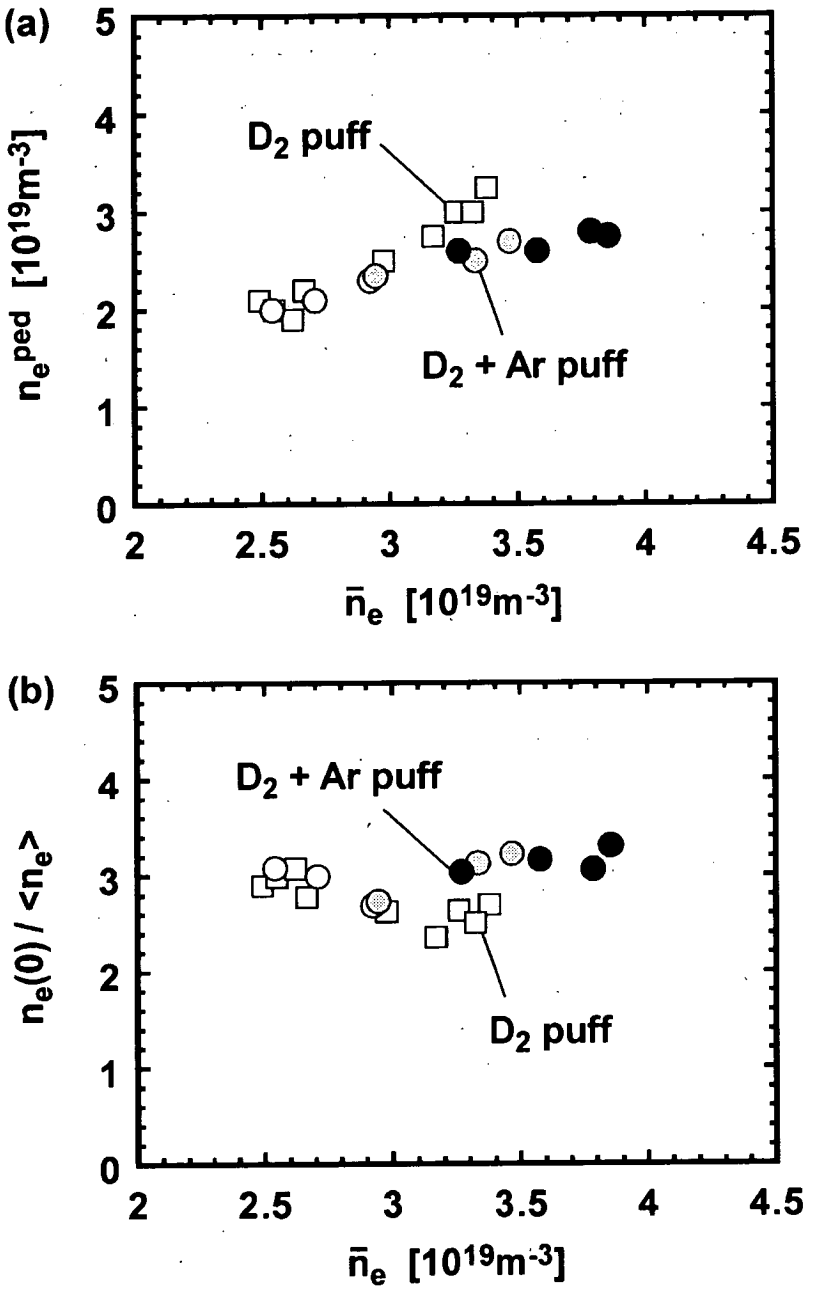

Figure 5.6 Density dependence of (a) the pedestal electron density, n_e^{ped}, and (b) the peaking factor of electron density profile, $n_e(0)/\langle n_e \rangle$, where $n_e(0)$ and $\langle n_e \rangle$ denote the electron density at the center and the volume-averaged electron density, respectively. Open squares indicate the discharges without argon gas injection. Open, shaded and closed circles are of the fraction of argon density, f_{Ar} ($\equiv n_{Ar}/n_e$) ~ 0.2, 0.5 and 0.8 %, respectively.

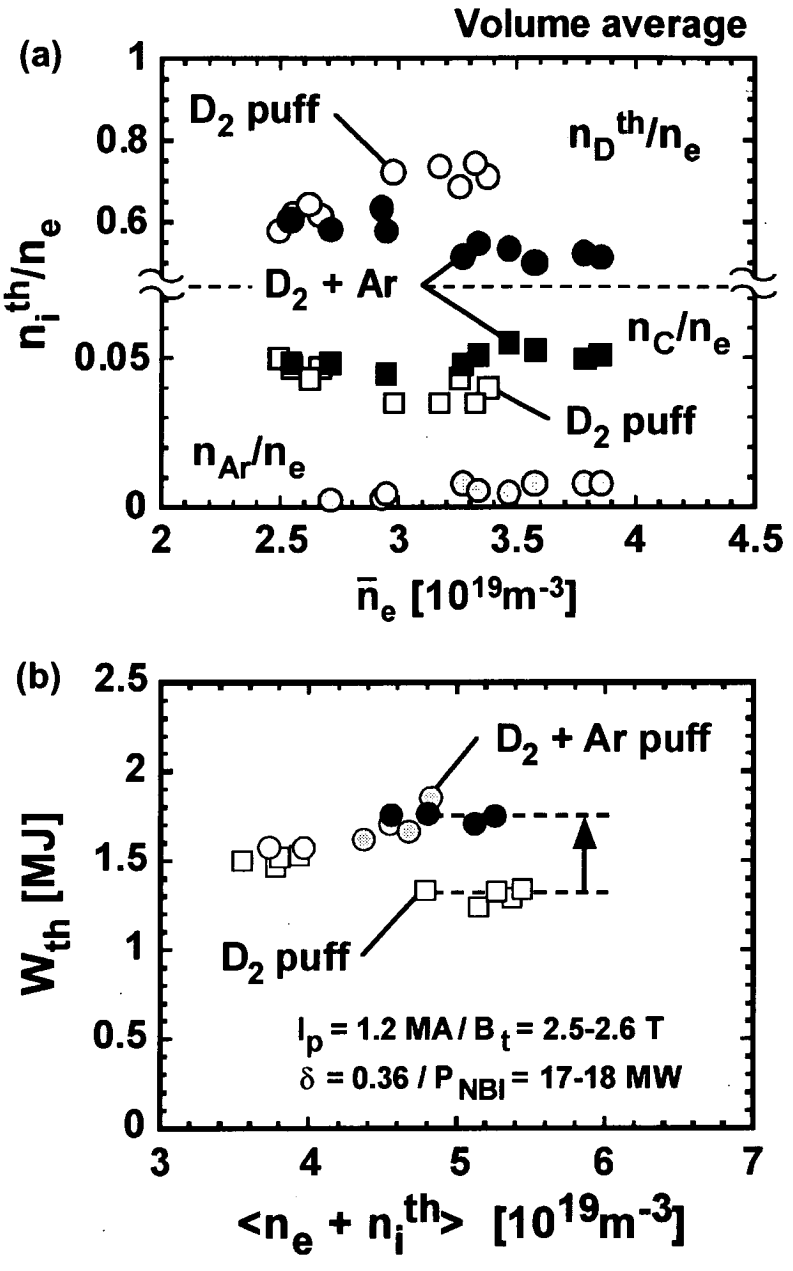

Figure 5.7 (a) The influence of impurity concentration on the dilution of thermal deuterium ion density. Closed and open circles indicate the fraction of thermal deuterium ion density, f_D^{th} (= n_D^{th}/n_e), in the plasmas with and without argon gas injection, respectively. Closed and open squares denote f_C (= n_C/n_e) in the cases with and without argon gas injection, respectively. Shaded circles indicate the argon concentration, f_{Ar} (= n_{Ar}/n_e), which is in the range of 0.2-0.8 %. (b) The dependence on the total thermal density, $<n_e + n_i^{th}>$, of W_{th}. Open squares indicate W_{th} in the discharges without argon gas injection. Open, shaded and closed circles are of the fraction of argon density, f_{Ar} ~ 0.2, 0.5 and 0.8 %, respectively.

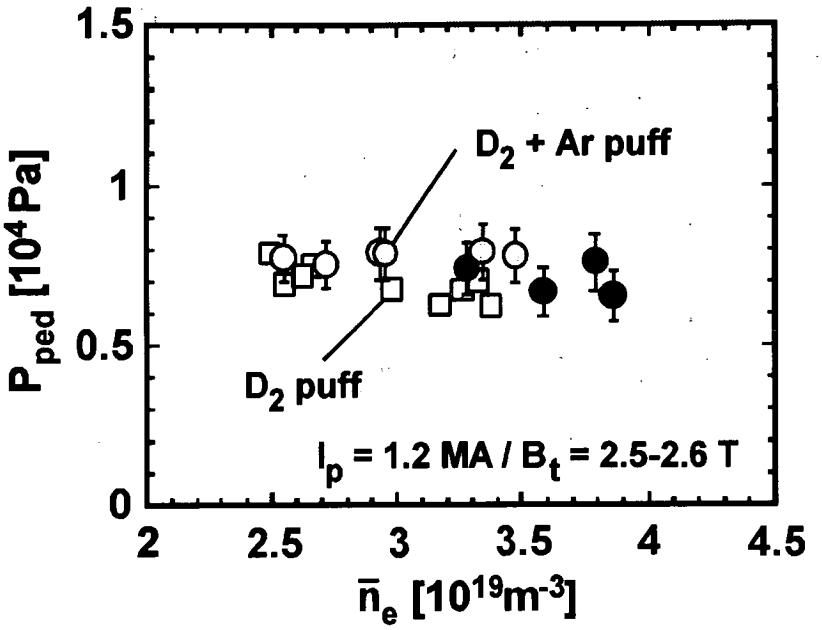

Figure 5.8 Density dependence of the edge pedestal pressure. The charge state of argon, Z_{Ar}, was assumed to be 16 at the plasma edge. Open squares indicate p_{ped} in the discharges without argon gas injection. Open, shaded and closed circles are of the fraction of argon density, f_{Ar} ~ 0.2, 0.5 and 0.8 %, respectively.

which could reach at most ~ 14 % of n_e. Therefore, the improvement of thermal energy confinement more than compensated for the dilution of deuterium ions due to impurity contamination, resulting in higher neutron production rates. As seen in figure 5.7(b), the total thermal density of ~ 5×10^{19} m^{-3} at f_{Ar} ~ 0.8 % corresponds to about a 30 % increase in W_{th}, where $n_D(0)\tau_E T_i(0)$ is improved by a factor of ~ 2. In JT-60U, the energy confinement improvement by argon gas injection is higher than that by neon gas injection (~ 15 %) [100,101].

5.4. Pedestal characteristics

As $\bar{n}_e$ is increased in the discharges without argon gas injection, the temperature at the pedestal shoulder drops as shown in figure 5.5(a) and (c). This

reduction in the temperature seems to be determined as a pedestal structure by the ELM activities. In figure 5.8, the pedestal pressures, p_{ped}, are plotted in the ELMy H-mode plasmas with and without argon gas injection as a function of $\bar{n}_e$. The pedestal pressure, p_{ped}, is evaluated as:

$$p_{ped} = n_e^{ped} k_B \left(T_e^{ped} + \sum_j f_j T_j^{ped} \right) \tag{5.4}$$

In argon gas injected plasmas, p_{ped} is kept constant in the range of 6.5-8.0$\times 10^3$ Pa over a wide range of density. Compared with the discharges without argon gas puffing, higher p_{ped} (~ 8 %) is obtained in argon seeded plasmas. As the density increases in the case with argon gas injection, the increase in the pedestal density is smaller compared with the case without argon gas injection since the thermal deuterium ion density decreases slightly and the peaked density profiles are sustained (see figure 5.6(a) and (b)). Thus, as shown in figure 5.5(a) and (c), the reduction in the pedestal temperature weakens so that p_{ped} remains constant.

5.5. Boundary condition for core confinement

It has been observed in ELMy H-mode plasmas without impurity injection that the pedestal temperature imposed by the destabilization of ELMs affect strongly the energy confinement of the plasma core as presented in chapter 3. With argon gas injection, the confinement is improved in the core region and the pedestal temperature is increased (see figure 5.5(a) and (c)).

To estimate the variation in the heat transport of the plasma core, the effective heat diffusivity of the plasma core, χ_{eff}^{core}, is evaluated in the same way as in chapter 3:

$$\chi_{eff}^{core} = \frac{\int_0^{r_{ped}} \chi_{eff}(r) \cdot 2\pi r dr}{\int_0^{r_{ped}} 2\pi r dr} \tag{5.5}$$

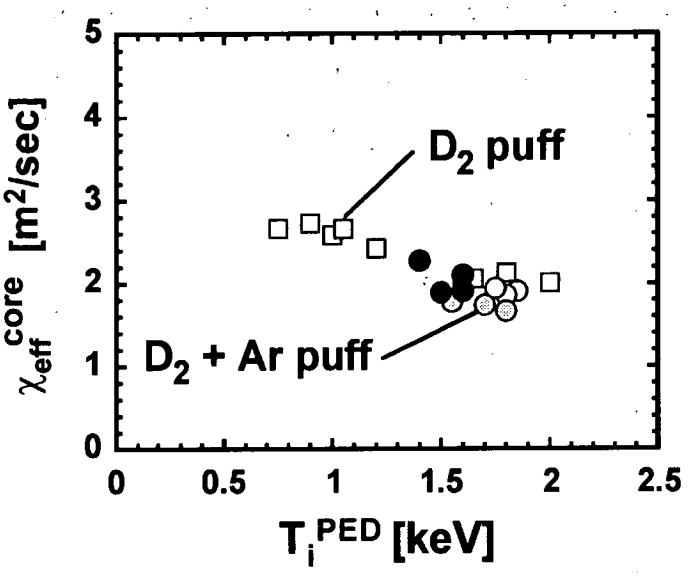

Figure 5.9 The dependence of the effective heat diffusivity of the core plasma, χ_{eff}^{core}, on T_i^{ped} in the ELMy H-mode plasmas with and without argon gas injection. Open squares indicate χ_{eff}^{core} in the discharges without argon gas injection. Open, shaded and closed circles denote χ_{eff}^{core} in the cases where $f_{Ar} \sim 0.2$, 0.5 and 0.8 %, respectively.

where $\chi_{eff}(r)$ is calculated by the transport analysis code for thermal plasmas (TOPICS) [67]. Figure 5.9 plots χ_{eff}^{core} as a function of T_i^{ped} in the discharges with and without argon gas puffing. It can be seen that χ_{eff}^{core} tends to decline gradually with increasing T_i^{ped}. It is of most significance in figure 5.9 that the trend of χ_{eff}^{core} on T_i^{ped} is roughly similar in cases with and without argon gas injection. This finding might be indicative of a profile similarity of the temperature in ELMy H-mode plasmas with and without argon gas injection. The lower χ_{eff}^{core} with argon gas puffing might be affected by higher temperature at the pedestal shoulder through the profile stiffness. However, compared with the plasmas without argon gas injection, it should be noted in figure 5.9 that χ_{eff}^{core} tends to be systematically smaller only by ≤ 15 % with a scatter at a fixed T_i^{ped} of ~ 1.7 keV in the argon seeded plasmas. This further reduction of χ_{eff}^{core}, could be explained by the effect of the radiation loss power on the energy balance and it is described in chapter 6.

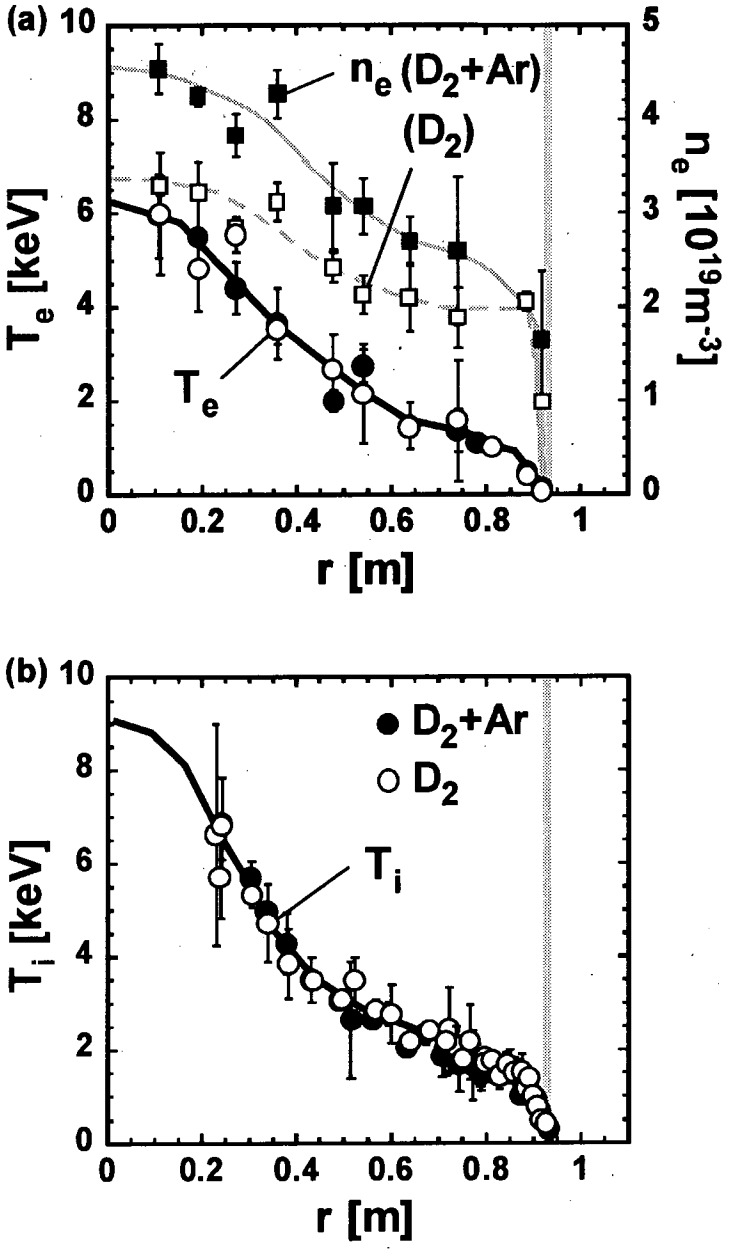

Figure 5.10 Profile similarity of the temperature profiles between a high density argon seeded ELMy H-mode plasma ($\overline{n}_e/n^{GW} \sim 0.60$ and $f_{Ar} \sim 0.5$ %) and a low density plasma without argon gas injection ($\overline{n}_e/n^{GW} \sim 0.45$). (a) The n_e, T_e and (b) T_i profiles are compared between these two plasmas. The separatrix position is shown by a shaded column.

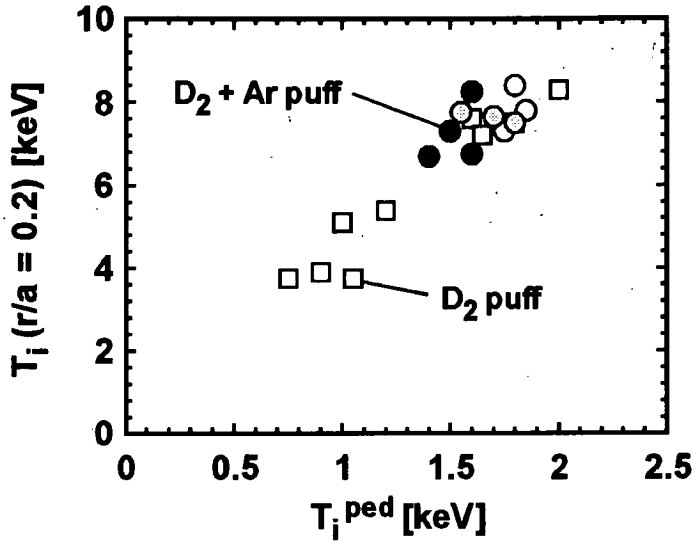

Figure 5.11 Proportionality between the core (T_i (r/a = 0.2)) and edge pedestal ion temperatures (T_i^{ped}) in ELMy H-mode plasmas with and without argon gas injection. Open squares indicate the plasmas without argon gas injection. Open, shaded and closed circles denote the cases where $f_{Ar} \sim 0.2$, 0.5 and 0.8 %, respectively.

Profile similarity of the temperature in the plasmas with and without argon gas injection is observed clearly by selecting profiles with a fixed temperature at the pedestal shoulder with different densities. Figure 5.10(a) and (b) show the n_e, T_e and T_i profiles in a high density argon seeded plasma ($\bar{n}_e/n^{GW} \sim 0.60$) and a low density plasma without argon gas puffing ($\bar{n}_e/n^{GW} \sim 0.45$). While the ion temperature at the H-mode pedestal decreases with density in the standard ELMy H-mode plasmas without impurity injection, it is kept higher at a high density by argon gas injection (see figure 5.5(a) and (c)). However, the temperature profiles of the plasma core in the argon seeded case seem approximately consistent with those of the case without argon gas injection. In a series of these discharges, the core temperatures are seen to increase approximately proportional to the pedestal temperatures in the discharges with different argon densities (see figure 5.11).

When the ELM activities limit the achievable pedestal pressure, the pedestal temperature is also determined by the pedestal density for each species as is presented in chapter 3. Argon gas puffed plasmas show a slight reduction in the thermal deuterium ion density and the center-peaked density profiles, in which the pedestal density becomes lower than that of the plasmas without argon injection at a fixed $\overline{n}_e$. Therefore, the reduction in the pedestal temperature weakens at high averaged densities. The high pedestal temperature with argon gas injection can produce high core temperature due to the profile stiffness, leading to the improvement of the energy confinement in the plasma core.

5.6. Conclusions

The density dependence of the energy confinement properties at the H-mode pedestal and core plasmas has been investigated in ELMy H-mode discharges with and without argon gas injection. Compared with the standard ELMy H-mode plasmas without argon gas puffing ($H_H^{IPB98(y,2)} = 0.7$ at $\overline{n}_e/n^{GW} = 0.6$), the energy confinement was improved in the high density regime by argon gas injection ($H_H^{IPB98(y,2)} = 0.9$-1.0 at $\overline{n}_e/n^{GW} = 0.6$). In addition, the improvement more than compensated for the dilution of deuterium ions due to argon gas injection. At high densities, higher core and pedestal temperatures were obtained with argon gas puffing. While the density profiles became flatter with increasing density in the case without argon gas injection, peaked density profiles were kept even at high densities in argon seeded plasmas. Higher pedestal temperature was obtained at roughly constant pedestal pressure by the lower pedestal density, which was given by the peaked density profile and the slight reduction in the thermal deuterium density at a fixed averaged density. Lower thermal conductivities of the plasma core were also obtained at higher boundary temperatures by argon gas injection. The core temperatures were observed to

increase in proportion to the pedestal temperatures. The puffing of seed argon gas caused a slight reduction in the thermal deuterium ion density and a peaked density profile, leading to a lower pedestal density. Thus, the reduction in the pedestal temperature in argon gas puffed plasmas was not significant at a high averaged density. Higher temperature in the core region and improved energy confinement were obtained by higher boundary temperature through the profile similarity.

6. Effects of Heat Flux on Temperature Profiles

6.1. Introduction

The temperature gradient is a key element in driving turbulent convection and causing anomalous heat transport in plasmas. The profile stiffness is believed to originate from a strong increase of transport when the temperature profile exceeds a threshold in the temperature gradient scale length. Therefore, understanding the response of temperature profiles to variations in the heating profile shape is indispensable for predicting the performance of a future fusion reactor. A saturation of local temperature in a situation of profile stiffness is considered to arise from a strong increase in heat diffusivity. Turbulence with large correlation lengths (streamers) might link transport in the edge region to transport in the core. The significant role of pedestal structure imposed by the ELM activities as a boundary condition for the heat transport in the plasma core has been observed in many devices [27,58,59,78,79]. As presented in chapter 3, the core temperatures tend to vary approximately in proportion to the temperatures at the shoulder of the H-mode pedestal in a range of accessible densities in the type-I ELMy H-mode regime on JT-60U, suggesting the existence of profile stiffness.

The temperature at the pedestal shoulder reduces with an increase in density to keep the pedestal pressure roughly constant, so that the corresponding core temperature also reduces. Based on this experimental observation, two methods have been investigated to extend the improved energy confinement regime of the H-mode in JT-60U: (1) high triangularity operation and (2) argon

gas injection. High triangularity discharges with high improved energy confinement of the plasma core have been observed with higher critical edge pressure gradient [26,126]. On the other hand, argon seeding can lead to improved energy confinement with higher peripheral temperature at a given density, compared to the cases without argon gas injection. This also provides a possible way to exhaust energy by a radiating belt around the plasma [38]. Both of the above methods indicate that an increase of the pedestal temperature imposes the core energy confinement through the profile stiffness. In chapter 4 and 5, the density dependence of thermal energy confinement properties concerning the profile similarity has been presented for the cases with and without argon injection. The effects of heat flux on the temperature profile are also of significant concern. Comparison of discharges with different triangularities enables us to check the stiff transport behavior with increased triangularity with high pedestal temperature. In argon seeded discharges, an enhanced radiation loss flux due to argon gas injection seems to affect conductive heat flux and heat diffusivity in the energy balance of plasma.

In this chapter, the temperature profile response to the variation of heat flux profile is examined in the ELMy H-mode experiments of high triangularity and argon gas injection. The experiments performed by the above methods are presented briefly in section 6.2. The heat transport mechanisms of the plasma core in the presence of temperature profile stiffness in high triangularity and argon seeded ELMy H-mode plasmas are discussed in section 6.3 and 6.4, respectively. Conclusions are given in section 6.5.

6.2. Experiments

The temperature profile and the heat transport of the plasma core are discussed in the following for three types of plasmas which are composed of low-

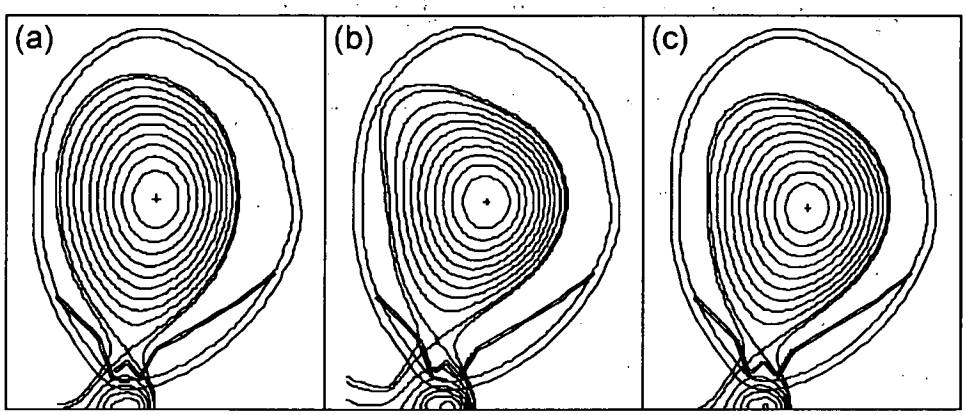

Figure 6.1 Plasma equilibria for (a) low-δ_x (~ 0.16), (b) high-δ_x (~ 0.45) and (c) argon gas injected ELMy H-mode discharges at δ_x ~ 0.35. The suffix 'x' indicates the value evaluated at the separatrix.

δ_x (~ 0.16) [79], high-δ_x (~ 0.45) [126] and argon gas injected ELMy H-mode discharges at δ_x ~ 0.35 [38]. The suffix 'x' denotes the value taken at the separatrix. Typical equilibria for these plasmas are illustrated in figure 6.1(a), (b) and (c). The experiments at δ_x ~ 0.16 and δ_x ~ 0.45 were performed at I_p / B_t = 1.8 MA / 3.0 T (q_{95} ~ 3.0) and 1.0 MA / 2.1 T (q_{95} ~ 3.5), respectively. The experiments with and without argon gas puff at medium-δ_x of ~ 0.35 were carried out at I_p / B_t = 1.2 MA / 2.6 T (q_{95} ~ 3.4). The positions of deuterium and argon gas puff on the poloidal cross section are illustrated in figure 5.1. In the transport analysis calculated for the fast ions (OFMC) [66] and thermal plasma (TOPICS) [67], data were deduced by the time average over several ELM cycles (~ 100 ms) of density and temperature profiles in quasi-stationary phases.

6.3. Effects of triangularity on plasma boundary and core transport

Plasma shaping, especially increased triangularity, is expected to have a strong influence on edge pressure gradients owing to the improvement of MHD

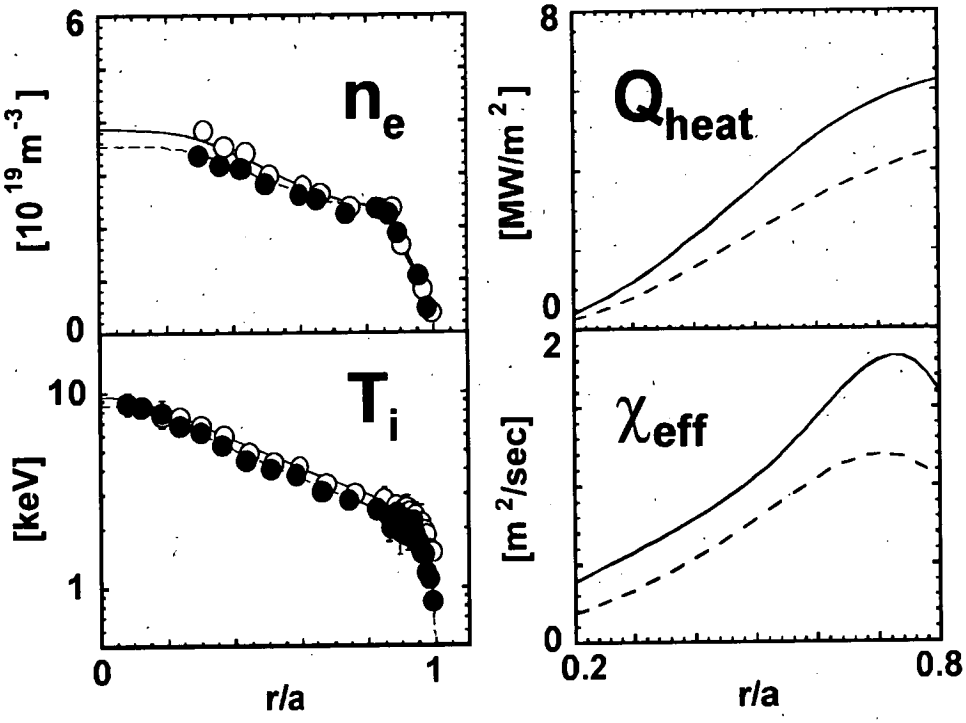

Figure 6.2 Effect of heat flux profile variation on the profiles of temperature and heat diffusivity in the JT-60U NB heated discharges for low triangularity configuration ($\delta_x \sim 0.16$) at I_p / B_t = 1.8 MA / 3.0 T. Full and dashed curves (open and closed circles) indicate the heating power absorbed in the bulk plasma, P_{abs}, of 9.4 MW and 6.8 MW, respectively.

stability at the plasma edge, and thus may lead to favorable H-mode performance with core improvement under a situation of stiff temperature profiles. The reaction of plasma transport to the heat flux profile is investigated for different triangularities in this section. In JT-60U, high triangularity discharges in the type-I ELMy H-mode regime showed higher pedestal temperature than that of low triangularity discharges at a fixed density as presented in chapter 4. The core temperature profiles are shape-preserving in terms of the scale length of the temperature gradient as can be seen by an approximately constant shift on the logarithmic plot when the boundary temperature is raised in the high triangularity configuration.

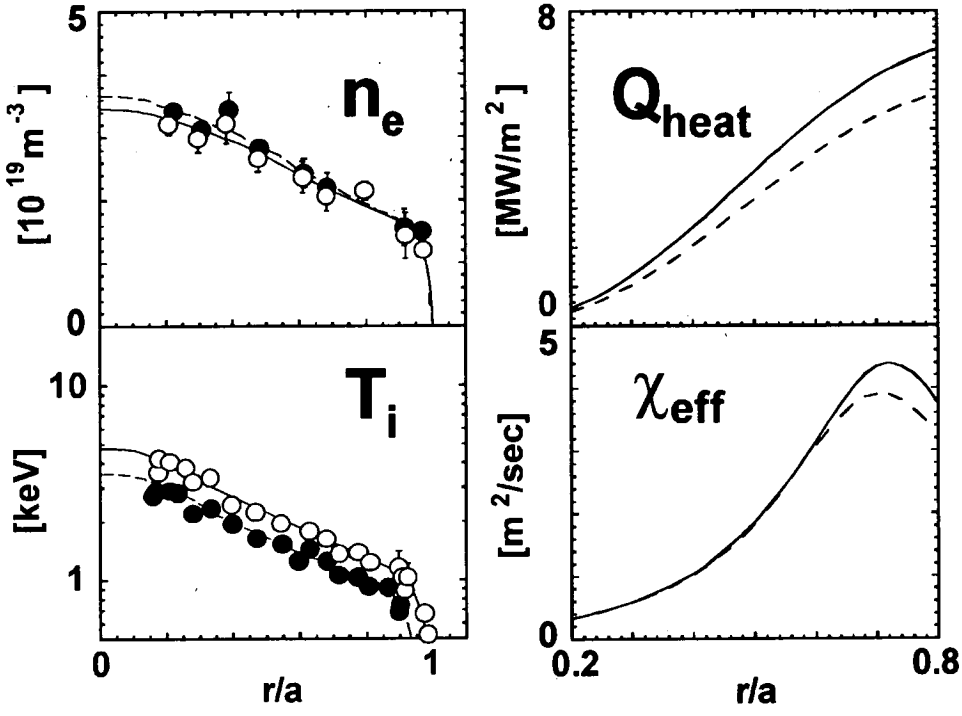

Figure 6.3 Effect of heat flux profile variation on the profiles of temperature and heat diffusivity in the JT-60U NB heated discharges for high triangularity configuration ($\delta_x \sim 0.45$) at I_p / B_t = 1.0 MA / 2.1 T. Full and dashed curves (open and closed circles) indicate the heating power absorbed in the bulk plasma, P_{abs}, of 10.6 MW and 8.5 MW, respectively.

The assumed profile stiffness is also examined by varying the heat flux profile for low ($\delta_x \sim 0.16$) and high triangularity ($\delta_x \sim 0.45$) plasmas using the positive ion-based NBI system. As shown in figure 6.2, the ion temperature profiles for the low-δ_x plasmas are similar, while the resulting species-averaged effective heat conductivities, χ_{eff}, are raised as the heat flux, Q_{heat}, increases, proving the stiffness of temperature profiles. The temperature gradients on log scale, $\nabla(\ln T_i)$, are kept almost constant in the range of $0.2 < r/a < 0.8$. This profile similarity was also found in electron temperature profiles, i.e., $\nabla(\ln T_e) \sim$ const. The T_e profiles seen in our analysis hereafter also have a similar behavior to the corresponding T_i profiles.

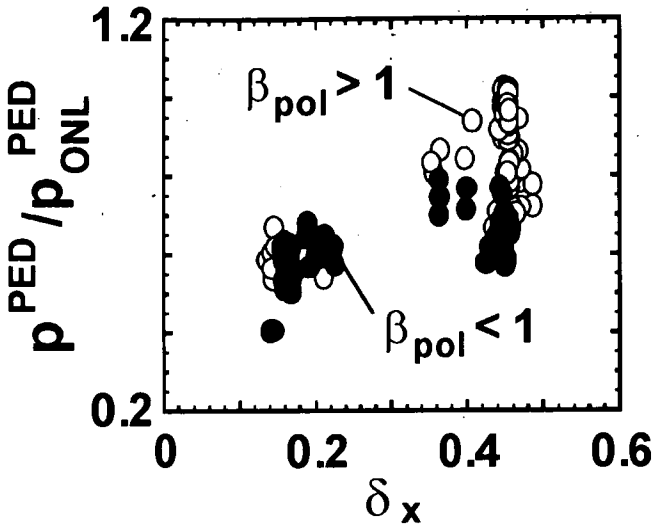

Figure 6.4 Influence of triangularity on the pedestal pressure normalized by the offset non-linear scaling of pedestal pressure. Open and closed circles indicate the data of $\beta_{pol} > 1$ and $\beta_{pol} < 1$, respectively.

The results of high-δ_x plasmas however show different features of the heat transport from the low-δ_x case as shown in figure 6.3. In the high-δ_x plasmas, the temperature profiles of the plasma core are stiff, showing that $\nabla(\ln T_i)$ remains roughly constant. However, the boundary temperature is raised in the highly NB-heated plasma. In proportion to the edge temperature, the core temperature is also raised with a constant scale length of the temperature gradient when the heat flux increases. The heat diffusivity for j-species, χ_j, is evaluated by the following expression:

$$Q^j_{heat} \propto n_j \chi_j \nabla T_j = n_j T_j \chi_j \cdot \nabla(\ln T_j) \tag{6.1}$$

In the high-δ_x case, the energy transport adjusts itself to maintain a constant $\nabla(\ln T)$ due to the increase in the conductive heat flux and its resultant increase in the core temperature. Note that the density profiles are almost identical. Independently of triangularity, the scale length of measured electron temperature gradient is also unaffected by the change in heating power. Especially at higher

densities, due to the strong electron-ion coupling, electron temperature profiles cannot be distinguished from the ion temperatures within the experimental errors.

Related to the increase in the boundary temperature, figure 6.4 indicates the dependence of triangularity on the normalized pedestal pressure evaluated by the offset non-linear (ONL) scaling [70]. The total pedestal pressure, p^{ped}, is given as the summation of the pressure of electrons, deuterium ions and carbon ions. The pedestal pressure in the ONL scaling can be expressed as:

$$p_{ONL}^{ped} = 2.8 I_p B_t a_p^{-1} b^{-0.1} \text{ [kPa]} \quad (6.2)$$

with $b = B_t R_p^{1.25}$.

Figure 6.4 shows that the achievable pedestal pressure increases with triangularity. In addition, it can be seen that high β_{pol} discharges raise p^{ped} at high-δ_x, while p^{ped} at low-δ_x remains nearly unchanged by an increase in β_{pol}. The pedestal pressure at high-δ_x tends to decrease with density [27,126]. The insensitive lower envelope is attributed mainly to low pedestal confinement seen in high triangularity discharges at high densities. At high-δ_x, a larger Shafranov shift due to an increase in β_{pol} or an increase in the field line curvature at the lower field side might account for the improvement of edge stability. High triangularity configuration can display its potential on the pedestal improvement at high β_{pol} discharges. In JT-60U, the edge pedestal pressure gradient in the type-I ELMy H-mode phase is critical both for high-*n* ideal ballooning mode and for intermediate-*n* kink-ballooning mode [127]. In addition, a detailed density fluctuation study has shown that the type-I ELM crash is highly localized poloidally at the lower field side [128].

In high triangularity ELMy H-mode discharges in JT-60U [75], the pedestal temperature and the pedestal pressure increases gradually with a slow time constant of ~ 2 s (~ $10 \times \tau_E$) which is comparable with the edge current diffusion time over the pedestal layer. In this case, the total β_{pol} also increased simultaneously. Therefore, both β_{pol} and edge current seem to contribute to

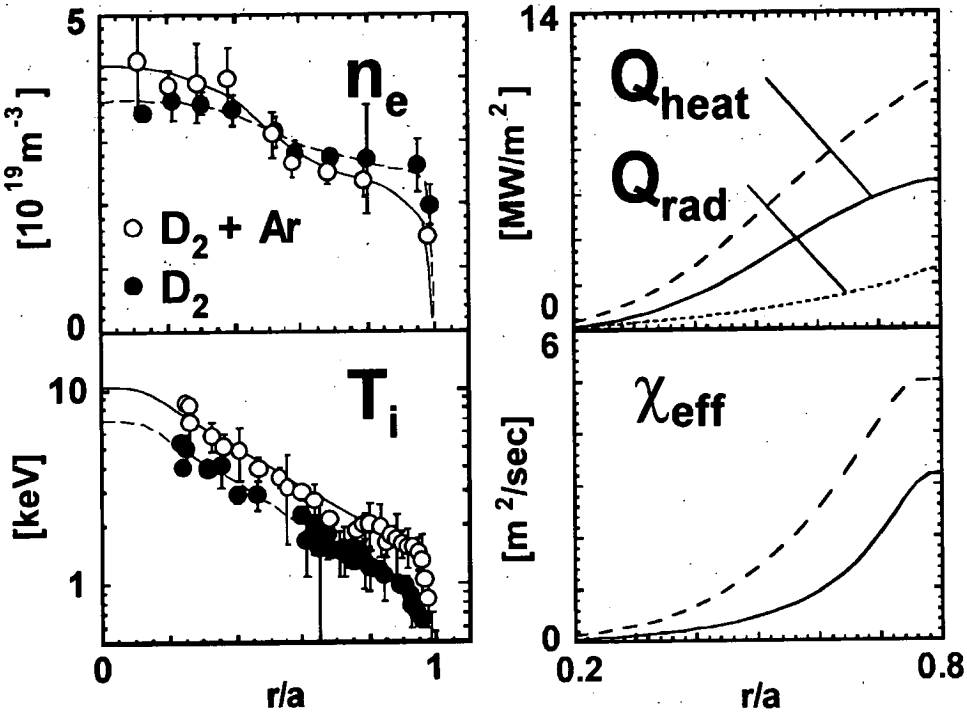

Figure 6.5 Effect of argon gas injection ($n_{Ar}/\bar{n}_e$ ~ 0.8 %) on the heat transport for the case of fixed $\bar{n}_e$ (~ 0.58 n^{GW}) and P_{NBI} (~ 16 MW) at I_p/B_t = 1.2 MA / 2.6 T. Full and dashed curves (open and closed circles) indicate the discharges with and without argon gas injection, respectively. Radiation loss flux, Q_{rad}, is shown for the argon gas seeded plasma as a dotted line, while Q_{rad} for the plasma without argon injection is relatively negligible.

increasing the critical edge pressure. Consequently, the edge stability of type-I ELMy H-mode plasmas seems to be determined by triangularity, total β_{pol} and edge current driven mainly by the bootstrap current [90].

6.4. Effects of argon gas injection on plasma boundary and core transport

Controlled injection of impurity gases is a promising technique for enhancement of radiation loss power fraction to mitigate the severe problem of

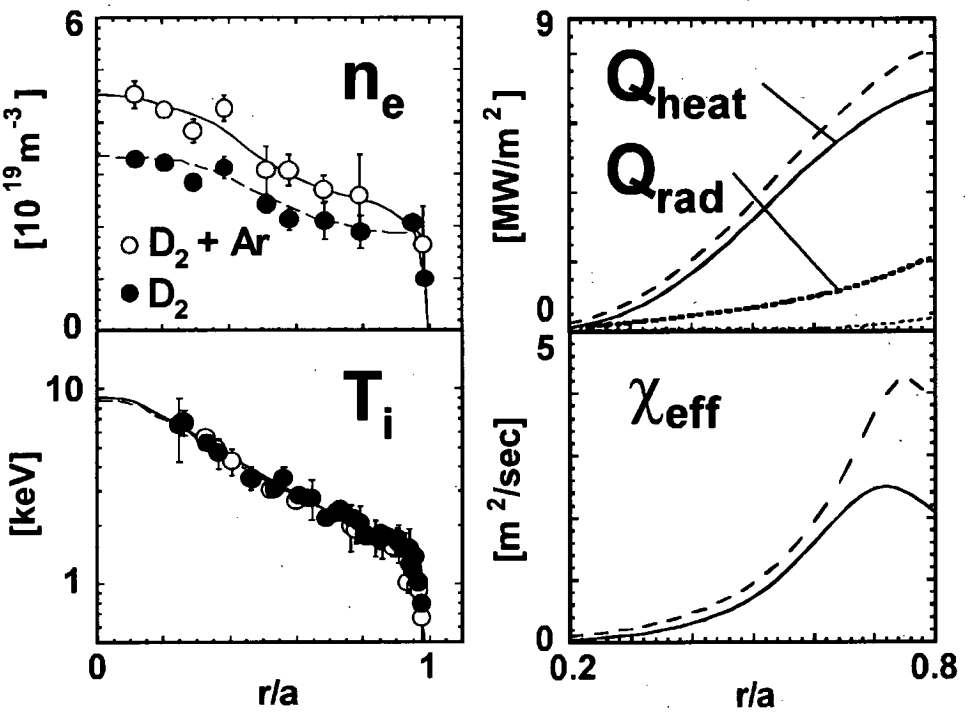

Figure 6.6 Effect of argon gas injection ($n_{Ar}/\bar{n}_e$ ~ 0.5 %) on the heat transport for the case of fixed T_i^{ped} (~ 1.7 keV) and P_{NBI} (~ 16 MW) at I_p / B_t = 1.2 MA / 2.6 T. Full and dashed curves (open and closed circles) indicate the discharges with and without argon gas injection, respectively. Radiation loss fluxes, Q_{rad}, are shown for the cases with and without argon gas injection as broken and dotted lines, respectively.

concentrated power loading on the divertor plates. Confinement improvement due to impurity injection has also been observed with the formation of a radiating mantle in several devices [35-38,100,101,129,130]. In JT-60U [37,38], highly improved energy confinement ($H_H^{IPB98(y,2)}$ = 0.9-1.0) has been sustained by argon gas injection until $\bar{n}_e/n^{GW}$ reaches ~ 0.60. Figure 6.5 shows the effect of argon gas injection on profiles of n_e, T_i, Q_{heat} and χ_{eff} at a fixed $\bar{n}_e/n^{GW}$ of ~ 0.58. The experiments were performed with and without argon gas injection in deuterium plasmas at a fixed NB injection power, P_{NBI} ~ 16 MW. As can be seen in figure 6.5, the absolute value of T_i in argon gas seeded plasma becomes higher than T_i without argon injection throughout the entire range of the minor radius. The

temperature profiles of the plasma core are stiff in the sense of a constant $\nabla(\ln T_i)$ as the boundary temperature is varied. For the argon gas injected case, the argon concentration, n_{Ar}/n_e, is ~ 0.8 %. In these plasmas, the effective charge numbers, Z_{eff}, are ~ 4.0 and ~ 2.1 for the cases with and without argon gas injection, respectively. It is seen in figure 6.5 that the conductive heat flux is reduced with increasing the radiation loss flux, Q_{rad}, at a fixed P_{NBI}. Hence, as can be estimated by Eq. (6.1), χ_{eff} is decreased by the reduction in Q_{heat} in conjunction with the increase in the core temperature. On the other hand, the density profile in argon injected case tends to be more peaked than the case without argon injection, and thus the edge density becomes relatively lower, resulting in a small difference of p^{ped} ($\leq$ 8 %) between D_2 and D_2 + Ar gas injected plasmas as is shown in figure 5.8. Higher boundary temperatures are obtained at lower pedestal densities due to peaked density profiles in argon seeded discharges.

The heat transport in argon puffed plasmas could then be examined at the pedestal temperature nearly compatible with that in the case without argon puff as shown in figure 6.6. In this figure, $\bar{n}_e/n^{GW}$ ~ 0.45 and ~ 0.60 in D_2 and D_2 + Ar gas injected plasmas, respectively. In the plasma with argon injection, n_{Ar}/n_e, is ~ 0.5 %. The effective charges, Z_{eff}, are ~ 4.0 and ~ 2.5 for the cases with and without argon gas injection, respectively. It can be seen that the temperature profiles of high density argon seeded plasmas are nearly consistent with those of low density plasmas without argon gas injection. In figure 6.6, when χ_{eff} decreases due to argon gas injection at a fixed P_{NBI}, conductive heat flow is reduced slightly with increasing radiation flow and the density profile becomes more peaked. Improved particle confinement seen in the argon puffed plasmas results in an increase of the achievable density at a given T^{ped} and could contribute to the reduction in χ_{eff}.

In chapter 5, it has been seen for the cases without argon gas injection that the core heat diffusivity decreases slightly with the pedestal temperature (see

figure 5.9). The relationship between the pedestal temperature and the core heat diffusivity in argon gas injected plasmas seems roughly close to that of the discharges without argon gas injection. Nonetheless, it has been observed that heat conductivities tend to be smaller systematically only by ≤ 15 % with a scatter at a fixed pedestal temperature than those in the plasmas without impurity injection. This difference could be caused by the improved particle confinement and the reduction in the conductive heat flow due to enhancement of the radiation loss power fraction in argon gas seeded discharges.

6.5. Discussions

In weakly collisional plasmas with high power NB heating sources the turbulence driven by ion temperature gradients (ITGs) is believed to be the main origin of turbulence with large correlation lengths, causing anomalous transport through the ion channel [84-87]. The properties of turbulence driven by temperature gradient (TG) lead to a limitation on the temperature profiles by a critical scale length of temperature gradient, which is characterized by $[\nabla(\ln T)]_c$. When $\nabla(\ln T) \leq [\nabla(\ln T)]_c$ TG transport is not active. When $\nabla(\ln T) \geq [\nabla(\ln T)]_c$ transport is high and keeps the profiles close to $[\nabla(\ln T)]_c$. These transport considerations are not necessarily valid inside the sawtooth inversion radius where profiles are essentially determined by this MHD activity. In H-mode the edge plasma should also be excluded due to the transport barrier and ELM activity.

The temperature profiles seen in NB-heated H-modes at any triangularities are qualitatively in agreement with these predictions. In argon gas injected discharges shown in section 6.5, the conductive heat flux reduced by increased radiation flux was still sufficient over a large part of the plasma for the temperature profiles to reach $[\nabla(\ln T)]_c$. Therefore, the transport might be determined by $[\nabla(\ln T)]_c$ over the major part of plasma radius. Comparison of heat

transport between experiments and predictions of theory based on transport models is required for quantitative evaluation of $[\nabla(\ln T)]_c$. The effect of Z_{eff} on the critical scale length of temperature gradient could not be clearly found between D_2 and D_2 + Ar injected experiments within the experimental errors.

6.6. Conclusions

The energy transport properties under the situation of the temperature profile stiffness have been investigated for high triangularity and argon gas injected ELMy H-mode plasmas. Independently of triangularity, the measured core temperature profiles ($0.2 < r/a < 0.8$) are unaffected by the change in the heat flux profile. At low triangularities, χ_{eff} is raised with a similar temperature profile including the plasma edge as the heat flux increases. However, in high triangularity discharges, the boundary temperature is raised with an increase in β_{pol} while the core $\nabla(\ln T_i)$ remains nearly unchanged. In argon seeded plasmas, the temperature becomes higher than the case without argon injection at a fixed density throughout the entire minor radius. The conductive heat flux is reduced with increasing the radiation loss flux due to argon gas injection and thus χ_{eff} decreases. Higher boundary temperatures are obtained at lower pedestal densities due to peaked density profiles in argon seeded discharges. Improved particle confinement due to argon gas puff raises the achievable density and contributes to the reduction in χ_{eff}.

7. Multi-Machine Database Analysis of H-mode Plasmas

7.1. Introduction

One of the features of the H-mode regime is the steep gradient in the temperature and density profiles near the plasma boundary. The region of steep gradients is often referred to as the H-mode transport barrier or more loosely the "edge pedestal." Understanding of edge pedestal characteristics has been recognized as an important issue of investigation, as it strongly influences the prediction of plasma performance for future magnetic fusion devices, such as ITER.

The characteristics of the H-mode edge pedestal are crucial for characterizing the confinement and stability properties of the core plasma and for quantifying the effect of ELM energy load on divertors. Understanding and prediction of pedestal pressure during type-I ELMs, which is considered as one of the reference operation modes of ITER, are essential, since the energy confinement of core plasma is believed to be strongly linked to the pedestal pressure. High pedestal pressure is generally needed for good confinement, while this may lead to a potential disadvantage of unacceptably high energy load on the divertor plate during ELMs. In order to address these issues and investigate other pedestal characteristics, a multi-machine pedestal database has been archived which includes various pedestal-related quantities, e.g., pedestal height for electron density, ion and electron temperatures, and pedestal width and gradient, from major divertor tokamaks, ASDEX-Upgrade (AUG), Alcator C-Mod (C-Mod),

Table 7.1 Contents of the multi-machine pedestal database [39]

	L-H and H-L	ELM free	Type-I ELMs	Type-III ELMs	Grassy ELMs	EDA	Other	Total
AUG	62	—	109	125	—	—	88	384
C-Mod	79	12	—	5	—	21	—	117
DIII-D†	417	—	4275	1153	—	—	474	6319
JET	8	4	41	16	—	—	86	155
JT-60U	25	259	140	45	24	—	5	498

† Note that DIII-D data are taken from 36 shots with ITER shape

DIII-D, JET and JT-60U.

It is widely observed that the confinement starts to degrade as density is increased. In this chapter, analysis of the relation of core confinement and pedestal parameters is performed using the multi-machine pedestal database to identify the underlying physics of this confinement degradation. A possible method to obtain improved pedestal conditions for good confinement in high density discharges by increasing the plasma triangularity is also presented.

7.2. Multi-machine pedestal database

To investigate the universal characteristics of edge pedestal, an international multi-machine pedestal database has been built. The first version of the database, which was installed during 1997, archives the pedestal data from major divertor Tokamaks, ASDEX-Upgrade (AUG), Alcator C-Mod (C-Mod), DIII-D, JET and JT-60U. Additional JT-60U, JET and AUG data have recently been supplied to the database. The database mainly stores the following pedestal parameters: temperatures at the shoulder of the H-mode pedestal (T_e^{ped}, T_i^{ped}), electron density at the top of pedestal (n_e^{ped}), pedestal widths for temperatures, density and electron pressure. Pedestal parameters during various phases of discharge are stored for each discharge, i.e. L-mode prior to L-H transition, ELM-

free, type-I ELMs, type-III ELMs, grassy ELMs, Enhanced D_α mode (EDA), H-mode prior to H-L transition. The detailed contents of the database as of Oct. 2000 are summarized in table 7.1 [39].

Due to diagnostics limitations in each machine, there are still missing data in the database. These missing data are estimated using the following assumptions: (1) $T_e^{ped} = T_i^{ped}$ except JT-60U. (2) The pedestal pressure is defined $p^{ped} = n_e^{ped} k_B (T_e^{ped} + 0.6T_i^{ped})$, i.e. $Z_{eff} = 3.0$ with an assumption of the main impurity being carbon. To compare pedestal parameters among the multi-machine data, the pedestal height (T_e^{ped}, T_i^{ped}, n_e^{ped}) should be derived using the same definition. The most reliable data may be obtained from a hyperbolic tangent (*tanh*) fit to the pedestal region with appropriate linear terms [131] if there are enough data to fit. In many machines, however, the data are not enough to perform *tanh* fits. For these machines, the pedestal width and height are estimated using a linear fit to the data.

7.3. Plasma magnetic geometry

Several tokamaks have reported a strong influence of magnetic geometry on the parameters of the H-mode pedestal. Changes in edge triangularity [26,27,29, 132], elongation [133] and squareness [132] have all been shown to induce strong changes in the pedestal parameters, either by shifting the relevant stability boundary or by shifting from one stability limit to another. In a given machine, it is often difficult to vary these shape parameters independently and thus comparisons between different machines are attractive. Moreover, the influence of the machine size and inverse aspect ratio on the pedestal parameters can be satisfactorily studied only with data from several machines. The pedestal database as of Sep. 2001 [134], which combines data from five different machines, enables independent analysis of the dependence of pedestal parameters on the machine

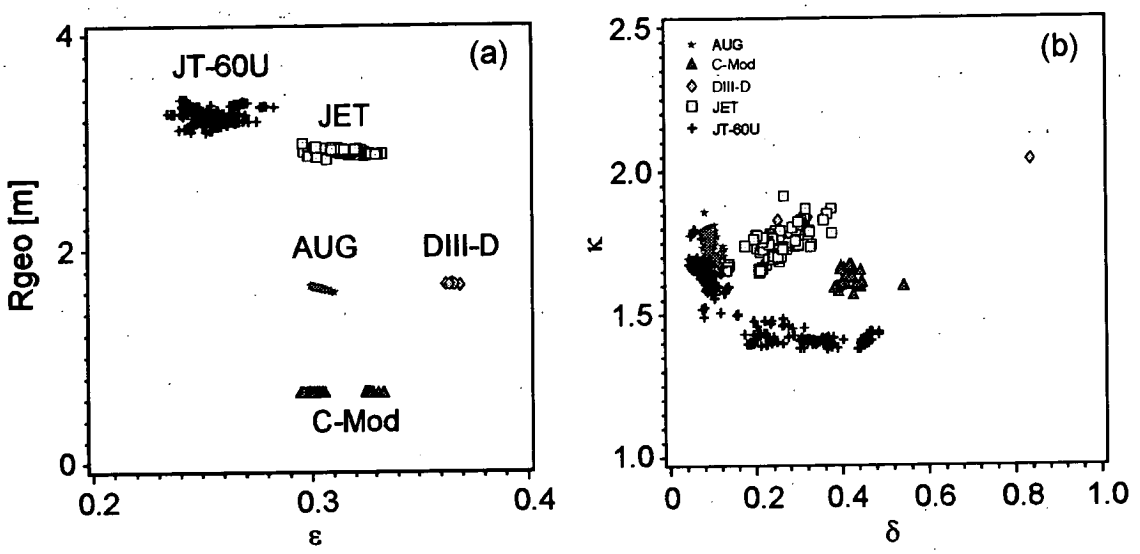

Figure 7.1 The spread of data provided by the multi-machine database [134]: (a) major radius versus inverse aspect ratio and (b) elongation versus triangularity.

size, R_{geo}, and inverse aspect ratio, ε, as shown in figure 7.1(a). The range of triangularity and elongation values provided by the multi-machine database for type-I ELMy H-mode discharges is shown in figure 7.1(b). It can be seen that large tokamaks such as JET and JT-60U have larger R_{geo} compared with a smaller machine size of Alcator C-Mod. On the other hand, JT-60U shows the smallest ε in the database while the largest ε can be seen in DIII-D. The low values of elongation are a significant feature of JT-60U data. In particular, higher κ configuration can be formed at lower δ but the increase in δ tends to reduce κ.

7.4. Boundary condition for core confinement

For a tokamak reactor, high density operation is required to achieve sufficiently high fusion gain and to increase radiation power loss in the scrape-off layer (SOL) and divertor regions in order to reduce the heat load onto the divertor plates [22]. However, energy confinement (the H-factor) in ELMy H-modes tends

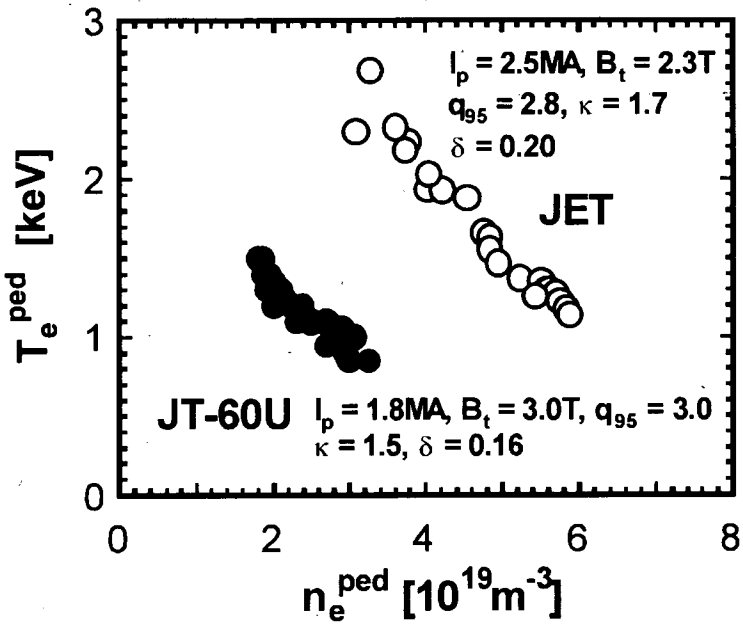

Figure 7.2 Edge operational space diagram for type-I ELMy H-mode plasmas. Open and closed circles denote JET and JT-60U discharges, respectively.

to degrade continuously with increasing density [52,53,55,56]. It is crucially important to develop understanding of the confinement degradation in high density for confinement prediction of future reactors. This section introduces the database of the pedestal parameters as the boundary condition for the core confinement and suggests a method to obtain improved pedestal conditions at a high density.

At sufficiently high input powers, the edge confinement of ELMy H-mode plasmas is imposed by regular type-I ELM events. The edge operational diagram for classifying ELM behavior [135] shows that an increase in the peripheral density in the type-I ELMy H-mode regime is accompanied by a decrease in the temperature at the pedestal shoulder (see figure 7.2). Experimentally, there are two typical cases in the pedestal pressure when density or gas puffing rate is increased. In JT-60U and ASDEX-Upgrade, the pedestal pressure remains roughly constant ($n^{ped}T^{ped}$ ~ const.) at low triangularity for fixed

I_p and B_t [59,79,136]. In JET, the pedestal pressure gradually decreases with density [27]. It is observed in both cases that the edge pedestal temperature determined by the action of type-I ELMs has a large influence on the energy confinement of the plasma core [60]. In particular, since the pedestal temperature decreases with increasing the edge density in type-I ELMy H-mode regime, the confinement degradation can be linked to the relatively low pedestal temperatures.

Figure 7.3(a) and (b) indicate the dependence of the H-factor relative to the ITER89P L-mode scaling [13] upon the pedestal electron temperature. In this dataset, it can be seen that once a critical temperature is exceeded ($T_e^{ped} \sim$ 1.3-1.4 keV) the impact of the pedestal temperature on the energy confinement weakens. It should be noted that the critical temperature might vary with various discharge conditions and machine size, which should be identified in future. A confinement improvement with increasing pedestal temperature takes place below the critical pedestal temperature. It should also be noted here that the confinement degradation at high density is mainly attributed to the confinement deterioration of the core plasma. Based on these experimental observations, it is concluded that, in the H-mode discharges, where the pedestal pressure is limited by the type-I ELMs, an increase in the pedestal density decreases the pedestal temperature, and if the pedestal temperature becomes lower than a certain level, confinement starts to degrade with decreasing temperature or increasing density.

These observations naturally suggest that the critical density, at which confinement degradation sets in, will be increased with increasing triangularity, because the edge pressure gradient (edge α-parameter) increases with triangularity. The α-parameter denotes the normalized pressure gradient given as:

$$\alpha = -\frac{2\mu_0 R_p q^2}{B_t^2}\frac{dp}{dr} \tag{7.1}$$

and α indicates a measure of the pressure gradient responsible for the MHD instability. In fact, experimental data in the database show that the edge α-

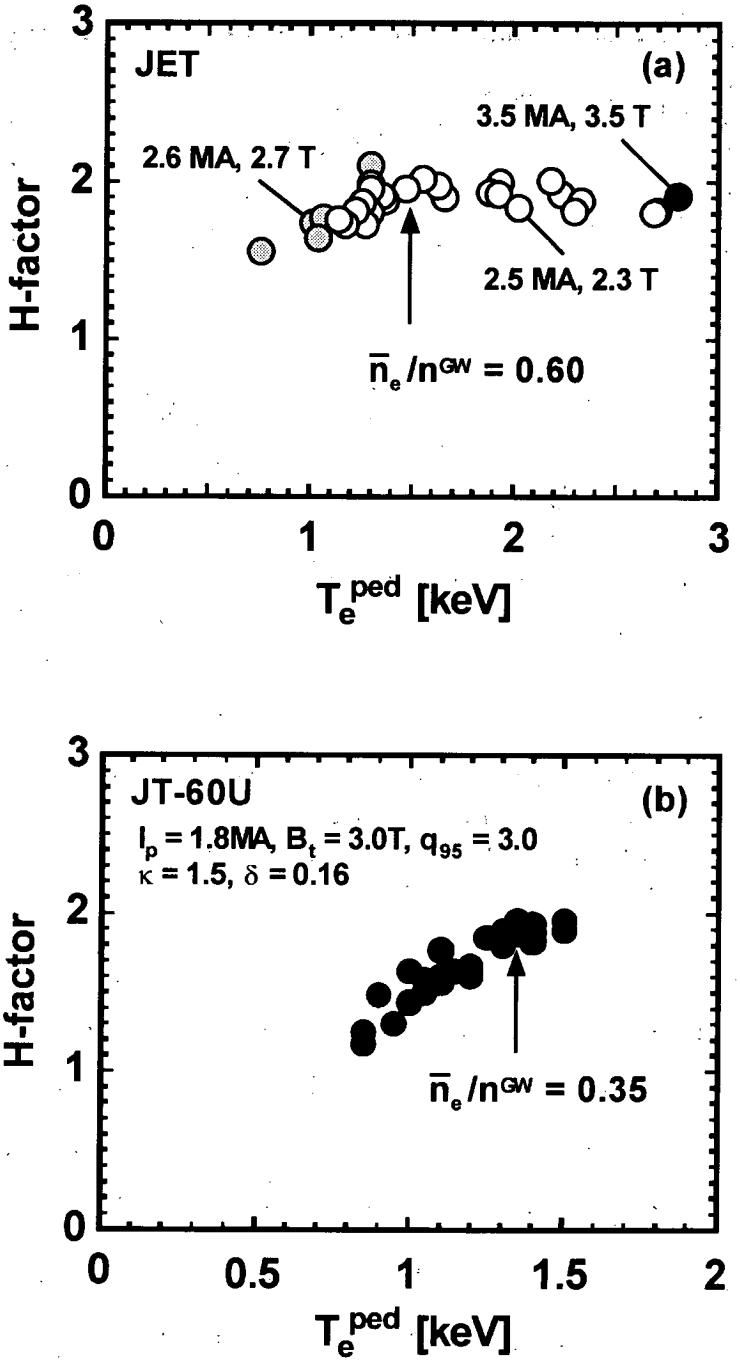

Figure 7.3 Dependence of the *H*-factor on the pedestal temperature in (a) JET and (b) JT-60U.

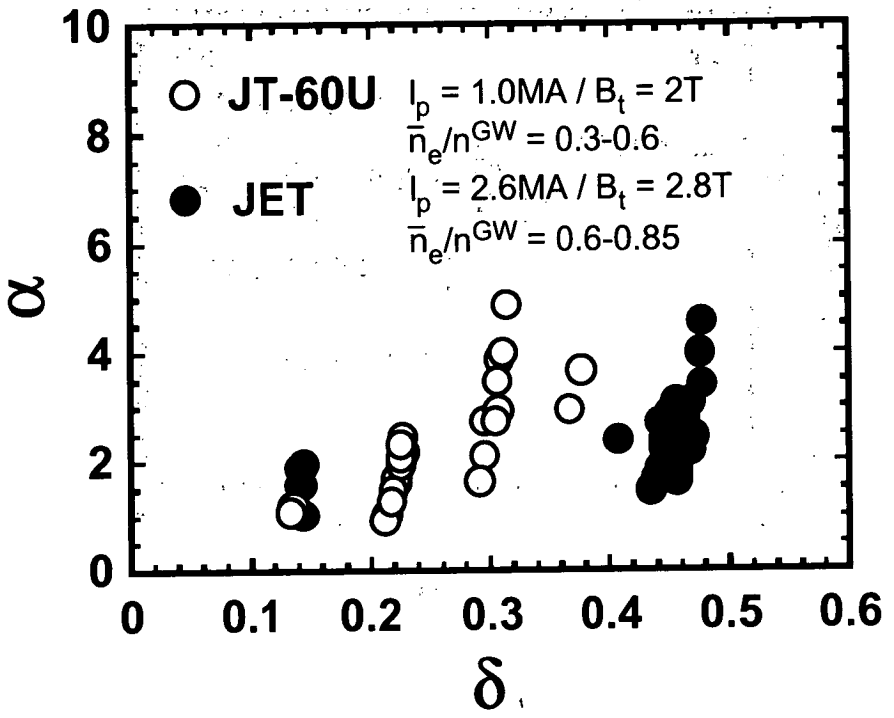

Figure 7.4 Relation between the normalized edge pressure gradient (α-parameter) and triangularity. The edge α-parameter is increased by a factor of 1.5-2 from δ = 0.14 to 0.48 in JT-60U (open circles) and by a factor of 3-4 from δ = 0.14 to 0.38 in JET (closed circles).

parameter is increased by a factor of 1.5-2 from δ = 0.14 to 0.48 in JT-60U and by a factor of 3-4 from 0.14 to 0.38 in JET as shown in figure 7.4. Here, the edge pressure gradient is evaluated by $p^{ped}/\Delta r$, where Δr denotes the width of the edge pedestal. In JT-60U, Δr is estimated from the ion temperature profile measured by charge-exchange recombination spectroscopy (CXRS), while Δr = 7 cm is assumed for JET type-I ELMy H-mode plasmas. In accordance with this increase of α-parameter, the *H*-factors are observed to increase with triangularity in JT-60U [26], ASDEX-Upgrade [31], JET [27] and DIII-D [30], in high density regime (see figure 7.5, 7.6, 7.7 and 7.8). The increase of α-parameter leads to higher pedestal temperature, which results in higher energy confinement of the core plasma, at a given pedestal density in high triangularity discharges.

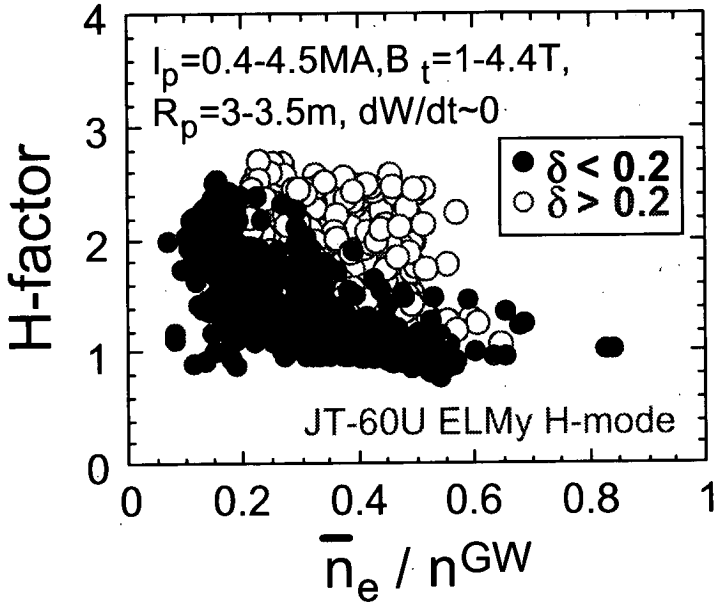

Figure 7.5 Effect of triangularity on the *H*-factor of ELMy H-mode plasmas in JT-60U ($dW_{dia}/dt \sim 0$) [26]. Higher *H*-factor can be obtained at high density with increasing δ.

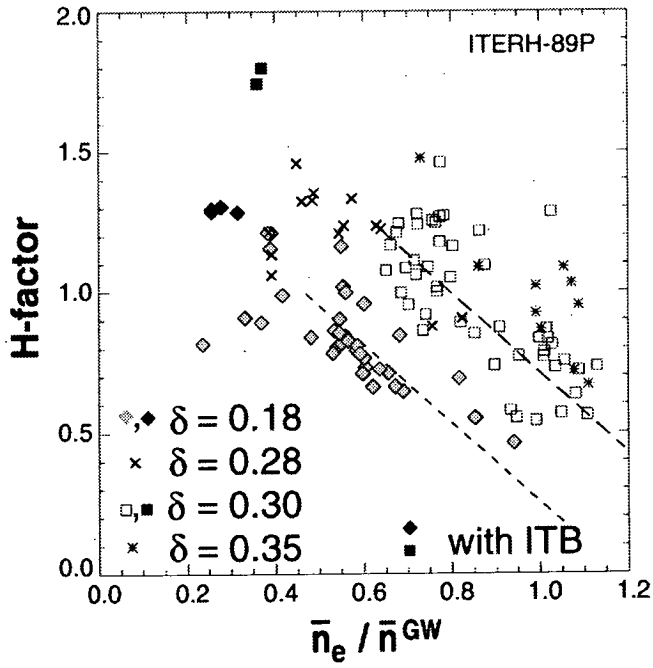

Figure 7.6 H-factor relative to the ITER89P L-mode scaling as a function of $\bar{n}_e$ devided by the Greenwald density in ASDEX-Upgrade [31].

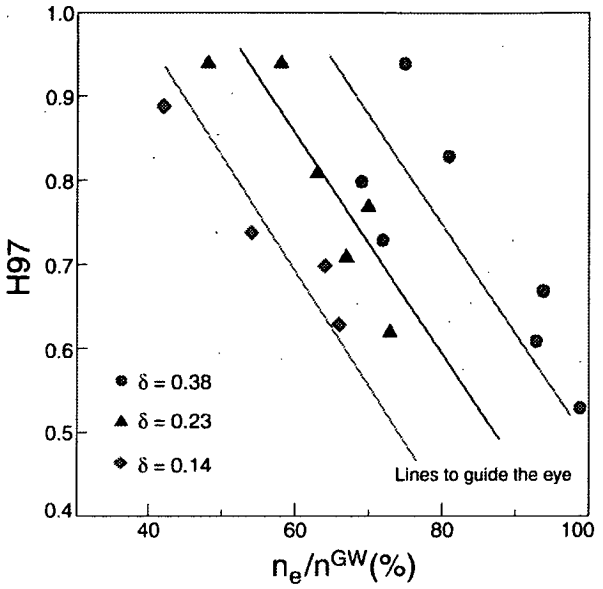

Figure 7.7 Degradation of confinement as a function of plasma density for three series of gas scans in JET, at 2.6 MA / 2.7 T, P_{abs} ~ 12 MW and edge δ of 0.14 to 0.38 [27].

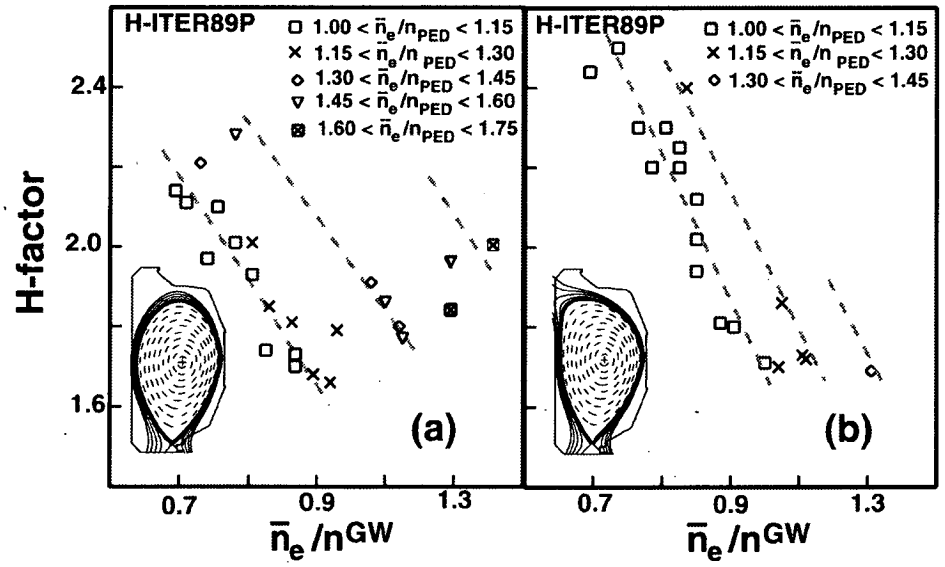

Figure 7.8 Energy confinement enhancement factor over ITER89P L-mode scaling is reduced at high density at both (a) low and (b) high triangularity in DIII-D [30]. The *H*-factor increases with density peaking.

7.5. Conclusions

With the use of the multi-machine pedestal database, the effects of pedestal parameters on the energy confinement, which are essential issues for ELMy H-mode regime, have been investigated. Examination of the relation between core confinement and pedestal temperature among different tokamaks showed that there exists some critical pedestal temperature below which the core confinement starts to degrade. Increasing the triangularity has been shown to be a possible method for maintaining high pedestal temperature in high density H-mode discharges and thus attaining high energy confinement. Comparisons of stability between machines and between different codes are required in order to provide a basis for extrapolation to next step devices.

H-mode physics is an area of fusion science where a qualitative, phenomenological understanding has been attained, but its complexity has prevented development of theoretical prediction methods appropriate for scaling present experimental results to reactor scale devices. The H-mode is characterized by pedestal temperature and density values just inside the transport barrier, width of the high gradient, transport barrier region, and the extent and consequences of edge localized modes (ELMs) destabilized by the steep gradients. Since all these issues bear on how a future fusion reactor will function and first-principle prediction is difficult, reactor scale experiments will be needed to establish a reactor scale phenomenological understanding to support the future fusion reactor design. In the meantime, vigorous experimental and database campaign should be maintained in the Parties' base programs to foster the theory of H-mode physics and to create databases that will both guide the theory and support empirical regression projections of H-mode physics for the design of reactor scale experiments.

8. Conclusions

Understanding and improving energy confinement in fusion plasmas is an active field of research since it determines the prediction and design of a next-step experimental reactor. In this thesis the energy confinement and transport properties of H-mode plasmas, which are expected to be the standard operation mode for use in ITER, have been investigated for H-mode plasmas with a range of density, plasma shape, seed impurity (argon gas) concentration, and conductive heat flux in the JT-60U tokamak. The research focused on the physics mechanism of core energy transport affected by the edge pedestal structure on the basis of the temperature profile effects. To determine the main cause of confinement degradation (or reduction in the confinement enhancement factor) at high densities, the density dependencies of thermal energy confinement and transport coefficients were examined systematically by separating the thermal stored energy into the H-mode pedestal and core components. The results showed that the boundary condition determines the core energy confinement in ELMy H-mode plasmas. Based on these results, it was shown that the energy confinement properties in high triangularity and argon seeded ELMy H-mode plasmas, which are capable of producing higher energy confinement at a given density, could also be explained consistently by the basic transport physics determining the properties of the standard H-mode plasmas. The effects of conductive heat flow on energy transport concerning the temperature profile similarity were also investigated for these conventional H-mode plasmas. The boundary condition for core confinement was discussed among several tokamaks by using an international multi-machine pedestal database. The main results obtained in this study are summarized below.

(1) Analysis of thermal energy confinement properties in low triangularity H-mode plasmas with the fast ion component removed indicated that the commonly observed reduction in the global stored energy at high densities was caused by the saturation of thermal stored energy, which was predicted to increase with density by many confinement scaling laws. Both core and pedestal components of the thermal stored energies remained approximately constant over the density range covered in the experiments. The energy confinement enhancement factor of the core component evaluated by the offset non-linear (ONL) scaling, which predicted that high density operation would improve energy confinement in the plasma core, decreased remarkably with increasing density, while the pedestal component remained almost constant over a wide range of densities.

(2) The influence of the edge pedestal structure imposed by the destabilization of type-I ELMs on thermal energy confinement of the core plasma was quantitatively investigated. As the density was increased, the saturation of the pressure at the pedestal shoulder caused by the type-I ELM activities led to a reduction in pedestal temperature. The core temperature for each species, in turn, decreased only by an approximately constant factor with a reduction in pedestal temperature, proving the existence of the edge-core proportionality on temperature profiles (profile stiffness). Thus, the thermal stored energy was saturated in the high density regime.

(3) High triangularity ELMy H-mode discharges ($\delta_x \sim 0.45$) at low densities ($\bar{n}_e/n^{GW} < 0.5$) were characterized by type-I ELMs, and higher H-mode pedestal pressure than that in low triangularity plasmas was produced. In the high density regime ($\bar{n}_e/n^{GW} > 0.5$) at fixed NB heating power, type-III

ELMs were generated and the pedestal pressure gradually decreased with an increase in density. Compared to low triangularity plasmas at low densities, higher pedestal temperature was obtained at high triangularity, and the core temperature was also improved by almost the same factor. The profiles of temperature were stiff over a wide range of densities and plasma shapes in the sense that there existed a minimum scale length of temperature gradient. Since plasma shaping strongly affects the peripheral region of magnetic flux surfaces, improvement in the edge stability by triangularity leads to higher pedestal temperature, which in turn raises the core temperature through the temperature profile similarity.

(4) High poloidal beta (β_{pol}) H-mode plasmas characterized by the existence of an internal transport barrier (ITB) with an H-mode edge produced even higher pedestal confinement, or pedestal pressure. At high triangularity, the H-mode pedestal height, which was affected by the edge stability for ELMs, increased further when the core energy confinement was improved or when β_{pol} was increased by ITB formation.

(5) Controlled injection of argon gas enabled the energy confinement to be improved (~ 50 %) with high radiation loss power at high density ($\bar{n}_e \sim 0.65 \times n^{GW}$) compared to the case with only deuterium gas puffing. Under the condition of $n_{Ar}/n_e < 1$ %, the dominant intrinsic impurity was carbon. Thermal energy confinement improvement more than compensated for the dilution of deuterium ions due to impurity contamination, resulting in higher neutron production rates. With argon gas injection, temperature profiles of ions and electrons were higher at the H-mode pedestal and in the core region than those of the plasma without argon gas puffing. While the density profiles became flatter with increasing density in the case

without argon gas injection, peaked density profiles were maintained even at high densities in argon seeded plasmas. Externally puffed seed argon gas caused a slight reduction in the thermal deuterium ion density and a peaked density profile, leading to a lower pedestal density at a fixed averaged density. Thus, the reduction in the pedestal temperature in argon gas puffed plasmas weakened at a high averaged density. Since the temperature profiles were approximately self-similar in either case with or without argon gas injection, the heat diffusivity was reduced consistently with the temperature at the plasma boundary. Higher temperature in the core region and improved energy confinement were obtained by higher boundary temperature through the profile similarity. Therefore, the impurity injection scenario might be effective for suppressing the confinement degradation expected for a high density operation in ITER.

(6) As the conductive heat flux increased due to high power NB heating, the effective heat diffusivity, χ_{eff}, adjusted itself to sustain a constant $\nabla(\ln T_i)$ in the plasma core, resulting in the temperature profile stiffness. In high triangularity discharges, highly improved energy confinement quality accompanied by high core temperature was obtained when the boundary temperature rose with an increase in β_{pol}. A constant temperature gradient scale length was sustained inside the H-mode edge pedestal in various heat flux profiles at low and high triangularities investigated. As the conductive heat flux decreased with an increase in the radiation loss flux in argon seeded H-mode plasmas, χ_{eff} decreased with a similar $\nabla(\ln T_i)$ of the plasma core in the case without argon gas injection. Improved particle confinement due to argon gas puff raises the achievable density and contributes to the reduction in χ_{eff}.

(7) Examination of the relation between the core confinement and pedestal temperature in different tokamaks using the international multi-machine pedestal database showed that there exists a critical pedestal temperature below which the core confinement starts to degrade. Increasing the triangularity was shown to be a possible method for maintaining high pedestal temperature in high density discharges and thus attaining high energy confinement in a next-step experimental device.

Several issues that should be investigated in future studies became apparent from the work presented in this thesis. The results of systematic analysis of data obtained from NB-heated H-mode experiments showed that temperature profiles inside the H-mode pedestal shoulder change in a self-similar way, so that $T(r) \propto T^{\mathrm{ped}}$. Theoretically, profile self-similarity, which is often called profile stiffness, can be explained by the fact that drift turbulences, such as ITG and TEM, become unstable only if the relevant temperature gradient exceeds a critical level, i.e., $\nabla(\ln T) \geq [\nabla(\ln T)]_c$. This kind of transport could provide a link between core confinement and edge parameters. By substituting these transport models into the energy balance equation under the assumption of very strong transport, $T(r) \propto T^{\mathrm{ped}}$ is obtained in steady state, and we can conclude equivalently that thermal stored energy is determined in proportion to T^{ped}. This qualitative estimation agrees well with experimental observations. For understanding the underlying physics of the temperature gradient (TG) driven turbulences, the dependence of the critical scale length of temperature profile on the plasma parameters must be examined quantitatively. In cases where the transport is not so extreme, the energy confinement might depend on the level of profile stiffness, and its study becomes vitally important, particularly for extrapolation to a tokamak reactor. In addition, it was found that the commonly observed degradation of energy confinement occurred above a critical density, or below the corresponding critical boundary

temperature. The key element determining the critical value of boundary temperature is not known clearly. The investigation of the critical density and boundary temperature should be carried out to extend high energy confinement regime at high density.

Acknowledgements

It is a great pleasure to express my special gratitude to Prof. M. Itagaki of Hokkaido University for his encouragement and many helpful suggestions. I must express my sincere appreciation for his continuous support and assistance throughout three years that enabled this thesis to be successful.

I am particularly indebted to Dr. Y. Kamada of Japan Atomic Energy Research Institute (JAERI) for supporting and guiding me as a supervisor in JT-60 Team. Without his patient encouragement and many productive suggestions, this thesis could not have been completed.

I am very grateful to Drs. H. Ninomiya, A. Kitsunezaki and M. Kikuchi of JAERI, Honorary Prof. T. Yamashina, Prof. T. Hino and Prof. T. Enoto of Hokkaido University, whose encouragement and advice were invaluable. I wish to thank Drs. K. Ushigusa, Y. Miura, R. Yoshino and M. Shimada of JAERI for their thoughtful supports. The encouragement by Dr. S. Oikawa of Hokkaido University is also appreciated.

I cordially acknowledge fruitful discussions on the subjects in particular with Drs. T. Takizuka, H. Kubo, H. Shirai, H. Takenaga, T. Fukuda, T. Hatae, T. Fujita, S. Takeji, T. Oikawa, S. Ide, N. Asakura, S. Higashijima and K. Itami of JAERI. I would also like to express my appreciation for the helpful and valuable discussions with Drs. G. Janeschitz, M. Sugihara and Y. Igitkhanov of ITER Joint Central Team (ITER-JCT) in Max-Planck-Institut für plasmaphysik, Dr. D. R. Mikkelsen of Princeton Plasma Physics Laboratory (PPPL) and Dr. G. Saibene of EFDA Close Support Unit.

My work was carried out with a large number of colleagues in the JT-60 project. I would like, therefore, to thank all members of Naka Fusion Research Establishment of JAERI for their warm friendship and support.

This work was supported by a grant from JAERI as a Fellow of Advanced Science from April 1999 to March 2001, and as a Research Collaborator from April 2001 to March 2002.

Naka Fusion Research Establishment, JAERI
January 2002 (Revised in November 2004) **Hajime Urano**

References

[1] J. P. Holdren: Ann. Rev. Energy Environ. **16** (1991) 235.

[2] J. Raeder et al.: in Safety and Environmental Assessment of Fusion Power (SEAFFP), European Commission, Brussels (1995).

[3] JET Team: Nucl. Fusion **32** (1992) 187.

[4] A. Gibson and the JET Team: Phys. Plasmas **5** (1998) 1839.

[5] S. Ishida et al.: Phys. Rev. Lett. **79** (1997) 3917.

[6] T. Fujita et al.: Phys. Rev. Lett. **78** (1997) 2377.

[7] T. Fujita and the JT-60 Team: Plasma Phys. Control. Fusion **39** (1997) B75.

[8] T. Fujita et al.: Nucl. Fusion **38** (1998) 207.

[9] T. Fujita et al.: Nucl. Fusion **39** (1999) 1627.

[10] ITER Special Working Group Report to the ITER Council on Task #1 Results: ITER EDA Documentation Series 15 (Vienna: IAEA) (1999).

[11] R. Aymar: Plasma Phys. Control. Fusion **42** (2000) B385.

[12] ITER EDA Agreement and Protocol 1: ITER EDA Documentation Series 1 (Vienna: IAEA) (1992).

[13] P. N. Yushimanov et al.: Nucl. Fusion **30** (1990) 1999.

[14] F. Wagner et al.: Phys. Rev. Lett. **49** (1982) 1408.

[15] ASDEX Team: Nucl. Fusion **29** (1989) 1959.

[16] H. Zohm: Plasma Phys. Control. Fusion **38** (1996) 105.

[17] H. Zohm: Plasma Phys. Control. Fusion **38** (1996) 1213.

[18] J. W. Connor: Plasma Phys. Control. Fusion **40** (1998) 191.

[19] J. W. Connor: Plasma Phys. Control. Fusion **40** (1998) 531.

[20] D. L. Hills et al.: Plasma Phys. Control. Fusion **36** (1994) A171.

[21] ITER Physics Expert Groups on Confinement and Transport and Confinement Modelling and Database, ITER Physics Basis Editors: Nucl. Fusion **39** (1999) 2175.

[22] G. Janeschitz et al.: in Fusion Energy 1996 (Proc. 16th Int. Conf. Montreal, 1996) vol 2 (Vienna: IAEA) (1997) p 755.

[23] L. D. Horton et al.: Nucl. Fusion **39** (1999) 1.

[24] A. Loarte et al.: in Fusion Energy 2000 (Proc. 18th Int. Conf. Sorrento, 2000) IAEA-CN-77/ITER/ITERP/11 (2001).

[25] M. Greenwald et al.: Nucl. Fusion **28** (1988) 2199.

[26] Y. Kamada et al.: in Fusion Energy 1996 (Proc. 16th Int. Conf. Montreal, 1996) vol 1 (Vienna: IAEA) (1997) p 247.

[27] G. Saibene et al.: Nucl. Fusion **39** (1999) 1133.

[28] J. Stober et al.: in Controlled Fusion and Plasma Physics (Proc. 26th Eur. Conf. Maastricht, 1999) vol 23J (Geneva: EPS) (1999) p 1401.

[29] W. Suttrop et al.: Plasma Phys. Control. Fusion **42** (2000) A97.

[30] T. H. Osborne et al.: Plasma Phys. Control. Fusion **42** (2000) A175.

[31] J. Stober et al.: Plasma Phys. Control. Fusion **42** (2000) A211.

[32] S. Ishida et al.: in Plasma Phys. and Control Nucl. Fusion Research 1992 (Proc. 14th Int. Conf. Würzburg, 1992) vol 1 (Vienna: IAEA) (1993) p 219.

[33] Y. Koide et al.: Phys. Rev. Lett. **72** (1994) 3662.

[34] H. Shirai et al.: in Plasma Phys. and Control Nucl. Fusion Research 1994 (Proc. 15th Int. Conf. Seville, 1994) vol 1 (Vienna: IAEA) (1995) p 355.

[35] R. R. Weynants: Nucl. Fusion **39** (1999) 1637.

[36] G. L. Jackson et al.: Nucl. Mater. **266-269** (1999) 380.

[37] S. Sakurai et al.: J. Nucl. Mater. **290-293** (2001) 1002.

[38] H. Kubo et al.: Nucl. Fusion **41** (2001) 227.

[39] T. Hatae et al.: Nucl. Fusion **41** (2001) 285.

[40] N. Peacock et al.: Nature **224** (1969) 488.

[41] R. Herman et al.: The Search for Endless Energy, Cambridge University Press (1991).

[42] R. J. Hawryluk et al.: in Plasma Phys. and Control Nucl. Fusion Research 1994 (Proc. 15th Int. Conf. Seville, 1994) vol 1 (Vienna: IAEA) (1995) p 11.

[43] K. M. McGuire et al.: in Fusion Energy 1996 (Proc. 16th Int. Conf. Montreal, 1996) vol 1 (Vienna: IAEA) (1997) p 19.

[44] T. Abe et al.: in Plasma Phys. and Control Nucl. Fusion Research 1986 (Proc. 11th Int. Conf. Kyoto, 1986) vol 1 (Vienna: IAEA) (1987) p 11.

[45] N. Hosogane et al.: in Fusion Energy 1996 (Proc. 16th Int. Conf. Montreal, 1996) vol 3 (Vienna: IAEA) (1997) p 555.

[46] Y. Ikeda et al.: in Fusion Energy 2000 (Proc. 18th Int. Conf. Sorrento, 2000) IAEA-CN-77/EXP4/03 (2001).

[47] Technical Basis for the ITER-FEAT Outline Design: ITER EDA Documentation Series 19 (Vienna: IAEA) (2000).

[48] Y. Shimomura et al.: Nucl. Fusion **41** (2001) 309.

[49] R. Aymar et al.: Nucl. Fusion **41** (2001) 1301.

[50] ITER Physics Expert Groups, ITER Physics Basis Editors, ITER Joint Central Team, and Home Teams (presented by D. J. Cambell): in Fusion Energy 1998 (Proc. 17th Int. Conf. Yokohama, 1998) vol 3 (Vienna: IAEA) (1999) p 931.

[51] Y. Shimomura et al.: Nucl. Fusion **39** (1999) 1295.

[52] JET Team: Nucl. Fusion **39** (1999) 1687.

[53] G. Saibene et al.: in Controlled Fusion and Plasma Physics (Proc. 25th Eur. Conf. Prague, 1997) vol 22C (Geneva: EPS) (1997) p 341.

[54] W. Suttrop et al.: in Fusion Energy 1998 (Proc. 17th Int. Conf. Yokohama, 1998) vol 2 (Vienna: IAEA) (1999) p 777.

[55] O. Gruber et al.: Nucl. Fusion **39** (1999) 1321.

[56] N. Asakura et al.: Plasma Phys. Control. Fusion **39** (1997) 1295.

[57] Y. Kamada et al.: Plasma Phys. Control. Fusion **41** (1999) B77.

[58] M. Greenwald et al.: Nucl. Fusion **37** (1997) 793.

[59] W. Suttrop et al.: Plasma Phys. Control. Fusion **39** (1997) 2051.

[60] G. Janeschitz et al.: in Controlled Fusion and Plasma Physics (Proc. 26th Eur. Conf. Maaştricht, 1999) vol 23J (Geneva: EPS) (1999) p 1445.

[61] T. Fukuda et al.: Rev. Sci. Instrum. **60** (1989) 1080.

[62] T. Hatae et al.: Rev. Sci. Instrum. **70** (1999) 772.

[63] S. Ishida et al.: Rev. Sci. Instrum. **61** (1990) 2834.

[64] Y. Koide et al.: Plasma Phys. Control. Fusion **36** (1994) A195.

[65] T. Nishitani et al.: Rev. Sci. Instrum. **63** (1992) 5270.

[66] K. Tani, M. Azumi, H. Kishimoto and S. Tamura: J. Phys. Soc. Japan **50** (1981) 1726.

[67] H. Shirai et al.: Plasma Phys. Control. Fusion **42** (2000) 1193.

[68] ITER H-mode Database Working Group: Nucl. Fusion **34** (1994) 131.

[69] ITER Confinement Database Modelling Expert Group (presented by T. Takizuka): in Fusion Energy 1996 (Proc. 16th Int. Conf. Montreal, 1996) vol 2 (Vienna:IAEA) (1997) p 795.

[70] T. Takizuka: Plasma Phys. Control. Fusion **40** (1998) 851.

[71] ITER Physics Expert Group on Energetic Particles, Heating and Current Drive, ITER Physics Basis Editors: Nucl. Fusion **39** (1999) 2471.

[72] W. W. Heidbrink, G. J. Sadler: Nucl. Fusion **34** (1994) 535.

[73] Y. Kamada et al.: Plasma Phys. Control. Fusion **36** (1994) A123.

[74] A. Colton et al.: in Controlled Fusion and Plasma Physics (Proc. 20th Eur. Conf. Lisbon, 1993) vol 17C (Geneva: EPS) (1993) p I-11.

[75] Y. Kamada, T. Hatae, T. Fukuda and T. Takizuka: Plasma Phys. Control. Fusion **41** (1999) 1371.

[76] A. W. Leonard et al.: Nucl. Mater. **290-293** (2001) 1097.

[77] M. Shimada et al.: in Fusion Energy 2000 (Proc. 18th Int. Conf. Sorrento, 2000) IAEA-CN-77/ITER/ITERP/05 (2001).

[78] W. Suttrop et al.: Plasma Phys. Control. Fusion **40** (1998) 771.

[79] H. Urano et al.: in Controlled Fusion and Plasma Physics (Proc. 27th Eur. Conf. Budapest, 2000) vol 24B (Geneva: EPS) (2000) p 956.

[80] D. R. Mikkelsen et al.: in Fusion Energy 2000 (Proc. 18th Int. Conf. Sorrento, 2000) IAEA-CN-77/EXP5/20 (2001).

[81] F. Ryter et al.: Nucl. Fusion **41** (2001) 537.

[82] T. H. Osborne et al.: Plasma Phys. Control. Fusion **40** (1998) 845.

[83] H. Yoshida et al.: Rev. Sci. Instrum. **66** (1995) 143.

[84] M. Kotschenreuter et al.: Phys. Plasmas **2** (1995) 2381.

[85] C. Petty et al.: Phys. Rev. Lett. **83** (1999) 3661.

[86] A. Dimits et al.: Phys. Plasmas **7** (2000) 969.

[87] G. Tardini et al.: in Controlled Fusion and Plasma Physics (Proc. 27th Eur. Conf. Budapest, 2000) vol 24B (Geneva: EPS) (2000) p 1148.

[88] F. Jenko et al.: Phys. Plasmas **7** (2000) 1904.

[89] M. Mori et al.: Nucl. Fusion **34** (1994) 1045.

[90] Y. Kamada et al.: Proc. 8th IAEA Technical Committee Meeting on H-mode Physics and Transport Barriers, Toki (2001) C08.

[91] M. Keilhacker et al.: in Plasma Phys. and Control. Nucl. Fusion Research 1992 (Proc. 14th Int. Conf. Würzburg, 1992) vol 1 (1993) p 15.

[92] M. Shimada et al.: in Plasma Phys. and Control. Nucl. Fusion Research 1992 (Proc. 14th Int. Conf. Würzburg, 1992) vol 1 (1993) p 57.

[93] M. C. Zarnstorff et al.: in Plasma Phys. and Control. Nucl. Fusion Research 1992 (Proc. 14th Int. Conf. Würzburg, 1992) vol 1 (1993) p 111.

[94] M. Kikuchi: Nucl. Fusion **30** (1990) 265.

[95] Y. Seki et al.: in Plasma Phys. and Control. Nucl. Fusion Research 1990 (Proc. 13th Int. Conf. Washington, 1990) vol 3 (1991) p 473.

[96] Y. Kamada et al.: Nucl. Fusion **39** (2000) 1845.

[97] Y. Kamada et al.: Plasma Phys. Control. Fusion **42** (2000) A247.

[98] L. L. Lao et al.: Nucl. Fusion **30** (1990) 1035.

[99] Y. Koide et al.: Plasma Phys. Control. Fusion **38** (1996) 1011.

[100] K. Itami et al.: in Fusion Energy 1996 (Proc. 16th Int. Conf. Montreal, 1996) vol 1 (IAEA: Vienna) (1997) p 385.

[101] K. Itami et al.: J. Nucl. Mater. **266-269** (1999) 1097.

[102] G. F. Matthews: Plasma Phys. Control. Fusion **37** (1995) A227.

[103] R. D. Wood et al.: in Controlled Fusion and Plasma Physics (Proc. 23rd Eur. Conf. Kiev, Ukraine, 1996) vol 20C (Geneva: EPS) (1996) p 763.

[104] J. A. Goetz et al.: Phys. Plasmas **3** (1996) 1908.

[105] C. F. Maggi et al.: J. Nucl. Mater. **241-243** (1997) 414.

[106] H. Kubo et al.: Plasma Phys. Control. Fusion **37** (1995) 1133.

[107] R. Reichle et al.: J. Nucl. Mater. **241-243** (1997) 456.

[108] L. C. Ingesson et al.: in Controlled Fusion and Plasma Physics (Proc. 24th Eur. Conf. Berchtesgaden, 1997) vol 21A (Geneva: EPS) (1997) p 113.

[109] T. W. Petrie, D. N. Hill and S. L. Allen: Nucl. Fusion **37** (1997) 321.

[110] A. Kallenbach et al.: Nucl. Fusion **35** (1995) 1231.

[111] J. C. Fuchs, K. F. Mast and G. Hass: in Controlled Fusion and Plasma Physics (Proc. 24th Eur. Conf. Berchtesgaden, 1997) vol 21A (Geneva: EPS) (1997) p 1453.

[112] A. W. Leonard et al.: J. Nucl. Mater. **220-222** (1995) 325.

[113] G. Janeschitz et al.: J. Nucl. Mater. **196-198** (1992) 380.

[114] T. W. Petrie et al.: J. Nucl. Mater. **196-198** (1992) 848.

[115] N. Hosogane et al.: J. Nucl. Mater. **196-198** (1992) 750.

[116] O. Gruber et al.: Phys. Rev. Lett. **74** (1995) 4217.

[117] B. Lipschultz et al.: J. Nucl. Mater. **220-222** (1995) 50.

[118] N. Asakura et al.: Nucl. Fusion **36** (1996) 795.

[119] G. D. Porter et al.: Phys. Plasmas **3** (1996) 1967.

[120] T. W. Petrie et al. Nucl Fusion **37** (1997) 643.

[121] H. Tamai, N. Asakura and N. Hosogane: J. Plasma Fusion Res. **74** (1998) 1336.

[122] P. C. Stangeby: Nucl. Fusion **33** (1993) 1695.

[123] L. D. Horton et al.: Plasma Phys. Control. Fusion **41** (1999) B329.

[124] D. E. Post and R. V. Jensen: Atomic Data and Nuclear Data Tables **20** (1977) 397.

[125] Y. Koide et al.: Rev. Sci. Instrum. **72** (2001) 119.

[126] H. Urano et al.: in Controlled Fusion and Plasma Physics (Proc. 28th Eur. Conf. Madeira, 2001) vol 25A (Geneva: EPS) (2001) p 1341.

[127] L. Lao et al.: Nucl. Fusion **41** (2001) 295.

[128] N. Oyama et al.: Proc. 8th IAEA Technical Committee Meeting on H-mode Physics and Transport Barriers, Toki (2001) D12.

[129] B. Unterberg et al.: in Fusion Energy 2000 (Proc. 18th Int. Conf. Sorrento, 2000) IAEA-CN-77/EX5/02 (2001).

[130] G. P. Maddison et al.: in Fusion Energy 2000 (Proc. 18th Int. Conf. Sorrento, 2000) IAEA-CN-77/EX5/04 (2001).

[131] R. Groebner et al.: Phys. Plasmas **5** (1998) 1800.

[132] T. H. Osborne et al.: Plasma Phys. Control. Fusion **42** (2000) 1.

[133] P. J. Lomas: Plasma Phys. Control. Fusion **42** (2000) B115.

[134] L. D. Horton et al.: Proc. 8th IAEA Technical Committee Meeting on H-mode Physics and Transport Barriers, Toki (2001) C06.

[135] W. Suttrop et al.: Plasma Phys. Control. Fusion **42** (2000) A1.

[136] L. D. Horton: Plasma Phys. Control. Fusion **41** (1999) B329.

This is a blank page.

国際単位系（SI）と換算表

表1　SI基本単位および補助単位

量	名称	記号
長さ	メートル	m
質量	キログラム	kg
時間	秒	s
電流	アンペア	A
熱力学温度	ケルビン	K
物質量	モル	mol
光度	カンデラ	cd
平面角	ラジアン	rad
立体角	ステラジアン	sr

表2　SIと併用される単位

名称	記号
分，時，日	min，h，d
度，分，秒	°，′，″
リットル	l，L
トン	t
電子ボルト	eV
原子質量単位	u

1 eV=1.60218×10^{-19}J

1 u=1.66054×10^{-27}kg

表3　固有の名称をもつSI組立単位

量	名称	記号	他のSI単位による表現
周波数	ヘルツ	Hz	s^{-1}
力	ニュートン	N	m·kg/s^2
圧力，応力	パスカル	Pa	N/m^2
エネルギー，仕事，熱量	ジュール	J	N·m
工率，放射束	ワット	W	J/s
電気量，電荷	クーロン	C	A·s
電位，電圧，起電力	ボルト	V	W/A
静電容量	ファラド	F	C/V
電気抵抗	オーム	Ω	V/A
コンダクタンス	ジーメンス	S	A/V
磁束	ウェーバ	Wb	V·s
磁束密度	テスラ	T	Wb/m^2
インダクタンス	ヘンリー	H	Wb/A
セルシウス温度	セルシウス度	℃	
光束	ルーメン	lm	cd·sr
照度	ルクス	lx	lm/m^2
放射能	ベクレル	Bq	s^{-1}
吸収線量	グレイ	Gy	J/kg
線量等量	シーベルト	Sv	J/kg

表4　SIと共に暫定的に維持される単位

名称	記号
オングストローム	Å
バーン	b
バール	bar
ガル	Gal
キュリー	Ci
レントゲン	R
ラド	rad
レム	rem

1 Å=0.1nm=10^{-10}m

1 b=100fm^2=10^{-28}m^2

1 bar=0.1MPa=10^5Pa

1 Gal=1cm/s^2=10^{-2}m/s^2

1 Ci=3.7×10^{10}Bq

1 R=2.58×10^{-4}C/kg

1 rad=1cGy=10^{-2}Gy

1 rem=1cSv=10^{-2}Sv

表5　SI接頭語

倍数	接頭語	記号
10^{18}	エクサ	E
10^{15}	ペタ	P
10^{12}	テラ	T
10^{9}	ギガ	G
10^{6}	メガ	M
10^{3}	キロ	k
10^{2}	ヘクト	h
10^{1}	デカ	da
10^{-1}	デシ	d
10^{-2}	センチ	c
10^{-3}	ミリ	m
10^{-6}	マイクロ	μ
10^{-9}	ナノ	n
10^{-12}	ピコ	p
10^{-15}	フェムト	f
10^{-18}	アト	a

（注）

1．表1－5は「国際単位系」第5版，国際度量衡局 1985年刊行による。ただし，1 eVおよび1 uの値はCODATAの1986年推奨値によった。

2．表4には海里，ノット，アール，ヘクタールも含まれているが日常の単位なのでここでは省略した。

3．barは，JISでは流体の圧力を表わす場合に限り表2のカテゴリーに分類されている。

4．EC閣僚理事会指令ではbar，barnおよび「血圧の単位」mmHgを表2のカテゴリーに入れている。

換算表

力	N(=10^5dyn)	kgf	lbf
	1	0.101972	0.224809
	9.80665	1	2.20462
	4.44822	0.453592	1

粘度　1 Pa·s(N·s/m^2)=10 P(ポアズ)(g/(cm·s))

動粘度　1 m^2/s=10^4St(ストークス)(cm^2/s)

圧力	MPa(=10bar)	kgf/cm^2	atm	mmHg(Torr)	lbf/in^2(psi)
	1	10.1972	9.86923	7.50062×10^3	145.038
	0.0980665	1	0.967841	735.559	14.2233
	0.101325	1.03323	1	760	14.6959
	1.33322×10^{-4}	1.35951×10^{-3}	1.31579×10^{-3}	1	1.93368×10^{-2}
	6.89476×10^{-3}	7.03070×10^{-2}	6.80460×10^{-2}	51.7149	1

エネルギー・仕事・熱量	J(=10^7 erg)	kgf·m	kW·h	cal(計量法)	Btu	ft·lbf	eV
	1	0.101972	2.77778×10^{-7}	0.238889	9.47813×10^{-4}	0.737562	6.24150×10^{18}
	9.80665	1	2.72407×10^{-6}	2.34270	9.29487×10^{-3}	7.23301	6.12082×10^{19}
	3.6×10^6	3.67098×10^5	1	8.59999×10^5	3412.13	2.65522×10^6	2.24694×10^{25}
	4.18605	0.426858	1.16279×10^{-6}	1	3.96759×10^{-3}	3.08747	2.61272×10^{19}
	1055.06	107.586	2.93072×10^{-4}	252.042	1	778.172	6.58515×10^{21}
	1.35582	0.138255	3.76616×10^{-7}	0.323890	1.28506×10^{-3}	1	8.46233×10^{18}
	1.60218×10^{-19}	1.63377×10^{-20}	4.45050×10^{-26}	3.82743×10^{-20}	1.51857×10^{-22}	1.18171×10^{-19}	1

1 cal= 4.18605J（計量法）

= 4.184J（熱化学）

= 4.1855J（15℃）

= 4.1868J（国際蒸気表）

仕事率　1 PS(仏馬力)

= 75 kgf·m/s

= 735.499W

放射能	Bq	Ci
	1	2.70270×10^{-11}
	3.7×10^{10}	1

吸収線量	Gy	rad
	1	100
	0.01	1

照射線量	C/kg	R
	1	3876
	2.58×10^{-4}	1

線量当量	Sv	rem
	1	100
	0.01	1

（86年12月26日現在）

Energy Confinement and Transport of H-mode Plasmas in Tokamak